STRUCTURAL CHARACTERISTICS IN LONG AFTERGLOW STRONTIUM ALUMINATE COMPOUNDS: AN INVESTIGATION WITH RAMAN AND FTIR SPECTROSCOPY

by
ARZU ERGENE

Submitted to the Graduate School of Engineering and Natural Sciences
in partial fulfillment of the requirements for the degree of
Doctor of Philosophy

Sabancı University
June 2022

STRUCTURAL CHARACTERISTICS IN LONG AFTERGLOW STRONTIUM ALUMINATE COMPOUNDS: AN INVESTIGATION WITH RAMAN AND FTIR SPECTROSCOPY

APPROVED BY:

DATE OF APPROVAL: 30/06/2022

ABSTRACT

STRUCTURAL CHARACTERISTICS IN LONG AFTERGLOW STRONTIUM ALUMINATE COMPOUNDS: AN INVESTIGATION WITH RAMAN AND FTIR SPECTROSCOPY

ARZU ERGENE

Materials Science and Engineering, Ph.D. Dissertation, June 2022

Thesis Supervisor: Prof. CLEVA W. OW-YANG

Keywords: Persistent Luminescence, Strontium Aluminate, Raman Spectroscopy, FTIR Spectroscopy, Energy-Efficient Lighting, Phosphor Pigments

Europium (Eu^{2+}), dysprosium (Dy^{3+}), and boron (B) co-doped strontium aluminate compounds emitting persistent luminescence (PersiL) are well-known for offering illumination with zero energy consumption making them attractive for use in safety signage and paint. Although B is well known to extend the persistence of luminescence from Eu and Dy co-doped strontium aluminates, it is not clear how B induces the formation of the material structure that supports extreme afterglow. Previous work suggests that B incorporates interstitially into $Sr_4Al_{14}O_{25}$: Eu, Dy. The objective of this dissertation is to elucidate how B directs the atomic arrangements in such compounds. To set the stage, we applied materials characterization tools that reveal information about short-range order and localized environments, FTIR and Raman spectroscopy. Because micro-Raman reveals spatially resolved information at the micrometer scale, it is particularly well suited for analyzing strontium aluminate pigments, which can be produced with micron-sized grains. Eu and Dy co-doped $Sr_4Al_{14}O_{25}$ (S4A7ED) synthesized with 30-40 mol% B_2O_3 displayed the longest duration of PersiL, and these compositions do not contain the highest amount of the long persistence phases. Instead, an optimal amount of B is necessary for the incorporation of electrically charged, non-bridging oxygen (NBO) into the doped S4A7ED crystal structure. The use of oxide glass forming precursors of Si, P, and Zr during Pechini processing also extended PersiL in S4A7ED compounds and was correlated with structural changes arising from NBO incorporation. Through the experimental evidence revealed in this work, we discovered a new class of long afterglow compounds.

ÖZET

ISRARLI-IŞILDAMALI STRONSİYUM ALÜMİNAT BİLEŞİĞİNDE YAPISAL ÖZELLİKLERİN RAMAN VE FTIR SPEKTROSKOPİSİ İLE ARAŞTIRILMASI

ARZU ERGENE

Malzeme Bilimi ve Mühendisliği, Doktora Tezi, Haziran 2022

Tez Danışmanı: Prof. CLEVA W. OW-YANG

Anahtar Kelimeler: Israrlı Işıldama, Stronsiyum Aluminat, Raman Spektroskopisi, FTIR, Verimli Aydınlatma, Fosfor Pigmentleri

Israrlı ışıma yayan evropiyum (Eu^{2+}), disprozyum (Dy^{3+}) ve bor (B) katkılı stronsiyum alüminat bileşikleri, sıfır enerji tüketimi ile aydınlatma sunmaları ile bilinirler. Bu özellik onları güvenlik tabelaları ve boyalarda kullanım için çekici kılar. B'un , Eu ve Dy birlikte katkılı stronsiyum alüminatların ısrarlı ışıma süresini uzattığı iyi bilinmesine rağmen, B'un ısrarlı ışımayı destekleyen malzeme yapısının oluşumunu nasıl etkilediği açık değildir. Önceki çalışmalarımızda, B'un arayer olarak $Sr_4Al_{14}O_{25}$:Eu, Dy yapısına dahil olduğu gösterilmiştir. Bu tezin amacı ise B'un bu tür bileşiklerdeki atomik düzenlemeleri nasıl yönlendirdiğini açıklamaktır. Bu amaçla, malzemenin bölgesel yapılarını ve içeriğinde bulunan kısa mesafe düzenli atomik yapıların incelenmesi için FTIR ve Raman spektroskopisi kullanılmıştır. Mikro-Raman spektroskopisi, mikrometre seviyesinde uzaysal çözümlenmiş bilgiler ortaya çıkardığı için, mikron seviyede üretilen stronsiyum aluminat pigmentlerinin analizi için oldukça uygun bir yöntemdir. Sonuçlarımız gösterdi ki, Eu ve Dy ortak katkılı $Sr_4Al_{14}O_{25}$ (S4A7ED) 30-40 mol% B_2O_3 ile sentezlenen kompozisyonlar en uzun ısrarlı ışımayı sergiledi ve bu kompozisyonlar en yüksek miktarda uzun ışıma fazlarına sahip değildir. Elektriksel yüklü köprü yapmayan oksijenlerin S4A7ED kristal yapısına girebilmesi için optimum miktarda B gereklidir. Ayrıca, Si, P ve Zr gibi diğer cam yapıcı öncülerin kullanılmasının da S4A7ED bileşiklerin ısrarlı ışıma süresini uzattığı gösterilmiştir. Bu durum köprü kurmayan

oksijenlerin yapıya girmesi sonucu oluşan yapısal değişimlerden kaynaklıdır. Bu çalışmada ortaya çıkan deneysel kanıtlar ışığında yeni bir uzun süreli parlama gösteren bileşik sınıfının keşfedildiği düşünülmektedir.

ACKNOWLEDGEMENTS

I would like to express my sincere gratitude to everyone who helped and supported me during this thesis work. I owe many thanks to all of them.

Foremost I would like to thank my supervisor Prof. Cleva W. OW-YANG, for her patience, great suggestions and supervision throughout my doctoral journey. I am very grateful for her support and constructive criticism of every details of my PhD studies. I learned a lot from her about how to be professional and productive. I feel very privileged to be part of her research group. She encouraged me to be more confident and think outside the box. She always gave the best advice when I needed it and I am so grateful that she has been a part of my life.

I would like the thanks to Prof. Mehmet Ali Gülgün (Mali Hoca) for his valuable advices about life and about research problems. He is the most cheerful professor I have ever known and he had always been generous with sharing his knowledge in research discussions. His door was always open to talk about everything in life.

I also would like to thank to my dissertation jury members, Assoc. Prof Aligül Büyükaksoy, Prof. Servet Turan and Assoc. Prof. Mirijam Vrabec for their insightful comments, which helped me to improve this work further.

I would like to thank Richard Bormett of Renishaw Inc for his guidance on Raman data processing. His expert comments helped me a lot and I am very grateful for that.

I would also thank to Sibel Kasap and Koray Bahadır Dönmez for helping me with Raman spectroscopy. They were always available when I needed someone to discuss Raman spectroscopy problems.

I am grateful to Turgay Gönül who had been always available to help and trained me on many characterization devices. He always had a great suggestions and knowledge about the problem that I had. I am very grateful for his help whenever I needed.

I would like to thank all the group members, Dr, Sirous Khabbaz Abkenar Dr. Güliz Inan Akmehmet, Dr. Hasan Kurt, Dr. Ali Ansari Hamedani, Zeki Semih Pehlivan, Ece Günay, Ece Deniz, Ayça Şenol Güngör, Ipek Efe, İren Efe, Defne Çirci, Ahmet Alper Özkan for their friendship and insightful discussions. It was my great pleasure to be a member of such a strong research team with knowledgeable humble and fun people.

I thank all my friends in Sabancı University; Melike Gezen, Ece Arıcı, Ferdows Seyedeh, Liyne, Dilek, Aygül, Mehmet Can, Yasemin and many others which I forgot to mention their names. I am thankful to each of them for bringing good memories to my life. I would like to thank my dear friend Merve Buldu for her friendship and support. She flourished the time that I spent at university.

I also would like to thank all the SU MAT family and it has been a privilege to be part of it.

I want to give special thanks to my beloved family. You have always been there for me, no matter what, and selflessly supported me. I feel truly blessed. My source of happiness is my niece Neva and Erdem, thank you for always bringing me happiness. I want to honor my angel grandmother; I wish she could see my graduation.

Last on the list, but far from the least priority, I want to thank my husband for his endless love and support for many years. I am so lucky to have him in my life. He was always by my side to encourage and motivate me in all difficult times. He is my true inspiration and I love him deeply.

I would like to acknowledge to the Sabancı University Internal Research Grant program (Grant #I.A.CF-18-01887) and Tübitak 119M840 project for the financial support.

TABLE OF CONTENTS

LIST OF FIGURES

LIST OF TABLES

LIST OF ABBREVIATIONS

Al	Aluminum
Ar	Argon
B	Boron
BO	Bridging oxygen
CA	Citric Acid
CIF	Crystallographic Information File
DCLS	Direct Classical Least Squares
Dy	Dysprosium
EG	Ethylene Glycol
Eu	Europium
FTIR	The Fourier transform infrared
ICSD	Inorganic Crystal Structure Database
MCR ALS	Multivariate curve resolution - alternate least squares
NBO	Non-bridging oxygen
O	Oxygen
P	Phosphorus
PersiL	Persistent Luminescence
PCA	Principle Component Analysis
PL	Photoluminescence
SA	$SrAl_2O_4$
SA2	$SrAl_4O_7$

SA6	$SrAl_{12}O_{19}$
S4A7	$Sr_4Al_{14}O_{25}$
SAB	Strontium Aluminoborate
S4A7ED	$Sr_4Al_{14}O_{25}$ co-doped with Europium and Dysprosium
S4A7EDB	$Sr_4Al_{14}O_{25}$ co-doped with Europium and Dysprosium with Boron
Si	Silicon
XRD	X-Ray Diffraction
V	Vanadium
Zr	Zirconium

CHAPTER 1: INTRODUCTION

Persistent luminescence pigments are widely investigated due to their various application areas such as safety signage and paint. Eu^{2+}, Dy^{3+} and B co-doped $SrAl_2O_4$ (SAED) and $Sr_4Al_{14}O_{25}$ (S4A7EDB) compounds are exhibit persistent luminescence. Boron oxide, initially used as a sintering flux agent to facilitate synthesis at lower temperatures and grain growth of stoichiometric, was noted to extend persistent luminescence in Eu and Dy co-doped $SrAl_2O_4$ (SAED) and S4A7ED from ca. 10 minutes to longer than 10 h [1–3]. Understanding the exact role of B in the formation of the atomic arrangements has motivated investigation into its location and crystal environment [4]. Nag had reported the existence of BO_4 units, as revealed by NMR and FTIR [5], which was confirmed by analysis of the B-K ionization edge energy loss near-edge structure (ELNES) [4].

$SrO\text{-}Al_2O_3$ system has five main phases based on the stoichiometry such as $SrAl_2O_4$ (SA), $SrAl_4O_7$ (SA2), $Sr_4Al_{14}O_{25}$ (S4A7), $SrAl_{12}O_{19}$ (SA6) and $Sr_3Al_2O_6$ (S3A) and only S4A7 and SA phases associated with an extended afterglow at room temperature. Both of the SA and S4A7 phase consists of chains (AlOx) polyhedra forming a rigid 3-D scaffold, with large cavities filled by Sr cations providing electrical charge balance. In this thesis, we focused on effect of boron incorporation into S4A7 phase.

The crystal structure of $Sr_4Al_{14}O_{25}$ is as shown in Figure 1.1 (a). $Sr_4Al_{14}O_{25}$ crystallizes in the orthorhombic space group Pmma with unit cell parameters of a = 24.785 Å, b = 8.487 Å, c = 4.886 Å; V = 1027.772 $Å^3$; $\alpha = \beta = \gamma = 90°$. A network of corner- and edge-sharing alumina polyhedra defines a scaffold—*i.e.*, chains of octahedra (Figure 1.1 (b)), sharing a single edge, defines the scaffold columns—, while chains of corner-sharing tetrahedra bridge the columns (Figure 1.1 (c)). Sr^{2+} cations provide charge compensation

in large interstitial cavities in two crystallographically non-equivalent sites: Sr1 coordinated by 10 oxygen and of Wyckoff symmetry 4*j* and Sr2 coordinated by 7 oxygen and of Wyckoff symmetry 4*i* (Figure 1.1 (d)).

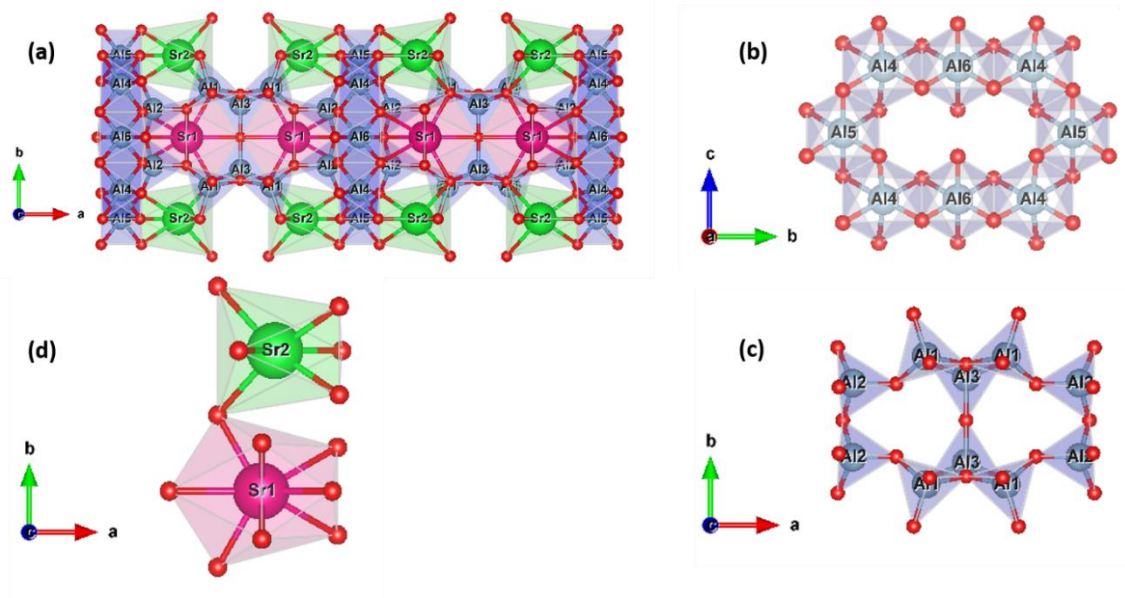

Figure 1.1 a) Components of the $Sr_4Al_{14}O_{25}$ unit cell viewed along the [001]; b) 6 oxygen-coordinated alumina scaffold; c) 4 oxygen-coordinated alumina scaffold; d) the coordination polyhedra of Sr (1) site (Wyckoff 4j) and Sr (2) site (Wyckoff 4i).

B_2O_3 also functions as a structural network former in oxide glasses. Network formers forms polyhedral units in a glass network structure, and they are covalently bonded with oxygen[6][7]. Network modifiers, on the other hand, contribute non-bridging oxygen, which do not link completely link all of the polyhedral units. Alkaline oxides and alkali earth oxides are the common modifiers, and their presence is usually to maintain local electrical charge neutrality [8][9]. Network intermediates either act as glass formers or modifiers, depending on the local network structure and composition [8][6]. The structure of boron oxide is corner-sharing triangular polyhedra and vitreous boron oxide has planar boroxol ring trigonal uncharged [BØ3] network structure where Ø indicates bridging oxygen, O for non-bridging oxygen [10]. Combinations of basic borate structural units form superstructural units, such as metaborate $[BØ_2O]^-$, pyroborates $[BØO_2]^{2-}$, orthoborates $[BO_3]^{3-}$, and $[BØ4]^-$ tetrahedra [7].

The change in structural function of boron oxide is commonly referred to as the boron anomaly. With the addition of modifier oxides, planar trigonal charge-neutral (BO_3) moieties initially transform to negatively charged, tetrahedral $[BO_4]^-$ of 3-D character. However, upon further modifier addition, the number of non-bridging oxygen increases, breaking up the oxide network connectivity [10–12]. At higher modifier content, the coordination number of boron converts back from four to three, in the form of complex triangular [BØ$_3$] structures—ones with non-bridging oxygen on meta $[BØ_2O]^-$, pyro $[BØO_2]^{2-}$ and finally ortho $[BO_3]^{3-}$ units[7,13]. While boron effectively densifies the aluminum polyhedra at low modifier concentrations, at elevated modifier concentrations, non-bridging oxygen presence yields increased free volume in the network. The structural connectivity of borate-containing glass is thus determined by the relative amount of 3- and 4-coordinated boron, and the relative ratio can be defined as N4 (= B4/ (B3+B4).

Aside from B_2O_3 , other oxide glass forming cations, such as Si, P, V, and Zr, have also been used to produce afterglow compounds, such as rare-earth doped silicates and phosphates[14–20]. SiO_2 and P_2O_5 glass structure consist of interconnected polyhedra of oxygen-coordinated cations that share bridging oxygen anions. Vitreous silica glasses are 3-D networks of SiO_4 tetrahedral units and vitreous phosphate is composed of PO_4 tetrahedral units (Figure 1.2). When a modifier cation, such as alkaline or alkaline earth cations, enters these oxide networks, some bridging oxygen become non-bridging ones, due to differences in valence. The Q^n notation was developed to facilitate discussion distinguishing polyhedral units containing different numbers of bridging oxygen (BO) and NBO. Q represents the polyhedral unit; *n* represents the number of bridging oxygen, while *n*-1 represents the number of non-bridging oxygen per tetrahedron**.** The increase in the fraction of network modifier cations in the glass system promotes the presence of Q^{n-1} units at the expense of Q^n units [21]**.**

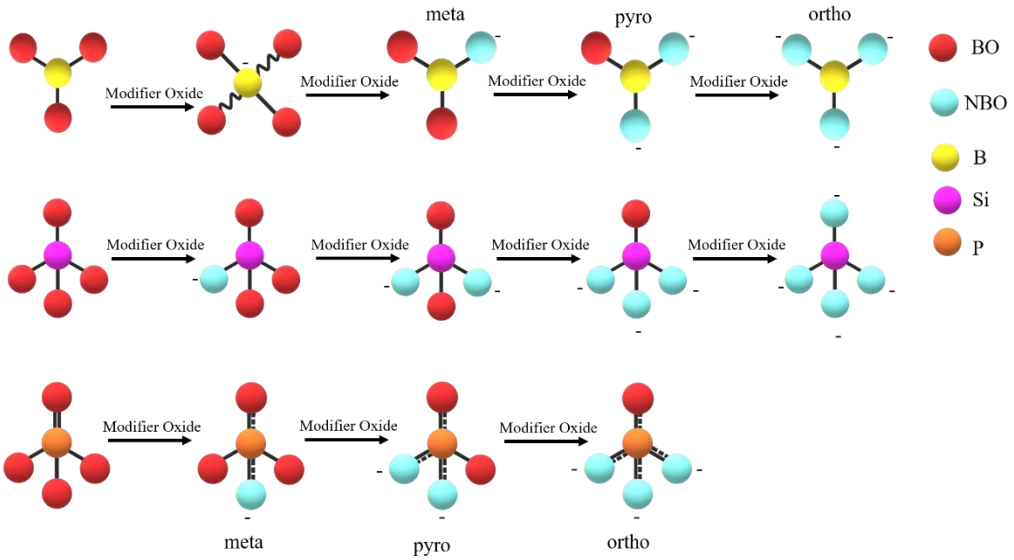

Figure 1.2 Structural changes of glass series with modifier oxide addition.

In previous studies, vibration spectroscopy techniques have proved useful in determining the structure and local environment in polymorphic crystal structure and in glassy ones. The Raman modes of $SrAl_2O_4$ (SA) have also been considered in several studies [22–24]. Meanwhile, crystal structure changes due to dopant and impurity incorporation have been studied with Raman spectroscopy [25]. Raman and infrared spectroscopy are commonly used as complimentary techniques for elucidating the local structure in modified glass and crystalline structures [26–32].

In this work, we have observed that although Eu and Dy co-doped $Sr_4Al_{14}O_{25}$ (S4A7ED) synthesized with 30-40 mol% B_2O_3 displayed the longest duration of PersiL, these compositions do not contain the highest amount of the long persistence phases. To elucidate how the structural arrangement of atoms in S4A7EDB induced by synthesis using 30-40 mol% B_2O_3 yields the longest persistence, the crystal environment of B in S4A7ED was evaluated by using Raman and FTIR spectroscopy. FTIR and Raman spectra revealed that S4A7ED doped with 30-40 mol% B_2O_3 compositions contained polyborate supramolecular arrangements, like neutral trigonal $BØ_3$ units, charged $BØ_4^-$ tetrahedra, metaborate $BØ_2O^-$.

In this thesis, we also investigated the correlation between other oxide glass forming cations—Si, P, Zr and V—and their capability for extending PersiL in S4A7ED. To understand the structural changes that these cations impart to the atomic arrangements inside the S4A7ED crystal structure, we used FTIR and micro-Raman spectroscopy and evaluated the impact of charged NBOs. Our results demonstrated that use of oxide glass forming precursors of Si, P, and Zr during Pechini processing also extended PersiL in S4A7ED compounds.

To understand how B_2O_3, SiO_2, P_2O_5, V_2O_5, and ZrO_2 content tunes the structure a luminescence behavior of S4A7ED, the crystal environment of cations was investigated by micro-Raman and FTIR spectroscopy. The structural investigation of the S4A7ED doped with different glass former cations was carried out with X-ray diffraction (XRD) and quantitative Rietveld phase analysis. VESTA software used for viewing crystal structures—reference ones and refined ones. The luminescence behavior of S4A7ED doped with different glass formers was investigated by photoluminescence spectroscopy.

CHAPTER 2: EXPERIMENTAL TECHNIQUES

2.1 Introduction

The $SrO\text{-}Al_2O_3$ system has five main phases based on stoichiometry such as $SrAl_2O_4$ (SA), $SrAl_4O_7$ (SA2), $Sr_4Al_{14}O_{25}$ (S4A7), $SrAl_{12}O_{19}$ (SA6), and $Sr_3Al_2O_6$ (S3A) as seen in Figure 2.1. All these phases were synthesized with different techniques for structural investigation. The phase pure strontium aluminate compounds were synthesized with sol-gel Pechini and solid-state techniques. Strontium aluminate compounds coped with Eu, Dy, and glass-forming cations were synthesized with the sol-gel Pechini method.

General material characterization techniques were employed to evaluate the crystal environment of glass former cations in strontium aluminate, to elucidate the relationship between composition, structure, and luminescence. The characterization tools used for the analysis: X-ray diffraction analysis (XRD), Rietveld refinement of the XRD data, Raman spectroscopy, FTIR Spectroscopy, Photoluminescence spectroscopy (PL-PLE), and afterglow decay time measurements.

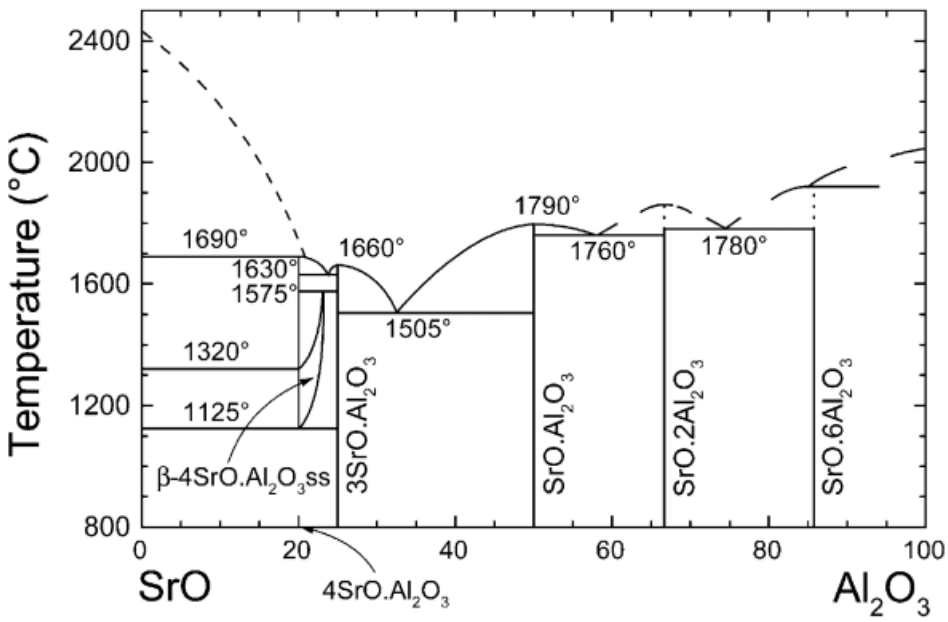

Figure 2.1 $SrO\text{-}Al_2O_3$ phase diagram (Reprinted from [33] with permission of Elsevier).

2.2 Chemical Processing of Strontium Aluminate Compounds

S4A7ED*x*B, where $0 \leq x \leq 60$ mol% B_2O_3 compositions synthesis via modified Sol-gel Pechini process. Sol gel process is a phase transformation from liquid to cross link gel through a polymerization reaction. All chemicals used for the synthesis of S4A7EDxB with $0 \leq x \leq 60$ mol% B_2O_3 phosphors are summarized in Table 2.1.

Table 2.1 Precursors list for the modified Pechini sol-gel synthesis of S4A7ED*x*B, where $0 \leq x \leq 60$ mol% B_2O_3.

Precursor name	**Chemical Formula**	**Provider**
Aluminum nitrate nonahydrate	$Al(NO_3)_3.9H_2O$	Merck / 99.9%
Strontium nitrate anhydrous	$Sr(NO_3)_2$	Merck / Extra pure
Europium (III) nitrate hexahydrate	$Eu(NO_3)_3.6H_2O$	Alfa Aesar /99.99%
Dysprosium (III) nitrate pentahydrate	$Dy(NO_3)_3.5H_2O$	Alfa Aesar /99.99%
Boron trioxide	B_2O_3	Alfa Aesar /99.98%
Citric acid monohydrate	$C_6H_8O_7.H_2O$	Merck / 99.5%
Ethylene glycol	$C_2H_6O_2$	Carlo Erba/99.5%

First 300 mL of deionized water was boiled in a glass beaker on a hot plate and then stoichiometric amounts of the precursors were added to the boiling with under continuous stirring with the order in the list. The solutions were kept mixed with a magnetic stirrer after the addition of all precursors for about 20 minutes to make sure the precursor was properly mixed and dissolved as shown in Figure 2.2.

Then the aqueous solution was placed into the box furnace at the temperature of 120 °C for 24 for the evaporation of the water and the gelation process. After the drying stage, voluminous sponge-like amorphous material was obtained. The material was ground into a powder in an agate mortar with a pestle for heat treatment and thermal analysis.

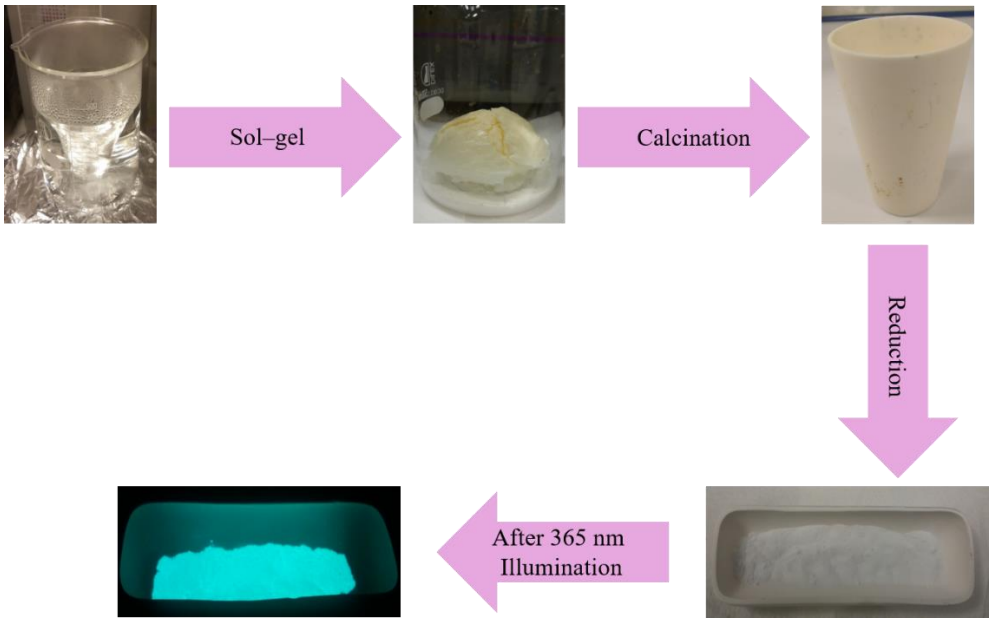

Figure 2.2 The synthesis scheme of strontium aluminate compounds by sol-gel Pechini method.

Heat treatment procedure that followed based on the thermal analysis results to obtain crystalline $Sr_4Al_{14}O_{25}$ compound doped with 1 at % Eu, 1 at % Dy and $0 \leq x \leq 60$ mol% B_2O_3

(S4A7ED*x*B, where $0 \leq x \leq 60$ mol% B_2O_3,) with persistent luminesce properties.

I. The completely dried and ground amorphous powders were transferred to the alumina crucible and placed in the box furnace. The box furnace was heated from room temperature to 600°C at a heating rate of 10°C/min for 6 hours under an oxidizing atmosphere to combust the organics.

II. Then the furnace temperature was heated up from 600°C to 1150 °C with a heating rate of 10 °C/min for 10 hours under oxidizing atmosphere to obtain the S4A7 phase. The furnace cooled down to room temperature with a cooling rate of 10 °C/min. After the calcination, white crystalline powder was ground for the next step.

III. The powder was transferred into alumina crucible and then placed into the reduction furnace. The reduction procedure was applied to the powder to reduce Eu^{3+} to Eu^{2+}. The reduction furnace was heated up from room temperature to 1150 °C with a heating rate of 10 °C/min. When the furnace heat reached to target temperature, the reducing atmosphere (96 wt% Ar and 4 wt% H_2) was applied for 4 hours with a flow rate of 120 mL/min through the reduction process. After reduction, the powder was cooled down in the furnace to room temperature, and the reducing atmosphere was kept until the furnace temperature dropped to below 500 °C. The yellowish-white powder was obtained at the end of the heat treatment.

$Sr_4Al_{14}O_{25}$ compounds doped with 1 at% Eu, 1 at% Dy was synthesized by a sol-gel Pechini process as described above. Each compound was prepared with m = 3, 10 and 30 mol% oxide glass former precursors. The compositions were named as S4A7EDm*X*, where *X* represented the oxide glass former precursor: B_2O_3, TEOS, H_3PO_4, ZrO_2, or V_2O_5. All chemicals used for synthesis are listed in Table 2.2

Table 2.2 Precursors list for the modified Pechini sol-gel synthesis of S4A7EDm*X* compounds.

Precursor name	**Chemical Formula**	**Provider**
Aluminum nitrate nonahydrate	$Al(NO_3)_3.9H_2O$	Merck / 99.9%
Strontium nitrate anhydrous	$Sr(NO_3)_2$	Merck / Extra pure
Europium (III) nitrate hexahydrate	$Eu(NO_3)_3.6H_2O$	Alfa Aesar /99.99%
Dysprosium (III) nitrate pentahydrate	$Dy(NO_3)_3.5H_2O$	Alfa Aesar /99.99%
Phosphoric Acid	H_3PO_4	Alfa Aesar /99.98%
Tetraethyl orthosilicate	$Si(OC_2H_5)_4$	Aldrich /99.0%
Zirconyl chloride octahydrate	$ZrOCl_2 \cdot 8H_2O$	Alfa Aesar
Vanadyl acetylacetonate	$OV(C_5H_7O_2)_2$	Alfa Aesar
Citric acid monohydrate	$C_6H_8O_7.H_2O$	Merck / 99.5%

Different reduction conditions were applied to the S4A7ED*mX* compounds to obtain the persistent luminescent powders. Table 2.3 summarized the applied reduction conditions.

Table 2.3 The reduction conditions for the S4A7ED*mX* compounds.

S4A7EDm*X* Compounds	**Reduction Condition**
S4A7ED 30 mol % TEOS	1150 °C - 4h - flow 60
S4A7ED 10 mol % H_3PO_4	1150 °C - 4h - flow 60
S4A7ED 3 mol % $ZrOCl_2$	1150 °C - 4h - flow 60
S4A7ED 10 mol % $VO(Ac)_2$	1150 °C - 1h - flow 60

Strontium aluminate compounds with< 90% phase purity, were prepared with sol-gel Pechini and solid state techniques. Processing conditions were optimized for each composition to obtain a single-phase compound. Optimization parameters are summarized in Figure 2.3.

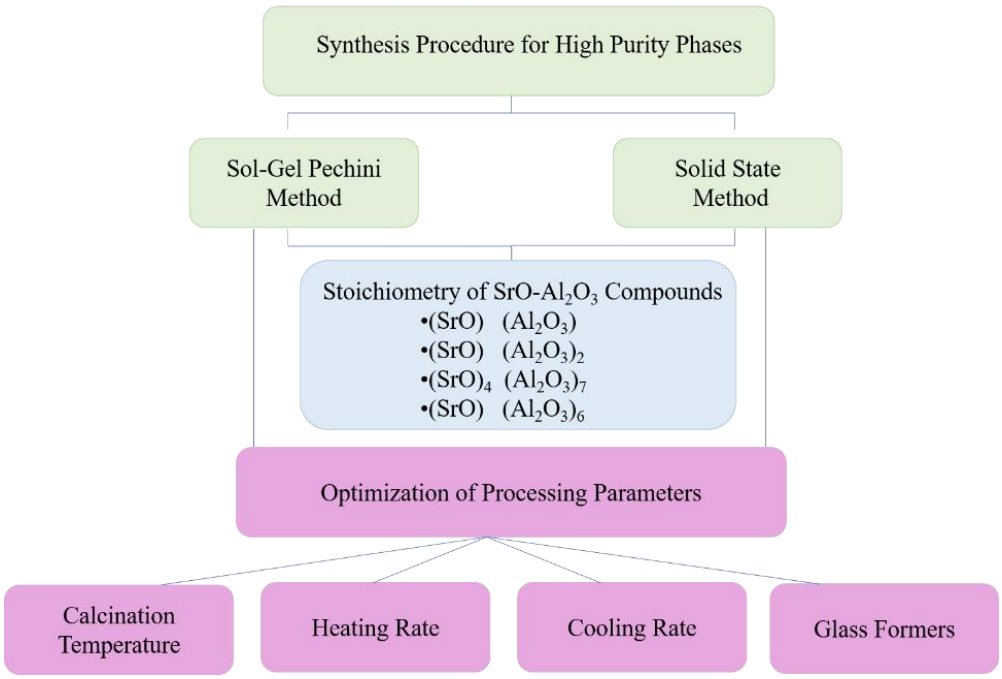

Figure 2.3 Synthesis procedure for the high purity phases.

Solid-state synthesis of strontium aluminate was initiated by adding the stoichiometric amount of $SrCO_3$, and Al_2O_3 as starting materials according to the intended phase. To

produce a homogenous mixture, these materials were ball milled using a planetary mill at 600 rpm rotations for several hours in an acetone medium. The well-mixed batch was dried at room temperature and mildly ground in agate mortar with a pestle for the heat treatment step. Table 2.4 shows the parameters applied to obtain high purity phases.

Table 2.4 Synthesis conditions for $SrO\text{-}Al_2O_3$ high purity phases.

Phase	Synthesis Method	Processing Parameters
SA	Solid State	1000°C/30K/30min/Quenched
SA2	Sol-gel Pechini	1000°C/5K/10h/Quenched
S4A7	Sol-gel Pechini	1300°C/10K/24h/Quenched
SA6	Sol-gel Pechini	1200°C/30K/20h/Quenched

2.3 Characterization Tools

2.3.1 X-ray Diffraction Characterization

Analysis of the crystal structure and phase identification were performed by powder XRD analysis (Bruker AXS, D8 Advance: Cu-Kα source (λ =1.54056 Å), scanning rate 1s per step, 0.02° increment, over a 2θ range of 10° to 90°). Phase analysis of the diffraction patterns was performed by using search matches from the International Centre for Diffraction Data (ICDD) database in DIFRACT.SUITE EVA software (Bruker AXS, Germany): orthorhombic $Sr_4Al_{14}O_{25}$ (S4A7) PDF No 74-1810, monoclinic $SrAl_4O_7$ (SA2) PDF No 70-1479, hexagonal $SrAl_{12}O_{19}$ (SA6) PDF No 70-0947, and monoclinic $SrAl_2O_4$ (SA) PDF No 74-0794.

The DiffracPlus TOPAS 4.2 software package (Bruker AXS, Karlsruhe, Germany) [34] was used for structural analysis by the X-ray Rietveld refinement method with corresponding crystallographic information files (CIF) of the identified phases from Inorganic Crystal Structure Database(ICSD; FIZ Karlsruhe 2019, version 4.2.0) [35] and FindIT crystal database software.

During Rietveld analysis, the background coefficient was determined as a 6-coefficient polynomial function. Structural parameters of each of the phases were refined starting with the dominant phase. At the end of the Rietveld refinement, refined structural parameters were inserted into Vesta software and used for visualizing the refined crystal structures[36]. DIFRACT.SUITE EVA (Bruker AXS, Germany) was used for determining the percent crystallinity.

2.3.2 Fourier Transform Infrared

The Fourier transform infrared (FTIR) technique was used to determine the structure and local environment of glassy systems and polymorphic crystal structures. FTIR measurements of the four main phases of the $SrO\text{-}Al_2O_3$ compounds were collected before the doped compounds to use as a reference spectrum. FTIR spectra were collected on a Nicolet IS10 FTIR spectrometer (Thermo Scientific, USA) with ATR mode in the range of 4000 to 600 cm^{-1} using resolution of 4 cm^{-1} at 128 scans. Spectral processing and analysis were performed using the program Omnic (Thermo Scientific) program [37] and the software program Fityk® version 1.3.1 for spectral deconvolution [38].

2.3.3 Raman Spectroscopy

Dopant induces structural changes of strontium aluminates compound investigated with Raman spectroscopy. Phase-pure, SA, SA2, S4A7 and SA6 compounds were characterized to serve as a reference fingerprint for Raman spectrum analysis. Micro-Raman analysis was performed on polished sintered ceramic pellets with using a Raman system (Renishaw inVia) mounted on a confocal microscope: λ_{ex} = 532 nm, 10 s exposure, 1 cm^{-1} spectral resolution; system calibrated to 520 cm^{-1} of Si. A representative dataset was ensured via measuring at 5 different locations. The manufacturer provided WiRE 3.4 software application was used for data acquisition and analysis by multivariate curve resolution-alternating least squares (MCR-ALS) method using Empty Modelling™. The baseline correction was performed to a 5^{th} order polynomial, and

spectral deconvolution analysis was performed using Fityk® [38]. The details of data interpretation were explained in Chapter 5.

2.3.4 Afterglow Persistence

Afterglow persistence of S4A7ED*x*B samples ($0 \leq x \leq 60$ mol% B_2O_3) were collected by using a custom-built optical bench photoluminescence system consist of a photomultiplier tube (H7421; Hamamatsu Photonics Deutschland GmbH, Herrsching, Germany) coupled with photon counting unit (C-8855, Hamamatsu Photonics Deutschland GmbH), after illuminating the powder with a 365 nm UV light source with for 10 minutes, and then recorded for up to 14 h.

The intensity of luminescence emission by S4A7ED*mX* samples was measured using an in-house system—i.e., one consisting of a high-speed Si PIN photodiode (Melles Griot 13DAH005) and a source meter (Keithley 2400). This system was calibrated using an AM1.5G solar simulator with an emission power of 100 $mW \cdot cm^{-2}$ and a set of reflective neutral density filters (Thorlabs NDK01). The readout was carried out after a strictly observed 10 minutes of UV irradiation at wavelength of 365 nm, using a 6 W Hg vapor lamp.

2.3.5 Photoluminescence Spectroscopy

Photoluminesence spectroscopy was used the analyze excitation and emission behavior of Eu^{2+} hosted in multiple crystal environments of strontium aluminates. PLE/PL measurements were recorded using an Agilent Cary Eclipse Spectrofluorometer. The set up power turned on to allow the light source to warm up and stabilize for about 20 minutes. A small amount of powder was placed between the two glass coverslips and the edges were tightly tied to prevent it from falling. Table 2.5 summarizes the measurement range with maximum excitation and emission values for each compound.

Table 2.5 PL/PLE measurement range with maximum excitation and emission values for each hero S4A7ED*mX* compounds.

Composition	**λ_{ex} range (nm)**	**λ_{ex} (nm)**	**λ_{em} range (nm)**	**λ_{em} (nm)**
S4A7ED 30 mol% B_2O_3	300-450	354	380-700	490
S4A7ED 30 mol% TEOS	300-450	337	360-700	495
S4A7ED 10 mol % H_3PO_4	300-450	337	360-700	406
S4A7ED 3 mol% $ZrOCl_2$	300-450	420	450-700	496
S4A7ED 10 mol% $VO(Ac)_2$	300-450	420	450-700	490

CHAPTER 3: BORATE POLYANIONS TUNING PERSISTENT LUMINESCENCE IN EUROPIUM AND DYSPROSIUM CO-DOPED STRONTIUM ALUMINATE

This ***Chapter 3*** has been published in:

Coşgun Ergene A, Khabbaz Abkenar S, Deniz E, Ow-Yang CW. Borate polyanions tuning persistent luminescence in Eu and Dy co-doped strontium aluminate. Mater Adv 2022;3:3238–50. https://doi.org/10.1039/D1MA01234G.

3.1 Introduction

Eu^{2+}, Dy^{3+} and B co-doped $Sr_4Al_{14}O_{25}$ (S4A7EDB) is well known to exhibit persistent luminescence. Boron oxide, initially used as a sintering flux agent to facilitate synthesis at lower temperatures and grain growth of stoichiometric, was noted to extend persistent luminescence in Eu and Dy co-doped $SrAl_2O_4$ (SAED) and S4A7ED from *ca.* 10 minutes to longer than 10 h [1–3]. Understanding the exact role of B in forming the crystal structure has motivated investigations into its location and crystal environment [4,5,39]. Nag had reported the existence of BO_4 units, which were revealed by NMR and FTIR [5], and which was confirmed by spatially resolved analysis of the B-K ionization edge energy loss near-edge structure (ELNES) [4]. Boron incorporation in RE co-doped S4A7 was also associated with a blue shift in emission at 400 nm, which was attributed to lattice shrinkage [39]. Additional peaks were observed in the photoluminescence (PL) and

thermoluminescence (TL) spectra, which were interpreted as additional traps due to the incorporation of B into the SAED crystal structure [40]. To explain the role of boron, theoretical studies suggested the clustering of the point defects, Eu^{2+}, Dy^{3+}, B, and oxygen vacancy [41]. In nano-S4A7 produced by a microemulsion method, 15-20 mol% has been reported as the optimum boric acid concentration for maximum intensity and duration of the persistent luminescence [42].

B_2O_3 is known to serve as a network former in oxide glasses, where it forms polyhedral units due to being covalently bonded with charge-screening oxygen [6,7]. Each oxygen is saturated, *i.e.*, bonded to 2 cations. Network modifiers, on the other hand, contribute non-bridging oxygen to the network. Because they do not completely link the maximum number of polyhedral units—*i.e.*, 2 units per oxygen—their presence lowers network connectivity, resulting in more open networks. Alkaline oxides and alkali earth oxides are common modifiers, and the presence of their cations provides local electrical charge neutrality [8,9]. Network intermediates act as glass formers or modifiers, depending on the local network structure and composition [6,8]. The structure of boron oxide consists of corner-sharing triangular polyhedra. Vitreous boron oxide has planar six-membered boroxyl rings containing trigonal uncharged [$BØ_3$], where Ø indicates bridging oxygen, O for non-bridging oxygen [10]. Combinations of basic borate structural units form superstructural units, such as borate rings, diborates, metaborate ring-chains, and pyroborate dimers, etc. [7,43,44].

Cation additions can change the oxide network character. For example, B_2O_3 incorporation into alumina glass induces changes in the types and connectivity of borate and aluminate structural units. Boron oxide functions as both former and modifier in alumino-borate (Al_2O_3-B_2O_3) networks, depending on their relative concentration ratio[11].

The change in structural function of boron oxide is commonly referred to as the boron anomaly. With the addition of modifier oxides, planar trigonal charge-neutral [$BØ_3$] triangles initially transform to negatively charged, tetrahedral $[BO_4]^-$ of 3-D character. Upon increasing modifier addition to Al_2O_3-B_2O_3, the number of non-bridging oxygens increases, breaking up the oxide network connectivity [10–12]. Above a critical modifier

concentration, the coordination number of boron converts back from four to three, in the form of complex triangular moieties—ones with non-bridging oxygen on meta $[B\O_2O]^-$, pyro $[B\OO_2]^{2-}$ and finally ortho $[BO_3]^{3-}$ units [7,13]. Thus while boron effectively densifies the alumina polyhedral network at low modifier concentrations, the increase in non-bridging oxygen yields increased free volume in the network at elevated modifier concentrations. The structural connectivity of borate-containing glass can be quantified by the relative amount of 3- and 4-coordinated boron, with the relative ratio defined as N4 = (B4/ (B3+B4)). This metric facilitates the correlation of structure to optical and thermal properties.

The role of oxides in the complex strontium aluminate $SrO\text{-}Al_2O_3\text{-}B_2O_3$ network depends on composition. Al^{3+} ions can be either a network former in Al_2O_3, forming AlO_4 tetrahedra, or network modifier, by contributing non-bridging oxygen in the formation of AlO_6 octahedra [11,21,45]. Sr^{2+} ions are network modifiers in SrO, where they break up the network and provide charge compensation in interstitial sites [46]. B_2O_3 can provide charge compensation to stabilize Al polyhedra [11].

Previous work in our group revealed the significant and multi-functional role of boron in the structural evolution of S4A7EDB during Pechini processing. Boron was associated with RE incorporation into adjacent Sr^{2+} sites in S4A7 [47], as well as with a more uniform distribution of RE dopants in Sr^{2+} sites across the microstructure by nanoCL analysis [3]. The boron-rich intergranular phase enabled tuning of RE dopant concentration in S4A7 grains to reach their solubility limits, to avoid concentration quenching [4]. In addition, trigonally coordinated boron was observed in the intergranular phase, while it was primarily of tetrahedral coordination in the S4A7 grains[4]. We also observed that processing with boron oxide not only lowered the temperature needed for the crystal structure of S4A7 to form, but also modified the diffusion kinetics of Eu and Dy, in playing a role in extending afterglow persistence in S4A7EDB [3,4,47]. Finally, the amount of boron oxide used in Pechini processing of S4A7EDB influenced the duration of persistent luminescence, with the longest in compounds containing 30-40 mol% B_2O_3. Interestingly, the total amount of long afterglow phase was not at the maximum when this amount of B_2O_3 is used [48].

In previous studies, vibration spectroscopy techniques have proved useful in determining the structure and local environment in polymorphic crystal structure and in glassy ones, as well as those of borates. The Raman modes of $SrAl_2O_4$ (SA) have also been considered in several studies [22–24]. Meanwhile, crystal structure changes due to dopant and impurity incorporation have been studied with Raman spectroscopy [25]. Raman and infrared spectroscopy are commonly used as complimentary techniques for elucidating the local structure in modified glass and crystalline structures [26–32]. Keiner and co-workers demonstrated the use of micro-Raman and FTIR to correlate spatially resolved information about molecular and network structures [49].

In this work, to understand how the B_2O_3 content tunes the structure and luminescence behavior of S4A7ED, we synthesized S4A7EDB by Pechini processing using different amounts of B_2O_3; analyzed the phase composition and changes to atomic arrangements in the crystal structure by XRD, the crystal environment of B by micro-Raman and FTIR spectroscopy, and measured the duration of persistent luminescence by afterglow decay.

3.2 Results

The afterglow decay lifetime of S4A7EDxB, where $0 \leq x \leq 60$ mol% B_2O_3, was recorded for 14 hours under ambient conditions after being illuminated with UV light source (λex = 365 nm) for 10 minutes, and the decay curves are summarized in Figure 3.1 (a). All S4A7 powders exhibited persistent luminescence, regardless of B_2O_3 content. The longest persistence luminescence was observed in the x = 30 mol% B_2O_3 and 40 mol% B_2O_3 compounds. Figure 3.1 (b) shows the afterglow decay curves for S4A7EDxB ($30 \leq x \leq$ 40 mol% B_2O_3).

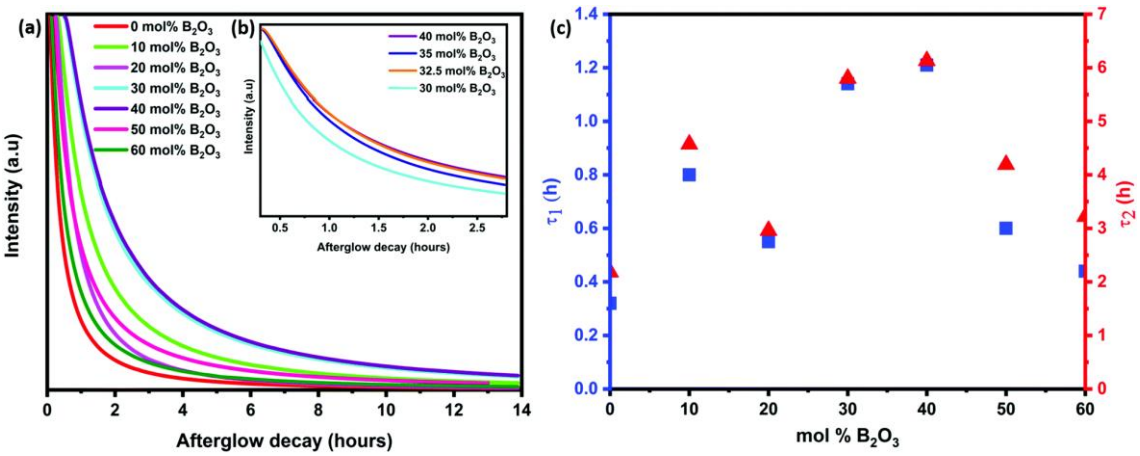

Figure 3.1 a) Afterglow decay curves for S4A7ED*x*B ($0 \leq x \leq 60$ mol% B_2O_3); b) Afterglow decay curves for S4A7ED*x*B ($30 \leq x \leq 40$ mol% B_2O_3); c) decay time constant analysis of S4A7ED*x*B ($0 \leq x \leq 60$ mol% B_2O_3) samples: τ_1 for relaxation from shallow traps; τ_2 for relaxation from deep traps.

The two-slope behavior in the decay curves indicated 2 independent de-trapping mechanisms, corresponding to τ_1 and τ_2 respectively, which was obtained from the decay-curve fitting equation:

$$I = \alpha_1 \exp\left(\frac{-t}{\tau_1}\right) + \alpha_2 \exp\left(\frac{-t}{\tau_2}\right)$$

Eq (3.1)

α_1 and α_2 are constants, τ_1 and τ_2 are the decay lifetimes times, as shown in Figure 3.1 (c). The two different lifetimes, τ_1 and τ_2, indicate rapid and slow components of radiative relaxation. The S4A7ED*x*B compound with x = 30 mol% B_2O_3 doped composition had τ_1 = 1 h, τ_2 = 5.8 h, while the x = 40 mol% B_2O_3 doped one showed τ_1 = 1.21 h, τ_2 = 6.13 h.

To determine the phase composition of S4A7EDxB, where $0 \leq x \leq 60$ mol% B_2O_3, all samples were analyzed using XRD (Figure 3.2). Calibration of the instrument was performed using a corundum standard. The evolution in the main (421) diffraction peak with B_2O_3 content is shown in Figure 3.2 (b), across the entire composition range studied, with an emphasis on peak shifts in the $20 \leq x < 40$ mol% B_2O_3 compositions in Figure

3.2 (c). The main diffraction peaks corresponding to the crystallographic planes (421), (021), and (420) shifted from the reference positions with the addition of B_2O_3 for $0 < x < 40$ mol%. In S4A7EDxB compounds with $20 \leq x < 40$ mol% B_2O_3, the (421) shifted toward lower d-spacing (Figure 3.2 (b) and 3.2 (c)).

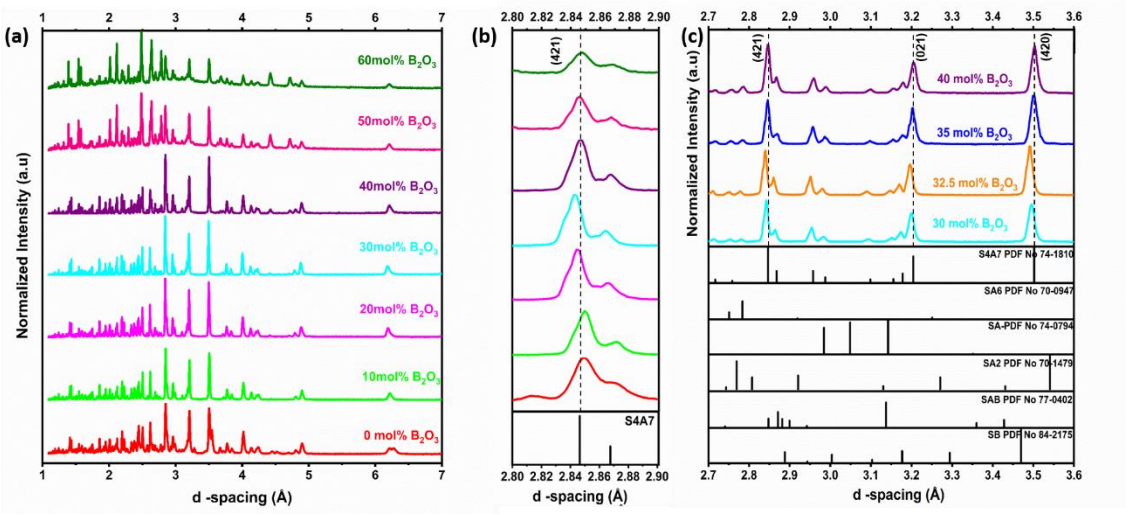

Figure 3.2 X-ray diffractograms of S4A7ED*x*B ($0 \leq x \leq 60$ mol% B_2O_3) a) full range; b) magnified around the (421) diffraction peak; c) diffractograms for S4A7ED*x*B ($30 \leq x \leq 40$ mol% B_2O_3).

Table 3.1 Percent crystallinity and amorphous phase fraction determined from the XRD data of S4A7ED*x*B ($0 \leq x \leq 60$ mol% B_2O_3) samples.

B_2O_3 Content (mol %)	**Fraction of crystalline phase (%)**	**Fraction of amorphous phase (%)**
0	83.3	16.7
10	68.79	31.21
20	65.31	34.69
30	62.58	37.42
32.5	57.52	42.48
35	58.73	41.27
40	49.71	50.29
50	38.86	61.14
60	31.92	68.08

The presence of an amorphous phase was revealed by quantifying the relative amount of crystalline phase in Figure 3.3 (a) (Table 3.1). The results of Rietveld quantitative phase analysis is summarized in Figure 3.3 (b) (Figure 3.4), of the XRD patterns of S4A7ED*x*B samples ($0 \leq x \leq 60$ mol% B_2O_3), while Table 3.2 summarizes the results of quantitative analysis of XRD data.

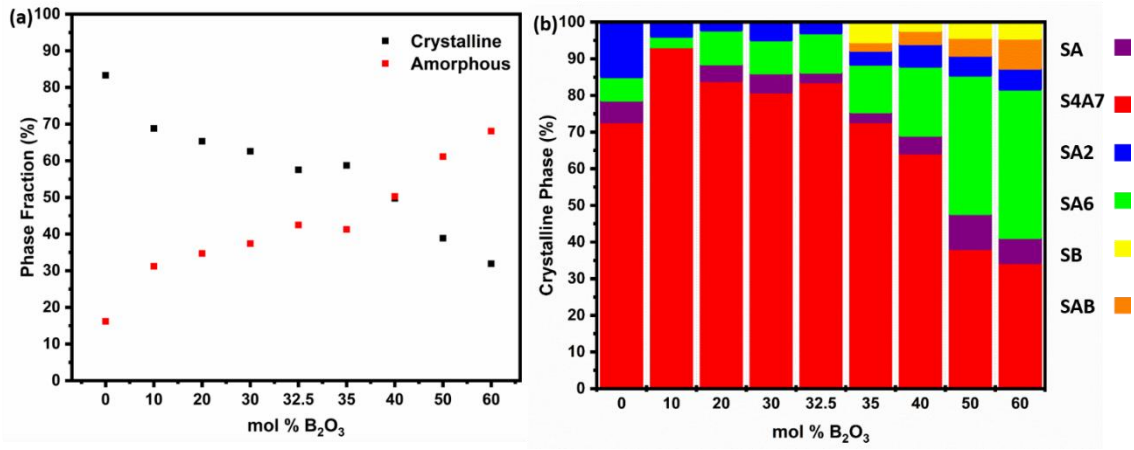

Figure 3.3 a) Percent crystallinity and amorphous phase fraction determined from the XRD data of S4A7ED*x*B ($0 \leq x \leq 60$ mol% B_2O_3) samples; b) Phase distribution revealed by Rietveld phase analysis of the diffractograms shown in Figure 3.2.

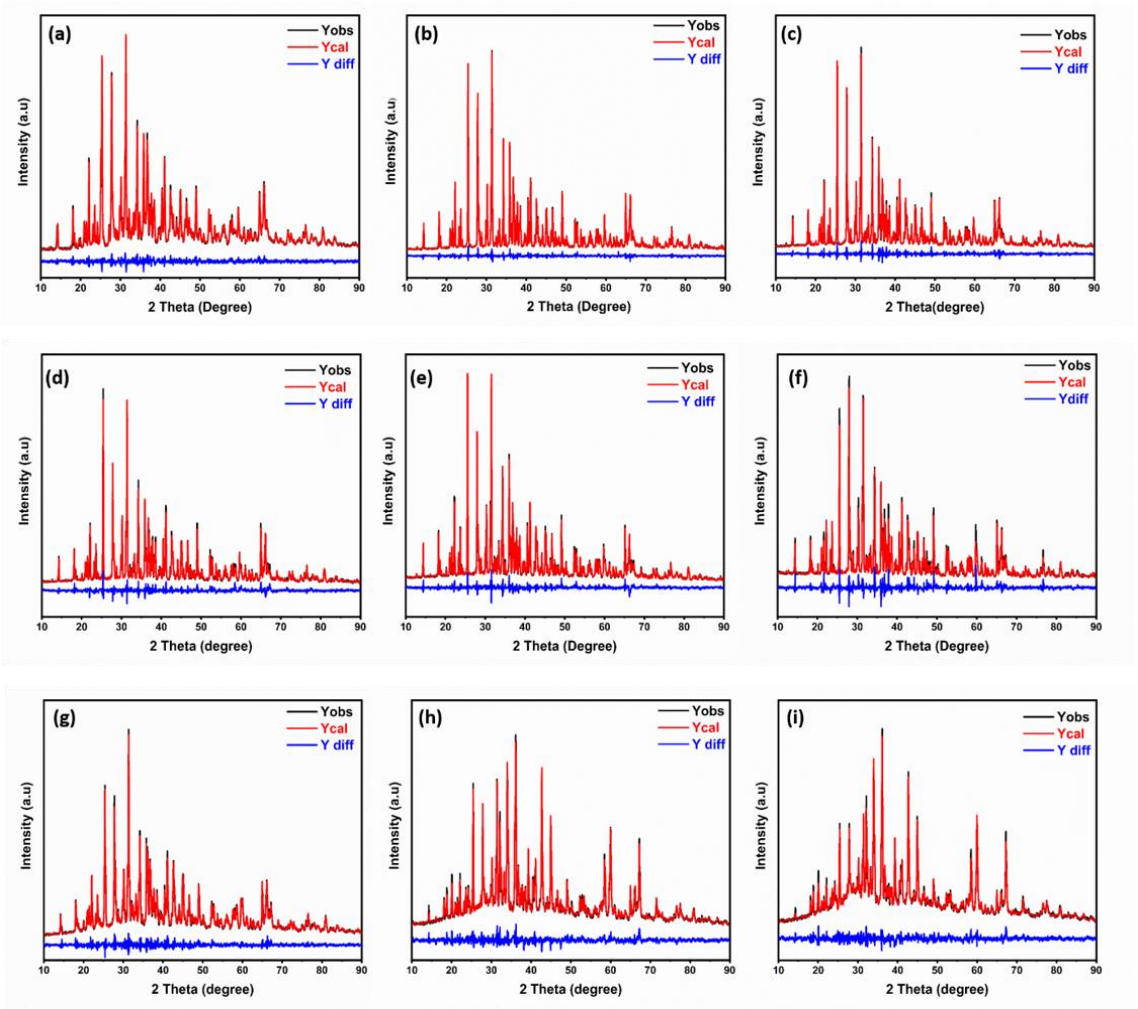

Figure 3.4 Rietveld refinement from the X-ray powder diffraction data plots of a) S4A7ED 0 mol% B_2O_3; b) S4A7ED 10 mol% B_2O_3; c) S4A7ED 20 mol% B_2O_3; d) S4A7ED 30 mol% B_2O_3; e) S4A7ED 32.5 mol% B_2O_3; f) S4A7ED 35 mol% B_2O_3; g) S4A7ED 40 mol% B_2O_3; h) S4A7ED 50 mol% B_2O_3; i) S4A7ED 60 mol% B_2O_3. Observed (black solid line); calculated (red solid line) and difference (blue solid line) patterns data taken at room temperature.

Table 3.2 Phase Composition Revealed by Rietveld Analysis of the XRD Data from the S4A7ED*x*B ($0 \leq x \leq 60$ mol% B_2O_3) samples.

B_2O_3 Content (mol %)	**Fraction of Crystalline phase (%)**					
	S4A7	**SA**	**SA6**	**SA2**	**SAB**	**SB**
0	72.86	5.9	6.38	14.85		
10	93.31		2.89	3.8		
20	84.11	4.54	9.29	2.06		
30	81.02	5.15	9.09	4.74		
32.5	83.77	2.68	10.66	2.9		
35	72.89	2.76	12.87	3.86	2.31	5.3
40	64.32	4.85	18.85	6.13	3.67	2.18
50	38.29	9.55	37.77	5.35	4.89	4.15
60	34.45	6.82	40.48	5.7	8.18	4.37

The sample prepared without B_2O_3 was 80% crystalline and was multi-phase, being dominated by the S4A7 phase (72.8%), along with SA2 (14.85%), SA6 (6.38%) and SA (5.9%) as the minor strontium aluminate phases. The maximum amount of phases exhibiting room temperature persistent luminescence, S4A7 and SA, was found in the 10 mol% B_2O_3 compound, which was of 93.3% S4A7 phase (and negligible SA content).

Table 3.3 Crystallographic Parameters Obtained from XRD Rietveld Refinements for S4A7ED *x* mol% B_2O_3 ($0 \leq x \leq 60\%$)

B_2O_3 Content	**Crystallographic Parameter**							**Reliability Factors**		**Goodness of Fit**
(mol %)	**a(Å)**	**b(Å)**	**c(Å)**	**V(Å^3)**	**α (˚)**	**β (˚)**	**γ (˚)**	**Rp (%)**	**Rwp (%)**	**(Rwp/Rexp)**
Ref	24.785	8.487	4.886	1027.772	90	90	90			
0	24.789635	8.482859	4.889069	1028.108	90	90	90	3.18869803	4.07144499	1.73
10	24.773608	8.481705	4.88466	1026.377	90	90	90	3.24668546	4.3865856	1.85
20	24.772149	8.482794	4.885342	1026.591	90	90	90	4.20389875	5.37200161	2.23
30	24.775624	8.482993	4.88515	1026.713	90	90	90	5.34348677	6.775716	2.77
32.5	24.766645	8.480208	4.884087	1025.787	90	90	90	4.36019649	5.61149564	2.26
35	24.768747	8.481266	4.885121	1025.901	90	90	90	5.74639941	7.54287943	3.22
40	24.765642	8.478007	4.882548	1025.156	90	90	90	3.97649215	5.18788495	2.16
50	24.772529	8.482357	4.884941	1026.47	90	90	90	4.13802431	5.42468832	2.26
60	24.785065	8.483662	4.886702	1027.518	90	90	90	4.02013631	5.16775404	2.17
C.S.	O.Rhmbic									
Space group	Pmma									

S4A7ED*x*B for x = 30 mol% B consisted of 81.02 % S4A7, 5.15 % SA, 9.09 % SA6 and 4.74 % SA2 phases. A similar result was obtained for the compound prepared with 32.5 mol% B_2O_3. Increasing the B_2O_3 content to 35 mol% led to a significant drop in the S4A7 content, which decreased further with increasing B_2O_3 content, whereas the amount of SA6 phase increased. The diffractogram of S4A7ED*x*B for x = 40 mol% B showed additional peaks, indicating that the presence of SrB_2O_4 (SB) and $Sr_2B_2Al_2O_8$ (SAB) phases along with S4A7, SA6, SA2 and SA phases. Further addition of B_2O_3 resulted in dominance of SA6 over all other crystalline strontium aluminate phases. When S4A7ED*x*B was processed with 60 mol% B_2O_3, the amorphous content reached 68%. In the remaining crystalline material, SA6 dominated the multi-phase distribution, along with substantial amounts of SB and SAB phases.

The FTIR spectra were analyzed to identify the structural changes in strontium aluminate compounds arising from the different amounts of B_2O_3. The FTIR spectra of S4A7ED*x*B, where $0 \leq x \leq 60$ mol% B_2O_3, are shown for the region between 500-4000 cm^{-1} in Figure 3.5 (a). No peak was detected above 1500 cm^{-1}. The region 500-1000 cm^{-1} showed vibrations related to the alumina scaffold of the S4A7 crystal structure in Figure 3.5 (b). In this region, the characteristic vibrations of O-Al-O were observed in the phase-pure, undoped S4A7 reference spectra (Figure 3.6 (a)). Absorption bands were observed for Al-O features, both anti-symmetric stretching (700-1000 cm^{-1} region) and anti-symmetric bending (550-650 cm^{-1}). When the B_2O_3 content exceeded 40 mol%, the intensity decreased for some vibrations in the 800-900 cm^{-1} range; meanwhile the increase in the shoulder indicating enhanced absorption around 710 cm^{-1} suggested bending vibrations of B-O-B linkages in the borate network.

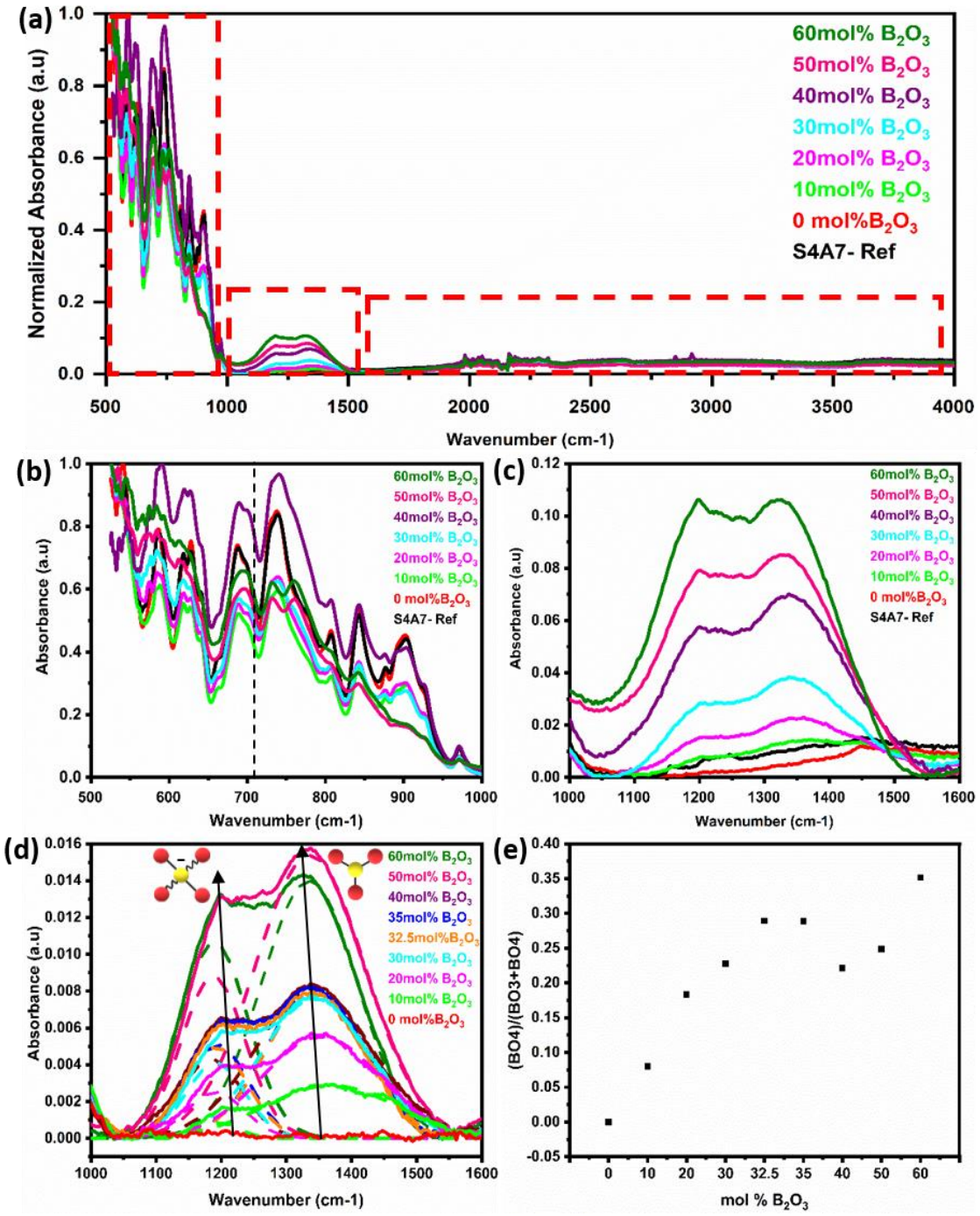

Figure 3.5 FTIR spectra summary for S4A7ED*x*B ($0 \leq x \leq 60$ mol% B_2O_3) a) full range spectra; b) 500-1000 cm^{-1} magnified; c) 1000-1600 cm^{-1} magnified; d) Deconvolution of 1000-1600 cm^{-1} magnified region; e) N_4 vs. mol% B_2O_3, where $N_4 = (B_4/(B_3+B_4))$.

No absorption peak was detected in the 1000-1600 cm^{-1} range for the reference (undoped) and the x = 0 mol% B_2O_3 compounds. With the addition of B_2O_3, two distinct absorption profiles were observed—between 1180-1200 cm^{-1} and 1330- 1370 cm^{-1}, as shown in Figure 3.5 (c). These two isolated bands became apparent when deconvoluted by assuming Gaussian profiles (Figure 3.5 (d)). The absorption band at 1180-1200 cm^{-1} corresponded to asymmetric B–O stretching vibrations of BO_4 units and the absorption at 1330-1370 cm^{-1} was assigned to B–O stretching vibrations of BO_3 groups [13,50,51]. Using the integrated area beneath these 2 vibration peaks, we determined the relative change in $N_4 = (B_4/ (B_3+B_4))$ as a function of B_2O_3 content (Figure 3.5 (e)).

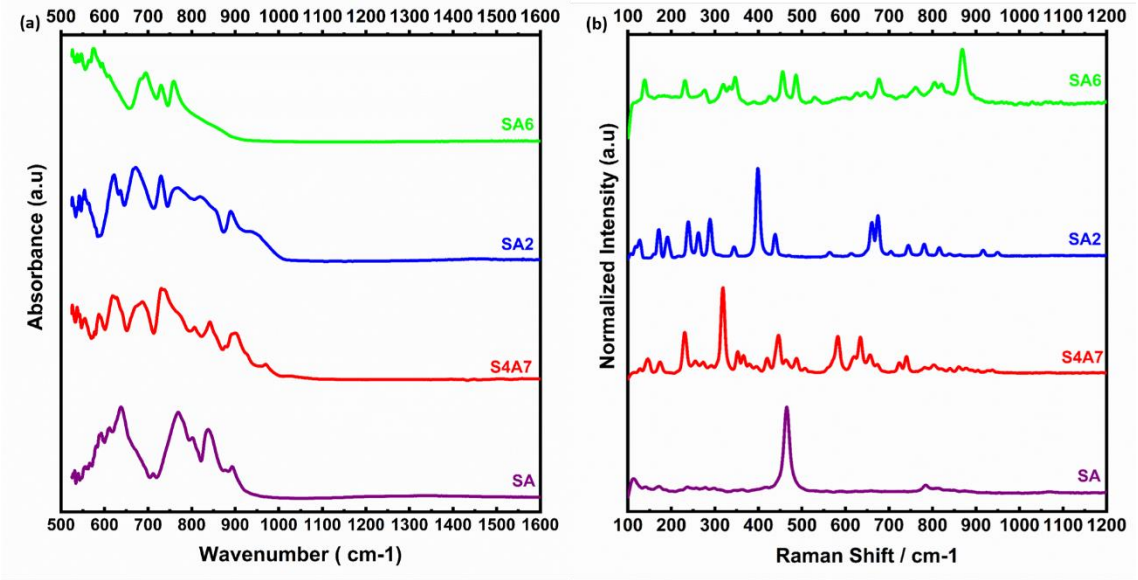

Figure 3.6 Reference Spectrum for SrO-Al_2O_3 a) FTIR ; b) Raman Spectrum

The intensity of these bands increased in a linear manner with B_2O_3 content, until reaching 30 mol% B_2O_3. Across the range 30 ≤ x ≤ 40 mol% B_2O_3, the N4 ratio reached a maximum value in the 32.5-35 mol% B_2O_3 compounds, and then declined in the 40 mol% B_2O_3 one. When the B_2O_3 content exceeded 50 mol% B_2O_3, we observed a sharp increase in peak intensities, concurrent with the amorphous content.

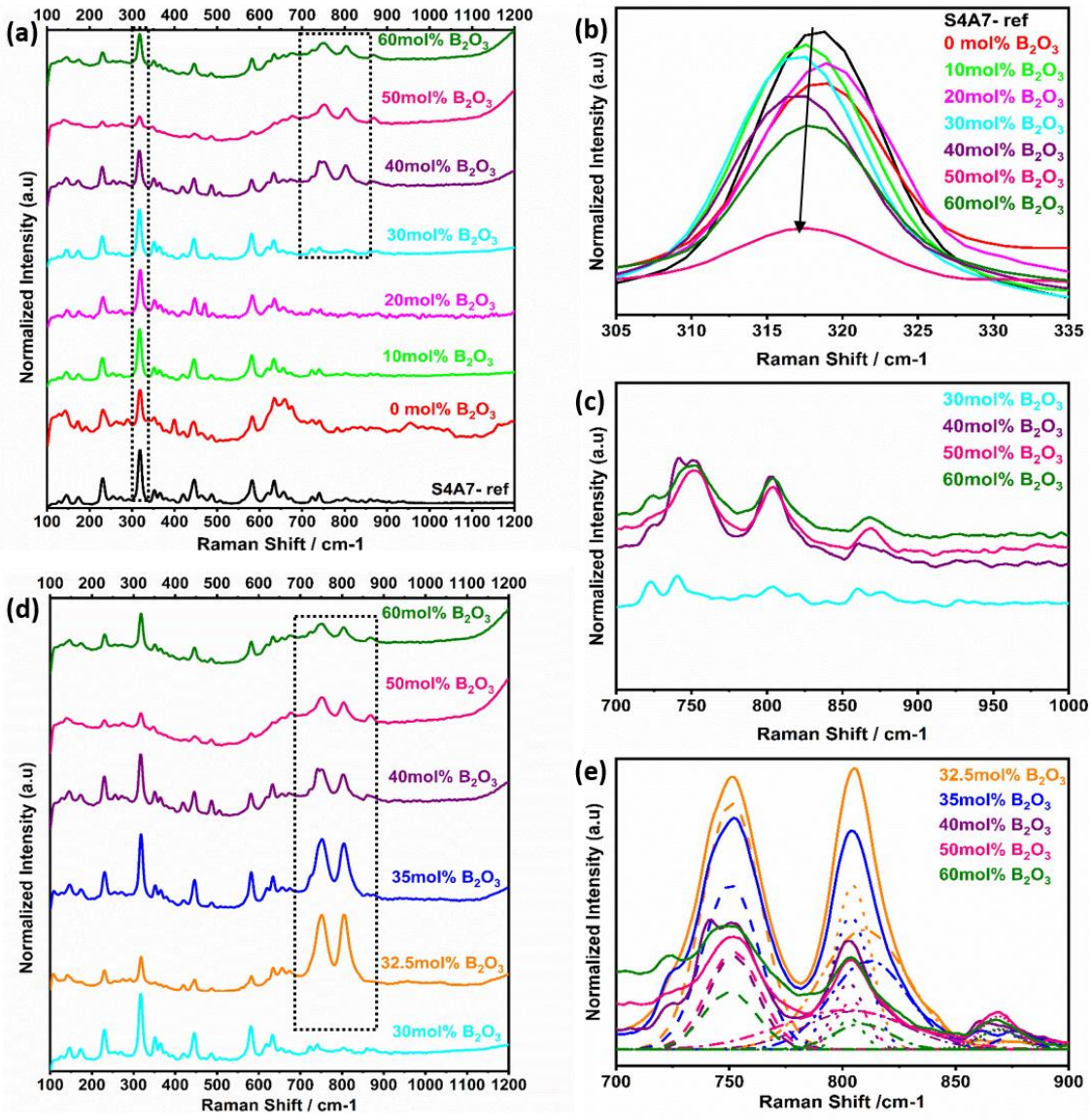

Figure 3.7 a) Raman shift spectra for S4A7ED*x*B ($0 \leq x \leq 60$ mol% B_2O_3); b) relative peak shift *ca.* 318 cm^{-1}; c) overlap region for 700-1000 cm^{-1}; d) S4A7ED*x*B ($30 \leq x \leq 60$ mol% B_2O_3); e) deconvoluted Raman shift spectra for S4A7ED*x*B ($30 \leq x \leq 60$ mol% B_2O_3)**.**

The changes in the vibrational modes of crystalline S4A7 caused by the incorporation of B_2O_3 into the crystal structure were also investigated by using Raman spectroscopy analysis. The phase-pure, orthorhombic S4A7 compound was characterized to serve as a reference fingerprint (Figure 3.6 (b)). The Raman spectra of S4A7ED*x*B, where $0 \leq x \leq 60$ mol% B_2O_3, are summarized in Figure 3.7 (a). With increasing B_2O_3, we observed a

weakening in intensity of the main 318 cm^{-1} peak, accompanying a shift toward shorter wavelengths (Figure 3.7 (b)). Furthermore, the appearance of additional peaks in the range of 700-900 cm^{-1} was observed in S4A7ED*x*B ($30 \leq x \leq 60$ mol% B_2O_3), which largely accounted for the boron-related structural groups (Figure 3.7 (c)). Figure 3.7 (d) shows the evolution in Raman shift within 700-900 cm^{-1} in for the S4A7ED*x*B compounds with $30 \leq x \leq 60$ mol % B_2O_3, correlated with the deconvolution analysis of these peaks in Figure 3.7 (e).

The $BØ_3$ unit has a D_{3h} symmetry point group symmetry and has $\Gamma_{D3h} = A'_1(R) + 2E'(IR,R) + A''_2(IR)$, in which R and IR represents Raman and infrared activity. These vibration modes are symmetric stretching ν_1 (A'_1), out-of-plane bending ν_2 (A''_2), asymmetric stretching ν_3 (E'), and in-plane bending ν_4 (E') modes. The replacement of bridging oxygen (Ø) by a non-bridging one (O^-) reduces to symmetry to C_{2V} from D_{3h}, while the doubly degenerate (E') asymmetric stretching mode will split into two IR-active components of A_1 and B_2 symmetry [52–55].

The strongest peak developing at 808 cm^{-1} was assigned to the symmetric breathing vibration of $BØ_3$ boroxyl rings, reflecting the presence of vitreous B_2O_3 compounds (Figure 3.8 (a)) [7,50]. The second strongest peak at 750 cm^{-1} was assigned to the symmetric breathing vibration of 6-membered rings, containing one $BØ_3$ triangle replaced by one $BØ_4$ tetrahedron (Figure 3.8 (b)) [44,50]. The band at 803 cm^{-1} was assigned to metaborate $BØ_2O^-$ units (Figure 3.8 (c)). Additional evidence of metaborate formation was provided by the weaker bands at around 640 cm^{-1} symmetric stretch of B-O-B rings [43,56]. With elevated B_2O_3 content, the formation of orthoborate monomers at 868 cm^{-1} was observed, reflecting the depolymerization of boroxyl rings and rings with BO_4 tetrahedral units to orthoborate monomers (Figure 3.8 (d)) [10,13]. Both Raman and IR spectroscopic techniques were applied in a complementary way to reveal the formation and changes of complex boron units.

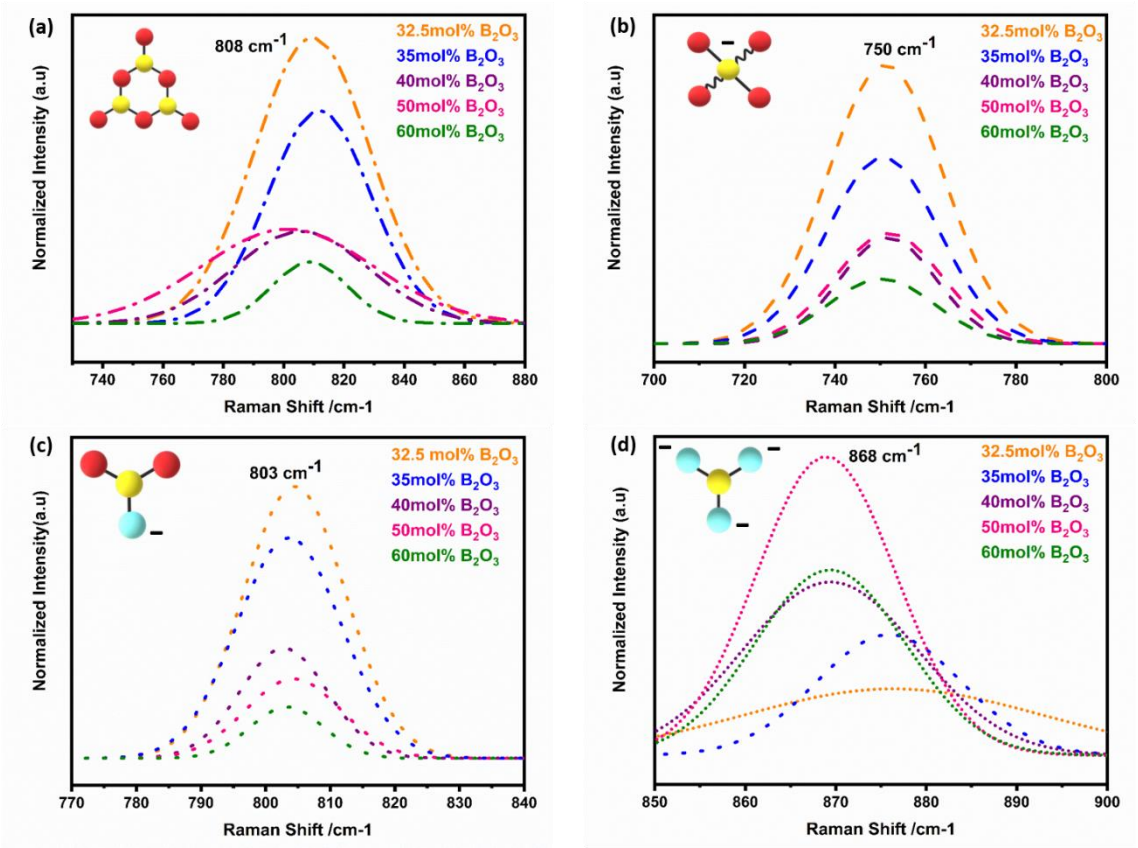

Figure 3.8 Deconvoluted Raman-shift spectra for S4A7ED*x*B ($30 \leq x \leq 60$ mol% B_2O_3) for vibrations of a) boroxyl rings of corner-sharing [$B\emptyset_3$]; b) [$B\emptyset_4$]$^-$; c) metaborate [$B\emptyset_2O$]$^-$; d) orthoborate (monomers of $[BO_3]^{3-}$).

Raman mapping was performed on sintered polished pellets of S4A7ED*x*B compounds of x = 30 mol% B_2O_3 and 40 mol% B_2O_3. To analyze the hyperspectral Raman dataset, we applied a multivariate curve resolution-alternating least squares (MCR-ALS) method. The spectral data matrix was analyzed in the Wire 3.4 environment using the MCR-ALS module, in which the data matrix was decomposed into spectral profiles ("Loadings") and concentration profiles ("Scores").

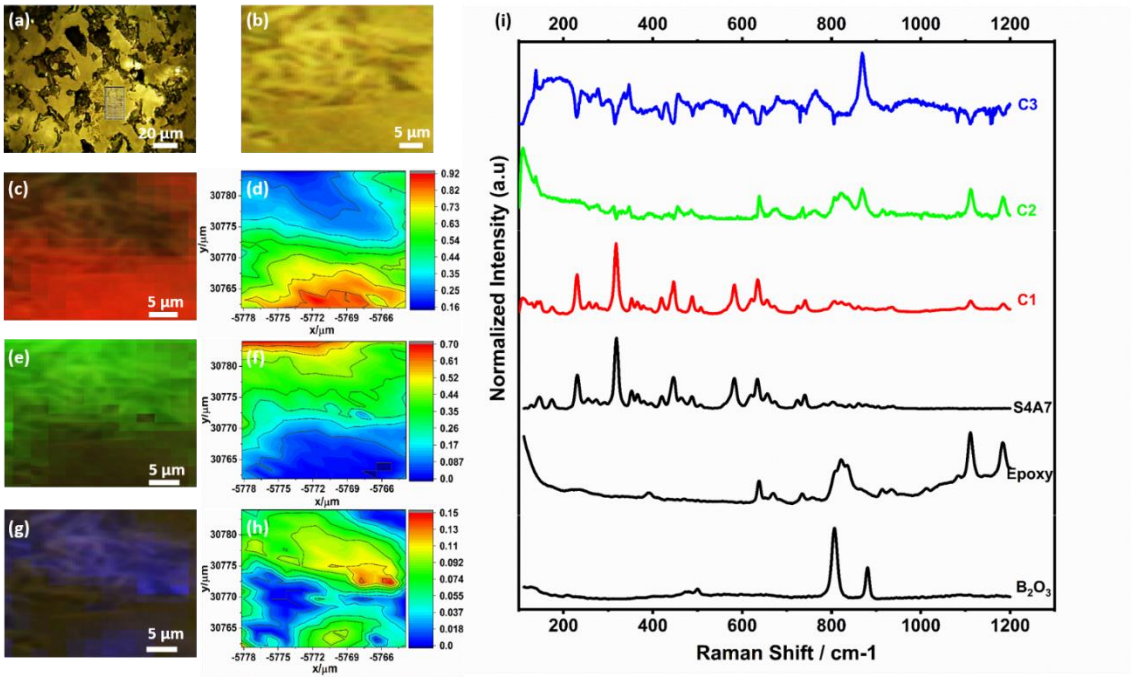

Figure 3.9 MCR-ALS analysis of Raman shift hyperspectral maps of S4A7ED 30 mol% B_2O_3 a) visible light image of specimen; b) region of interest for Raman mapping; c) C1 spectral image; d) C1 color coded score image; e) C2 spectral image; f) C2 color coded score image; g) C3 spectral image; h) C3 color coded score image; i) Corresponding Raman spectra of the 3 components compared to reference Raman spectra from pure S4A7, B_2O_3 precursor and the epoxy.

In the x = 30 mol% B_2O_3 data set, three physically significant MCR-ALS components were observed; and a good correlation was obtained between the identified loadings of the reference spectra from pure S4A7, B_2O_3 powder, and epoxy. Figure 3.9 (a) shows the visible-light image of the region of interest for Raman spectral imaging for the x = 30 mol% B_2O_3 S4A7EDxB specimen. Figure 3.9 (b) shows the scan area at higher magnification. The hyperspectral image of the first component is shown in Figure 3.9 (c), which is related to the S4A7 grains. Both overlay and color-coded (Figure 3.9 (d)) images show the spatial distribution of S4A7 grains. The representative Raman spectrum from component 2, shown in green, is consistent with the reference Raman spectrum obtained from neat epoxy (Figure 3.9 (e)). Since the pellet was necessarily embedded in an epoxy mold for polishing, the observation of epoxy at the surface was not surprising. (Figure 3.9 (f)). The last component appearing was attributed to the B_2O_3, which is shown in blue

(Figure 3.9 (g)). Color-coded images formed by boron units revealed the distribution of boron units around the S4A7 grains (Figure 3.9 (h)). In Figure 3.9 (i) corresponding Raman spectra of the 3 components compared to reference Raman spectra from pure S4A7, B_2O_3 and the epoxy has shown.

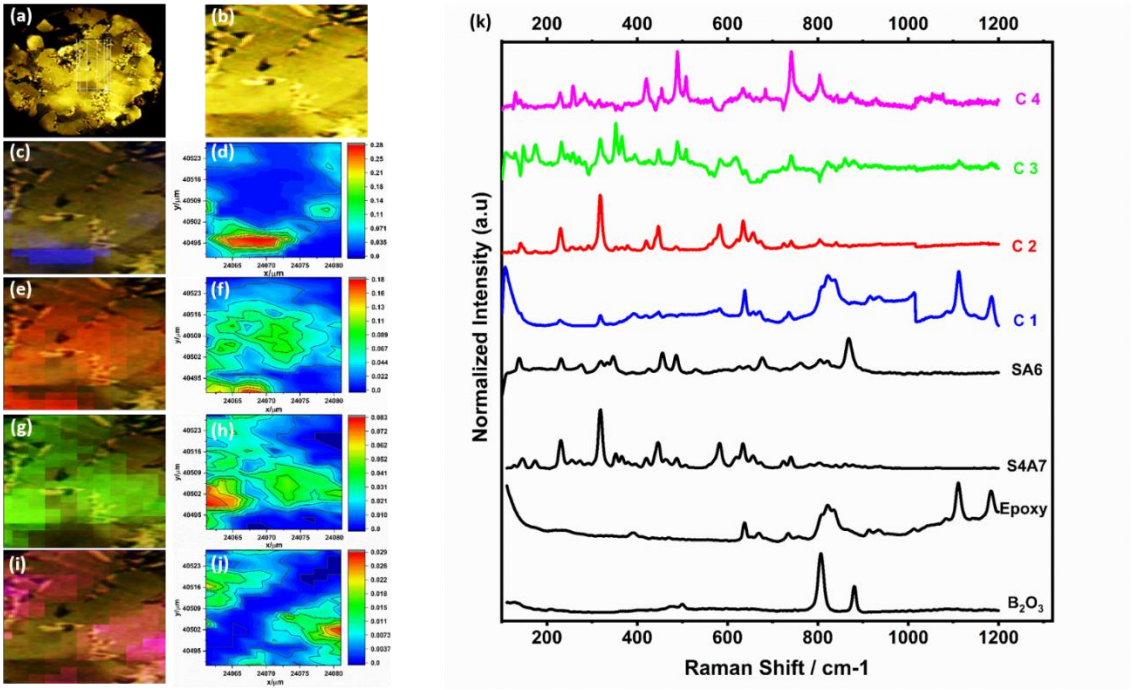

Figure 3.10 MCR-ALS analysis of Raman shift hyperspectral maps of S4A7ED 40 mol% B_2O_3 a) visible light image of specimen; b) region of interest for Raman mapping; c) C1 spectral image; d) C1 color coded score image; e) C2 spectral image; f) C2 color coded score image; g) C3 spectral image; h) C3 color coded score image; i) C4 spectral image; j) C3 color coded score image representative; k) Corresponding Raman spectra of the 4 components compared to reference Raman spectra from pure S4A7, SA6, B_2O_3 precursor and the epoxy.

MCR-ALS analysis of Raman shift hyperspectral maps of x = 40 mol% B_2O_3 S4A7EDxB are shown in Figure 3.10. There were four components, which were consistent with the reference spectra collected from phase pure S4A7, SA6, B_2O_3 powder, and the epoxy. The distribution of complex phases was color-coded in the MCR score—*i.e.*, concentration profile—plot shown. The multi-phase region was selected for mapping to analyze the distribution of crystalline and amorphous components. (Figure 3.10 (a-b)).

The first component originated from the epoxy, as was observed in the pellet of x =30 mol% B_2O_3 (Figure 3.10 (c-d)). The hyperspectral image that was color-coded red had correlated to large S4A7 grains (Figure 3.10 (e-f)). The presence of small SA6 grains in the scan area resulted from the third component, which was colored green (Figure 3.10 (g-h)) and was consistent with the reference spectrum of SA6. Component 4 reflected the presence of polyborate units and their spectral distributions across the mapped region (Figure 3.10 (i-j)). This component appeared to be superposed with the characteristic vibrations of S4A7, which is due to the borate-rich glassy phase being adjacent to S4A7 grains. In Figure 3.10 (k) representative Raman spectra of the 4 components compared to reference Raman spectra from B_2O_3, epoxy, pure S4A7, and pure SA6 has shown.

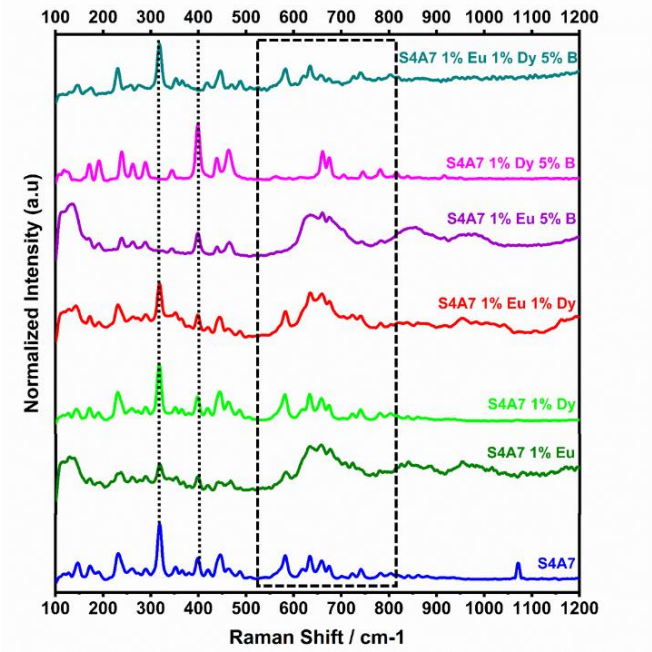

Figure 3.11 Raman shift of S4A7 unit cell doped with only Eu, Dy and B**.**

Figure 3.11 shows the effect of individual rare earth dopants on the S4A7 unit cell. The S4A7 unit cell doped with only Eu exhibited distortion in the Raman shift spectrum especially in the region 550-850 cm^{-1}, while doping with only Dy didn't generate such a distortion. This observation can be attributed to the difference in size between Eu and Dy ions, the latter of which, being larger, is more prone to segregating out of the grain above the solubility limit [4]; as a result, S4A7 doped only with Dy exhibited similar Raman

spectra with the non-doped sample. The compound co-doped with Eu and Dy showed spectra with high intensity and narrow bands consistent with S4A7 doped only with Eu.

It should be noted that in S4A7 containing 1 at% Eu 5 mol% B_2O_3 and S4A7 1 at% Dy and 5 mol% B_2O_3, neither compound exhibited the vibration modes of S4A7. The Raman shift spectrum of S4A7 1 at% Eu and 5 mol% B_2O_3 had wider and weaker Raman bands and was missing the shift at 318 cm^{-1}. Meanwhile, the spectrum of S4A7 1 at% Dy and 5 mol% B_2O_3 had Raman bands similar to those of SA2. The changes induced in the Raman spectra suggest that the presence of boron affects the atomic arrangements in each compound differently, which may also differentiate their incorporation into Sr sub-lattice sites in the unit cell.

Finally, the Raman spectra of S4A7ED*x*B with x = 5 mol% B_2O_3 contained known vibrational modes that were observed in other S4A7ED*x*B compounds, the ones containing S4A7 as a major phase.

3.3 Discussion

The optimal B_2O_3 composition for Pechini-processed S4A7ED*x*B compound was determined to lie in the range 30 mol% $B_2O_3 \leq x \leq 40$ mol% B_2O_3. De-trapping from both shallow-trap and deep-trap states, as extrapolated from the afterglow decay curves, was of the longest duration within this range of boron content and correlated to persistent luminescence of the longest duration. The introduction of B_2O_3 into the S4A7 unit cell appears to be associated with increasing the depth of both types of trap centers, leading to a slower decay rate than that observed in other B_2O_3-doped compositions.

The variation in strontium aluminate phase distribution was observed with the addition of boron oxide in samples prepared with identical synthesis and heat treatment conditions (Figure 3.3 (b)). We focused our analysis on the atomic positions in the target persistent luminescence phase, S4A7ED*x*B, where $0 \leq x \leq 60$ mol% B_2O_3, by performing Rietveld structural refinement analysis on the XRD data. As shown in Figure 3.12, the refined unit-

cell parameters revealed the most significant shrinkage in the S4A7 crystal lattice dimensions (*a*, *b*, *c*, and volume) starting from 30 mol % B_2O_3 and extending to 40 mol % B_2O_3 (Table 3.3). These parameters were compared against those of the pure S4A7 reference. The reason for this apparent change in the unit cell parameters appear to be induced by the presence of borate structures in the lattice.

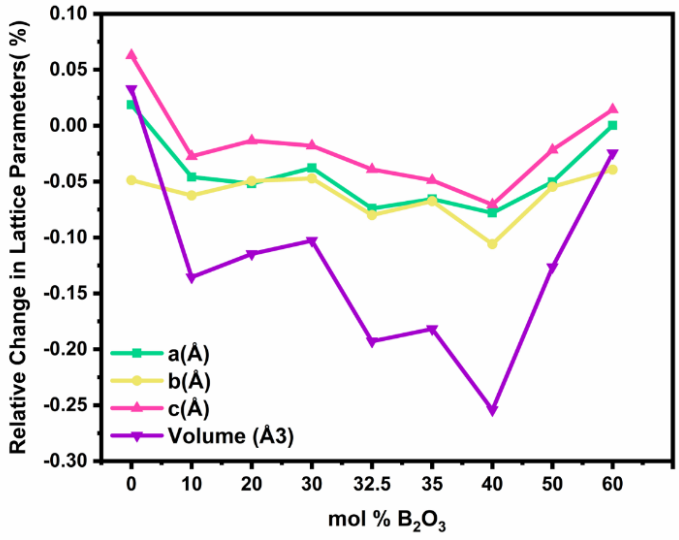

Figure 3.12 Changes in unit cell dimensions of S4A7 with increasing B_2O_3 content during Pechini processing.

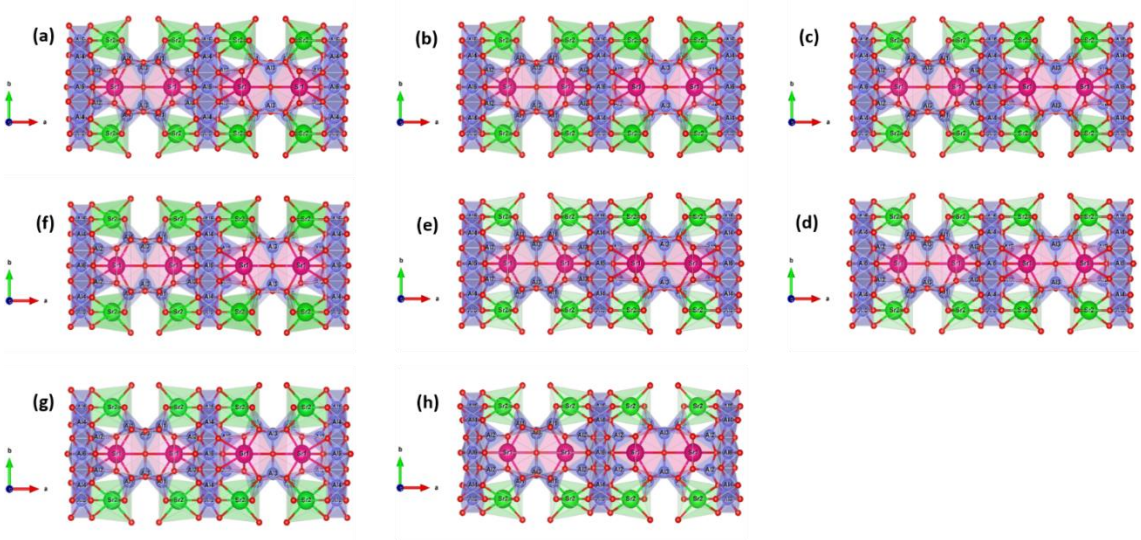

Figure 3.13 Visualization of the S4A7 unit cell, determined from *.cif file for the B_2O_3-free S4A7 unit cell and from structure files derived from Rietveld refinement analysis of XRD diffractograms shown in Figure 4. a) Original cif file; b) S4A7ED 0 mol% B_2O_3; c) S4A7ED 10 mol% B_2O_3; d) S4A7ED 20 mol% B_2O_3; e) S4A7ED 30 mol% B_2O_3; f) S4A7ED 40 mol% B_2O_3; g) S4A7ED 50 mol% B_2O_3; h) S4A7ED 60 mol% B_2O_3.

The effect of B_2O_3 incorporation on the crystalline S4A7 unit cell was visualized with the help of Vesta, using the atomic positions determined by Rietveld refinement analysis (Figure 3.13). The S4A7 unit cell contains 6 different crystallographically non-equivalent Al sites, and these Al sites are coordinated with 4 or 6 oxygen atoms. The Al1, Al2 and Al3 form AlO_4 tetrahedra, while Al4, Al5 and Al6 form AlO_6 octahedra. The interconnected network of these alumina polyhedra forms a rigid 3-D scaffold, with large cavities filled by Sr cations providing electrical charge balance. On the basis of above structure, there are two nonequivalent Sr sites: Sr2 coordinated by 7 oxygens (Wyckoff 4i) and Sr1 coordinated by 10 oxygens (Wyckoff 4j) (Figure 1.1).

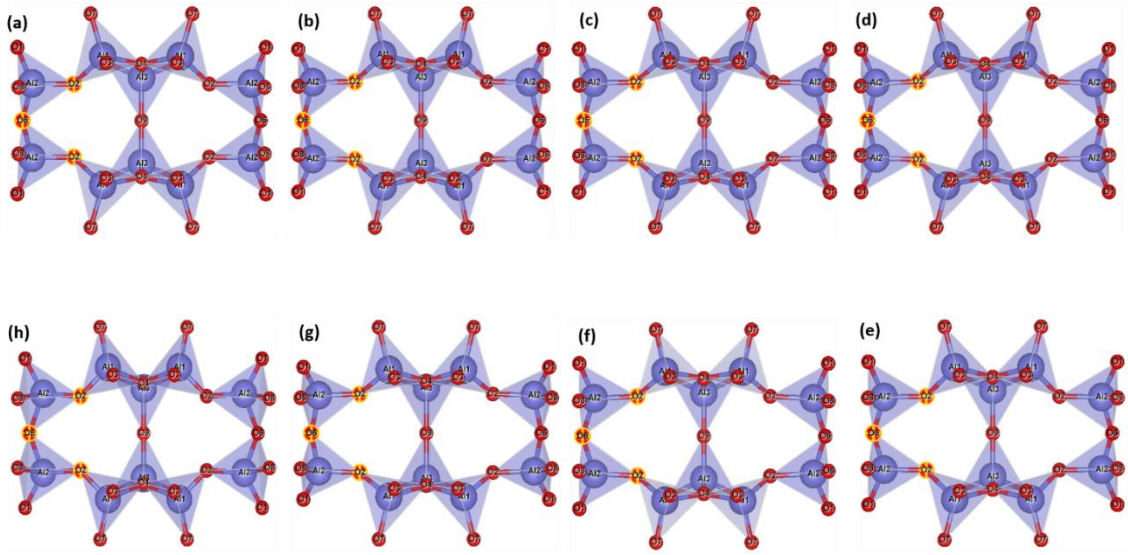

Figure 3.14 Visualization of the Al CN=4 polyhedral scaffold of the S4A7 unit cell, determined from *.cif file for the B_2O_3-free S4A7 unit cell and from structure files derived from Rietveld refinement analysis of XRD diffractograms shown in Figure 3.3. a) Original cif file; b) S4A7ED 0 mol% B_2O_3; c) S4A7ED 10 mol% B_2O_3; d) S4A7ED 20 mol% B_2O_3; e) S4A7ED 30 mol% B_2O_3; f) S4A7ED 40 mol% B_2O_3; g) S4A7ED 50 mol% B_2O_3; h) S4A7ED 60 mol% B_2O_3.

The change in polyhedral volume of each of the AlO_4 tetrahedrons is shown in Figure 3.15 (a). Within the compositional range S4A7ED*x*B *x* = 30-40 mol% B_2O_3 the volume of the sites Al2 and Al3 increased, while that of Al1 remained unchanged. (Figure 3.16) With further addition of up to 60 mol% B_2O_3, the integrity of the Al2 polyhedral volume increased by ca. 12.6%. Boron appeared not to have caused a significant change in the octahedral AlO_6 chains in the *x* = 30-40 mol% B_2O_3 range, when compared to the reference sample (Figure 3.15 (b)). The overall decrease in the AlO_6 polyhedra correlated with increasing B_2O_3 content. (Figure 3.17)

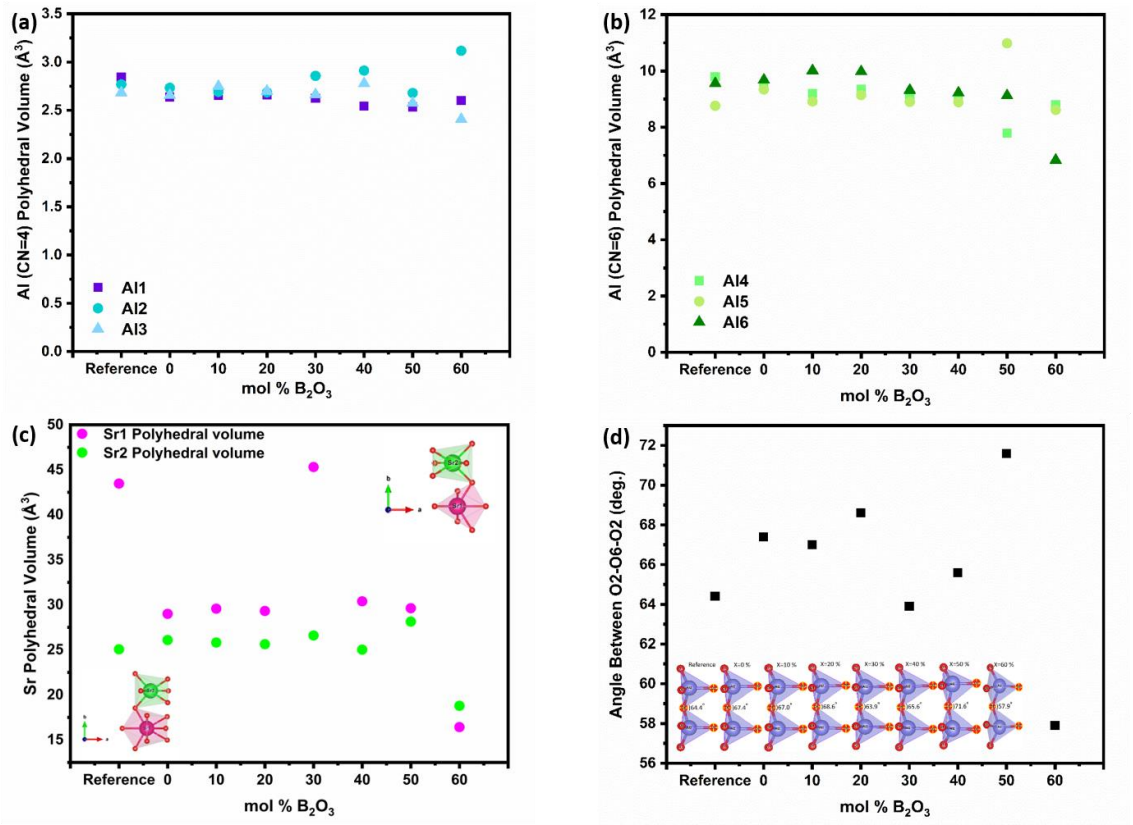

Figure 3.15 Volume changes resulting from modification by B_2O_3 addition for S4A7 reference and the representative S4A7ED*x*B ($0 \leq x \leq 60$ mol% B_2O_3) for a) Al CN=4 polyhedra; b) Al CN=6 polyhedra; c) Sr1 and Sr2 coordination polyhedra; and d) angle between oxygen sites O2-O6-O8.

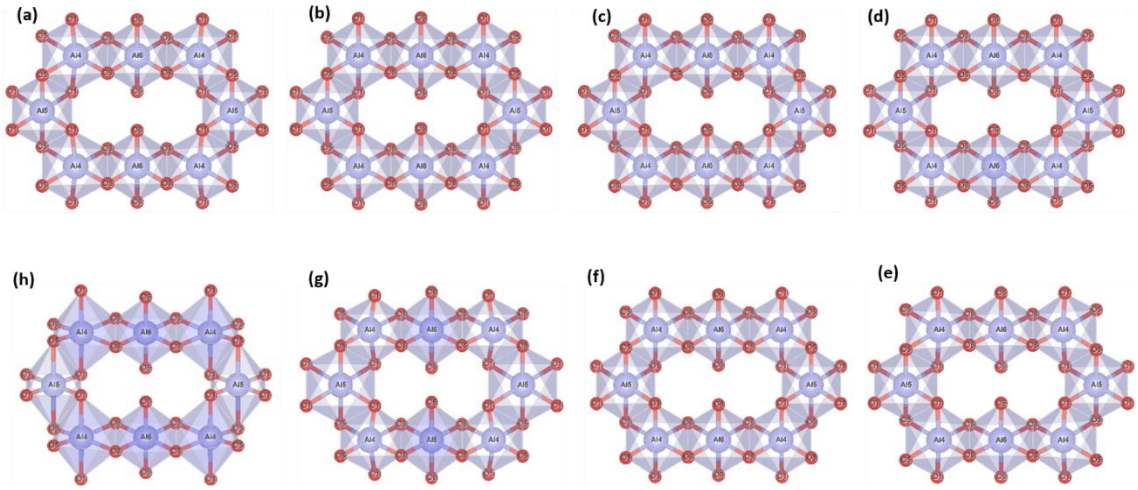

Figure 3.16 Visualization of the Al CN=6 polyhedral scaffold of the S4A7 unit cell, determined from *.cif file for the B_2O_3-free S4A7 unit cell and from structure files derived from Rietveld refinement analysis of XRD diffractograms shown in Figure 3.3. a) Original cif file; b) S4A7ED 0 mol% B_2O_3; c) S4A7ED 10 mol% B_2O_3; d) S4A7ED 20 mol% B_2O_3; e) S4A7ED 30 mol% B_2O_3; f) S4A7ED 40 mol% B_2O_3; g) S4A7ED 50 mol% B_2O_3; h) S4A7ED 60 mol% B_2O_3.

The incorporation of Eu into Sr sites was demonstrated using AR-STEM imaging [47]. The results of our analyses in this work revealed that both Sr sites investigated in compounds containing 30-40 mol% B_2O_3 showed localized expansion of their volume, particularly in the Sr1 polyhedral volume (Figure 3.15 (c) and Table 3.4). Sr1 (CN=10) has lower covalency compared to Sr2 (CN=7). This expansion would have altered the crystal field coordination environment around the Eu^{2+} ions, resulting in changes to the electronic structure of Eu^{2+} that control the persistent luminescence.

Table 3.4 Crystallographically non-equivalent Sr site evolution with increasing B_2O_3-content. (Data for the plot shown in Figure 3.15)

B_2O_3 Content (mol %)	**Sr1 Polyhedral volume ($Å^3$)**	**Sr2 Polyhedral volume ($Å^3$)**
Reference	43.4704	25.0581
0	29.0021	26.0927
10	29.5769	25.8161
20	29.3219	25.6241
30	45.3086	26.6014
40	30.3872	25.0241
50	29.6221	28.139
60	16.4174	18.7803

With Sr1 located in the large interstitial cavities of the alumina scaffold, any expansion of their polyhedral volume would deform the scaffold structure (Figure 3.15 (d)) (Table 3.5). The angle between neighboring Al2 tetrahedra within the x = 30-40 mol% B_2O_3 compositional range showed values closest to the undoped reference spectra. In addition, the expansion in Sr sites pushed the 4-coordinated alumina polyhedra towards each other. This observation may explain the decreasing d_{421}-spacing of between the main (421) planes within the compositional range of $30 \leq x \leq 40$ mol% B_2O_3.

Table 3.5 Crystallographically non-equivalent Al site evolution with increasing B_2O_3-content. (Data for the plot shown in Figure 3.15)

B_2O_3 Content (mol %)	Al CN= 4 (Å^3)			Al CN= 6 (Å^3)			Angle O2-O6-O2 (˚)
	Al1	Al2	Al3	Al4	Al5	Al6	Deg
Reference	2.8423	2.7679	2.6823	9.7875	8.759	9.5566	64.4
0	2.6382	2.7324	2.6553	9.4135	9.3414	9.679	67.4
10	2.6547	2.6907	2.7474	9.1918	8.9129	10.0118	67
20	2.6571	2.6853	2.6989	9.3434	9.142	9.9776	68.6
30	2.6227	2.8568	2.6624	9.1353	8.8955	9.3164	63.9
40	2.5426	2.9113	2.7766	9.0598	8.8862	9.2185	65.6
50	2.5347	2.6788	2.574	7.7868	10.9799	9.1209	71.6
60	2.5991	3.1166	2.4069	8.8040	8.6146	6.8316	57.9

Mid-infrared transmission and Raman spectra revealed that S4A7ED*x*B ($0 \leq x \leq 60$ mol% B_2O_3) compositions contained polyborate supramolecular arrangements, like neutral trigonal $BØ_3$ units, charged $BØ_4^-$ tetrahedra, metaborate $BØ_2O^-$, and orthoborate $(BO_3)^{3-}$. The red-shift of the 1000-1600 cm^{-1} absorption band envelope has been reported for other highly modified borate glasses [43,44]. For the compositions of S4A7ED*x*B with $10 \leq x \leq 40$ mol% B_2O_3, the progressive red-shift of the 1342-1370 cm^{-1} peak frequency was attributed to the formation of metaborate triangles $BØ_2O^-$ that were manifested by the deconvoluted Gaussian BO_3 component. Changes in the number of B-O$^-$ and B-Ø bonds undergoing stretching vibrations in $BØ_2O^-$ and $BØ_3$ units resulted in the downshift and asymmetry of these bands [44,55].

For the S4A7ED*x*B compositions of $40 \leq x \leq 60$ mol% B_2O_3, these trends continued in the 1335-1342 cm^{-1} spectral shift range, which was attributed to the progressive depolymerization in the borate network in superstructural units transforming to metaborate $(BØ_2O)^-$ and then orthoborate $(BO_3)^{3-}$ monomers. The presence of $(BO_3)^{3-}$ units was also observed, represented by peaks in the 500-1000 cm^{-1} region that appeared

only in compounds with > 40 mol% B_2O_3. The peak around 710 cm^{-1} was an out-of-plane bending mode of borate $(BO_3)^{3-}$ triangular units. In addition, the absorption bands around 800-1000 cm^{-1} had weakened, which was indicative of vibration modes dampened by the presence of B. The coexistence of multiple peaks with red-shift indicated the lowered symmetry of boron units. The absorption peak component related to BO_4 units (1189-1198 cm^{-1}) didn't show a pronounced overall red-shift compared to that of BO_3 (1335-1370 cm^{-1}).

The Raman spectra had also showed the characteristic vibrations of boron units, but offered deeper insight into the polyborate suprastructures. When S4A7ED*x*B contained 30-40 mol% B_2O_3, the simultaneous occurrence of bands around 808 cm^{-1}, 750 cm^{-1}, and 803 cm^{-1} in the Raman spectra suggested the presence of polymeric polyborate groups in the orthorhombic S4A7 crystal structure. Deconvolution analysis of the 700-900 cm^{-1} band revealed not only the presence of planar $BØ_3$ rings (808 cm^{-1} band), but also the symmetric breathing vibration of six-membered ring one replaced by $BØ_4^-$ (750 cm^{-1} band). The presence of such rings suggests an interconnected network of borate units in the 32.5 mol% B_2O_3 and 35 mol% B_2O_3 compounds. These spectral changes are consistent with the transformation of $BØ_3$ units into $BØ_4^-$ tetrahedra, as revealed by FTIR spectra (Figure 3.5 (d-e)). The maximum N4 value was attained by processing S4A7ED*x*B with 32.5-35 mol% B_2O_3 and indicated conversion of boroxyl rings to $BØ_4^-$ tetrahedra groups in compounds of this composition range.

Furthermore, the co-existence of metaborate suprastructural units—resonance at 803 cm^{-1} and 640 cm^{-1}—with $BØ_4^-$ ones, suggest an equilibrium between isomeric trigonal $2BØ_2O^-$ and charged tetrahedral units within the S4A7ED*x*B ($30 \leq x \leq 40$ mol% B_2O_3):

$$2(BØ_4)^- \leftrightarrow 2BØ_2O^-$$

Eq (3.2)

As the B_2O_3 concentration was increased, the borate backbone became further de-polymerized. The number of the non-bridging oxygen ions increased with the formation of orthoborate units, as revealed by the Raman response at 868 cm^{-1}. De-polymerization

resulted in the break-up of the B-O-B linkages and increase in free volume within the scaffold of coordination polyhedra.

In S4A7ED*x*B compounds of > 40 mol% B_2O_3, the intensity decreased for the bands at 808 cm^{-1}, 803 cm^{-1} and 750 cm^{-1}, while that of 868 cm^{-1} (ortho) increased. Such a spectral evolution indicates that the number of bridging oxygen per boron decreased, resulting in a dampening and red-shift in the vibration of B-Ø bonds in the $BØ_3$, $BØ_2O^-$, and $BØ_4^-$ units. The frequency of the B-O^- stretching in orthoborate triangles BO_3^{3-} was observed to increase with an increase in non-bridging oxygen content. Meanwhile, the lower intensity and red-shift of the main vibration at 318 cm^{-1} and the distortion in phonon vibrations in the Raman spectra indicated that the covalent nature of Al-O bonding was affected by the increase in non-bridging oxygen.

In compositions with B_2O_3 content in excess of that with the longest persistent luminescence duration (30-40 mol% B_2O_3), the electron density of the boron ions had increased as a consequence of de-polymerization of the boroxyl network, which increased the non-bridging oxygen content. As a consequence, the change in the proportion of different borate units perturbed localized electrical charge distribution within the crystal unit cell, which would in turn modify luminescence duration. Because the compounds of optimal luminescence contained connected planar triangular units and tetrahedral units, along with metaborate units, these results suggest that the formation of polymerized borate groups from BO_3 triangles and BO_4 tetrahedra contribute to the persistence behavior by stabilizing the Eu^{2+} and Dy^{3+} in the S4A7 unit cell. The coordination environment around the Eu and Dy ions, *i.e.* the crystal field around them, was affected by changes in the polyborate supramolecular structures. After all, the B-O network is known to act as an electron trapping center, which may serve as additional trap centers[57].

The fraction and arrangement of polyborate groups depends not only on the concentration of B incorporated into the crystal structure but also the type of modifier cation, which will affect the structure and optical properties of the overall network. The dual role of Sr as a network modifier and electrical charge compensator was a function of the SrO:Al_2O_3 ratio [58]. There was competition between Al and B as network formers for bonding with the

oxygen ions, which also contributed different numbers of bridging oxygen. When there was coexistence of aluminum and boron oxides, the resulting glass was characterized predominantly by formation of AlO_4 tetrahedra [12]. In a low glass and crystalline system rich in Al^{3+} modifier, AlO_6 formed for charge compensation [11].

The amount of B_2O_3 used determined the way B interacts with the ions in the amorphous pre-ceramic, and consequently the evolution in crystal structure. Evaluation of the crystal structure of S4A7 revealed that boron incorporation had altered the lattice parameters, to a degree correlated to the amount of B_2O_3 used during synthesis. The integrity of the unit cell was maintained within the S4A7ED*x*B composition optimal for extreme persistent luminescence—$30 \leq x \leq 40\%$ mol B_2O_3—although some cation coordination polyhedra underwent deformation, particularly the Sr1 polyhedra and the AlO_4 tetrahedra: Al1, Al2, and Al3.

For $30 \leq x \leq 40$ mol% B_2O_3, there was increased free volume around Sr^{2+} and $B\text{Ø}_2O^-$ structures present in the crystal structure, suggesting that the polyhedral scaffold changes around Sr^{2+} may be attributed to the $B\text{Ø}_2O^-$ inducing AlO_x polyhedral rotation. The longest afterglow microstructure existed in this composition range, in which there was a transition in the interaction between BO_3 units and the alumina polyhedra in the aluminoborate melt. Three-fold boron coordinated with oxygen from alumina polyhedra, and the conversion from three- to four-coordinated boron induced volume change in the alumina polyhedra. It appears that the boron structural anomaly in this composition range was related to the alumina polyhedral rotation.

For $x > 40$ mol% B_2O_3, the BO_3/BO_4 ratio defined the network character. Strontium metaborate (SrB_2O_4) precipitated, with Sr^{2+} providing charge compensation for the excess non-bridging oxygen. Because Sr^{2+} was occupied in (SrB_2O_4), the stoichiometry of Sr:Al in the melt changed. The Al-rich regions precipitated as SA6, consistent with the increased SA6 content revealed by Rietveld phase fraction analysis.

3.4 Conclusion

The longest persistent luminescence in S4A7EDxB compounds synthesized by Pechini processing was observed in compounds prepared with 30-40 mol% B_2O_3. Micro-Raman analysis of S4A7EDxB grains revealed the presence of borate supramolecular structures in their orthorhombic $Sr_4Al_{14}O_{25}$ crystal structure as $BØ_3$, $BØ_2O^-$, and $BØ_4^-$ units, with an equilibrium between $BØ_2O^-$ and $BØ_4^-$ units. $BØ_4^-$ units replaced $BØ_3$ ones in the network of polymerized $BØ_3/BØ_2O^-$ groups and induced deformation in the scaffold of interconnected AlO_4 polyhedra that lead to increased Sr^{2+} site volume. These results suggest that the enlarged Sr sub-lattice sites neighboring the negatively charged non-bridging oxygen accommodate Eu and Dy dopant incorporation, giving rise to clustering of ionic point defects that support persistent luminescence.

CHAPTER 4: OXIDE GLASS FORMERS EXTENDING PERSISTENT LUMINESCENCE IN EUROPIUM AND DYSPROSIUM CO-DOPED STRONTIUM ALUMINATES

4.1 Introduction

Ceramic pigments emitting persistent luminescence (PersiL) offer illumination with zero energy consumption in safety signage and paint. Although the use of boron oxide in processing Eu and Dy co-doped strontium aluminate compounds revealed a dramatic extension of PersiL, from 10 minutes to longer than 10 h [1,2], it is not clear if this property is unique only to boron, or if other dopants may also extend PersiL by imparting similar changes to the structure of PersiL compounds. In previous work, we have shown that although Eu and Dy co-doped $Sr_4Al_{14}O_{25}$ (S4A7ED) synthesized with 30-40 mol% B_2O_3 displayed the longest duration of PersiL, these compositions do not contain the highest amount of the long persistence phases. We have additionally observed vibration modes of borate polyanions in S4A7ED, particularly ones containing negatively charged non-bridging oxygen (NBO) [59]. Moreover, we have observed clustering of the rare earth dopants incorporating into Sr^{2+} sites in S4A7ED [47]. These results combined suggest that a critical amount of boron is necessary to induce clustering of ionic point defects in S4A7ED, and specifically by introducing NBOs.

Although B_2O_3 was initially used in processing of strontium aluminate as a sintering flux agent, to facilitate synthesis at lower temperatures and promote grain growth, precursors of other oxide glass forming cations, such as Si, P, V, and Zr, have also been used to produce afterglow compounds, such as rare-earth doped silicates and phosphates [14–19] [60]. Si^{4+} incorporation in $Sr_{1-x/2}Al_{2-x}Si_xO_4:Eu^{2+},Dy^{3+}$ was observed to extend PersiL,

attributed to increased trap depth [61]. Strontium aluminate mixed with P_2O_5 became a glass exhibiting transparency and PersiL [62]. These developments motivated us to investigate if such cations in general extend PersiL, also by contributing NBOs when incorporating into the crystal structure of the PersiL emitting phases of strontium aluminate.

Glasses of SiO_2 and P_2O_5 consist of interconnected polyhedra of oxygen-coordinated cations that share bridging oxygen anions. When a modifier cation, such as alkaline or alkaline earth cations, enters these oxide networks, some bridging oxygen become non-bridging ones, due to differences in valence. The Q^n notation was developed to facilitate discussion distinguishing polyhedral units containing different numbers of bridging oxygen (BO) and NBO. Q represents the polyhedral unit; *n* represents the number of bridging oxygen, while *n*-1 represents the number of non-bridging oxygen per tetrahedron**.** The increase in the fraction of network modifier cations in the glass system promotes the presence of Q^{n-1} units at the expense of Q^n units [21]**.**

Vitreous silica glasses are 3-D networks of SiO_4 tetrahedral units (Figure 4.1). Each SiO_4 tetrahedron is connected to neighboring tetrahedra via its four corners, resulting in four bridging oxygen atoms per tetrahedron. A tetrahedron with four BO is referred to as Q_{Si}^4 groups. Q_{Si} represents a SiO_4 tetrahedral unit, *n* represents the number of bridging oxygen per SiO_4 unit, such that *n* = 0, 1, 2, 3, 4, as shown in Figure 4.1: Q_{Si}^0 $[SiO_4]^{4-}$, Q_{Si}^1 $[SiO_{3.5}]^3$, Q_{Si}^2 $[SiO_3]^{2-}$, Q_{Si}^3 $[SiO_{2.5}]^{1-}$, Q_{Si}^4 $[SiO_{2.}]^0$ [21,63].

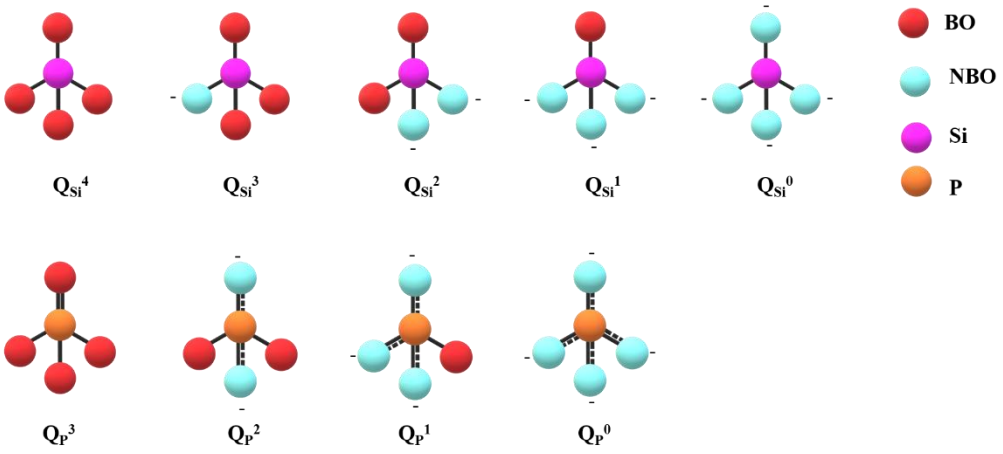

Figure 4.1 Q^n structural types in silicate and phosphate glasses.

Because P is pentavalent, vitreous phosphate is composed of PO_4 tetrahedral units—three bridging oxygen (BO) and one doubly bonded oxygen bond (DOB)—as shown in Figure 4.1 as a Q_P^3 (P_2O_5) units. Q_P represents a PO_4 tetrahedral unit, while *n* represents the number of bridging oxygen—0, 1, 2, or 3. In phosphate glasses, the DOB is considered equivalent to NBOs of the PO_4, because the DOB and the NBO are indistinguishable, as the negative charge is delocalized over both oxygen atoms[64–66]. With the addition of modifier amount, some BO change to NBO, and Q_P^{n-1} units form. Q_P^2 (PO_3^-) has two BOs, while the DOB becomes an NBO, and the two NBO bonds ($P\text{-}O^-$) share a negative charge. Q_P^1 ($P_2O_7^{4-}$) units have one BO and three NBO. Orthophosphate Q_P^0 (PO_4^{3-}) units have four NBOs[21,65–69].

Both P^{5+} and Si^{4+} form tetrahedral oxide networks; however, due to the DOB, phosphate networks have weaker connectivity [69]. The formation of Q^n with different BO/NBO in silicates and phosphates glasses depends on the stoichiometry of the glass composition—*i.e.*, the valence of the modifier cation.

As a network intermediate, ZrO_2 acts as a network former or as a modifier depending on the concentration and chemistry of the oxide glass system. Zirconium ions are mostly six-fold coordinated. ZrO_6 octahedra link with other network formers, such as SiO_4 and AlO_4 tetrahedra, through corner-sharing [70,71].

V_2O_5 is a network former. In addition to the VO_5 pyramids,vitreous vanadium pentoxide may contain $V^{5+}O_4$ tetrahedra with V=O apex and three bridging oxygen [72,73].

The structural anomaly in oxide glass networks occurs when the network structure is dependent on the stoichiometry, due to changing functions of a constituent cation—as a network intermediate that can function as a former over certain compositional range and as a modifier over other compositions. Al_2O_3 is such a network intermediate, and the oxygen coordination number of Al can be $^{[4]}$Al, $^{[5]}$Al, and $^{[6]}$Al, depending on the local network structure and composition [74]. In the case of the S4A7ED crystal structure, SrO is a network modifier, and the presence of Sr^{2+} provides local electrical charge compensation [75,76].

Although the glasses do not have a long-range structural order, they still have a short-range order in their atomic arrangements. In previous studies, vibration spectroscopy techniques have proved useful in determining the structure and local environment of glassy systems and polymorphic crystal structures**.** To elucidate the local structure in the modified glass and crystalline structures, Raman and infrared spectroscopy are commonly used. Raman and FTIR analysis of different strontium aluminates phases were reported in several studies [2,22–24,59] . We had recently applied these techniques to elucidate that borate polyanions extended PersiL in S4A7ED when incorporated into the crystal structure. By introducing excess negative charge through NBOs and consequently enlarging adjacent Sr sites, they enable clustering of Eu^{2+} and Dy^{3+} incorporating into adjacent Sr sub-lattice sites [59].

In this study, to examine the effect of glass-forming oxides on PersiL in S4A7ED, we synthesized S4A7ED with different amounts of glass-forming oxide precursors by the Pechini method. We analyzed the local structural environment in different glass-forming oxides by using micro-Raman and FTIR spectroscopy and related the polyanion structure and content to the crystalline phase composition and PersiL duration.

4.2 Results

Each S4A7ED*mX* compound was illuminated with a 365 nm UV light source, and the composition with the longest PersiL was selected for further analysis as the representative "hero" one for that *X* group. In the luminescence decay curves (Figure 4.2), PersiL duration was plotted with a minimum value of 0.32 mcd-m^2, which is *ca.*100 times the sensitivity of the human eye [77]. Table 4.1 summarizes the PersiL duration for each compound characterized.

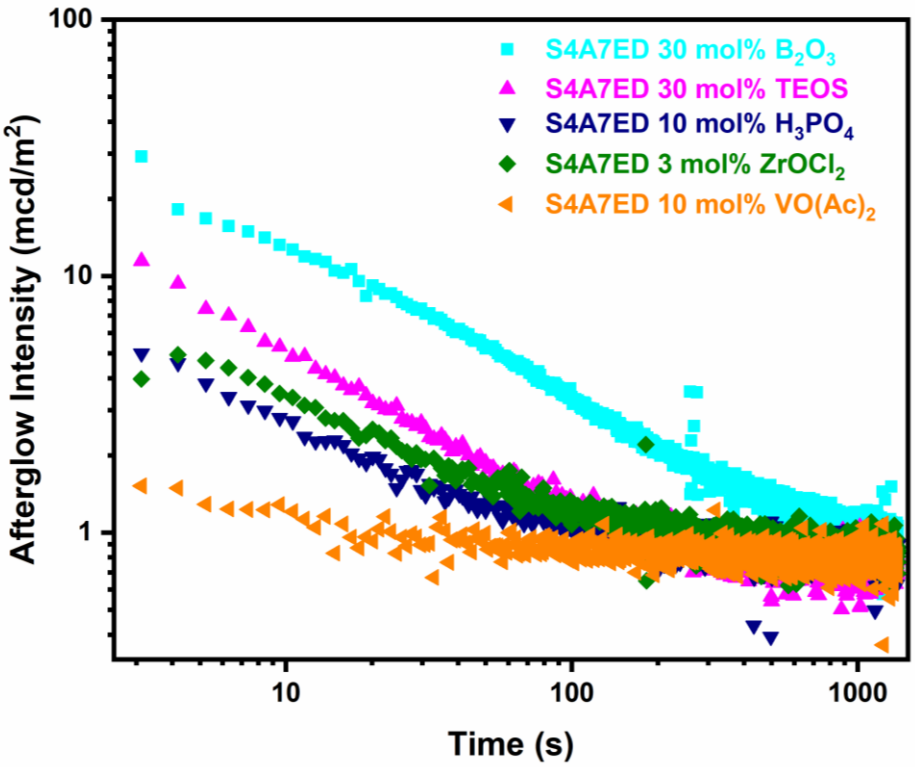

Figure 4.2 Afterglow decay curves for the hero S4A7EDmX compounds.

Table 4.1 PersiL decay to 0.32 mcd-m-2 duration of the hero S4A7EDmX compounds.

Sample Name	**Decay to 0.32 mcd-m^{-2} (s)**
S4A7ED 30 mol% B_2O_3	600
S4A7ED 30 mol% TEOS	350
S4A7ED 10 mol% H_3PO_4	150
S4A7ED 3 mol% $ZrOCl_2$	280
S4A7ED 10 mol% $VO(Ac)_2$	50

Figure 4.3 summarizes the results of phase composition analysis applied to the hero S4A7ED*mX* compounds. Normalized X-ray diffractograms of these compounds are shown in Figure 4.3 (a), while the relative amount of crystalline phase is shown in Figure 4.3 (b), and the Rietveld phase fraction analysis of the crystalline phases is summarized in Figure 4.3 (c). Table 4.2 summarizes the actual phase fractions and percent crystallinity.

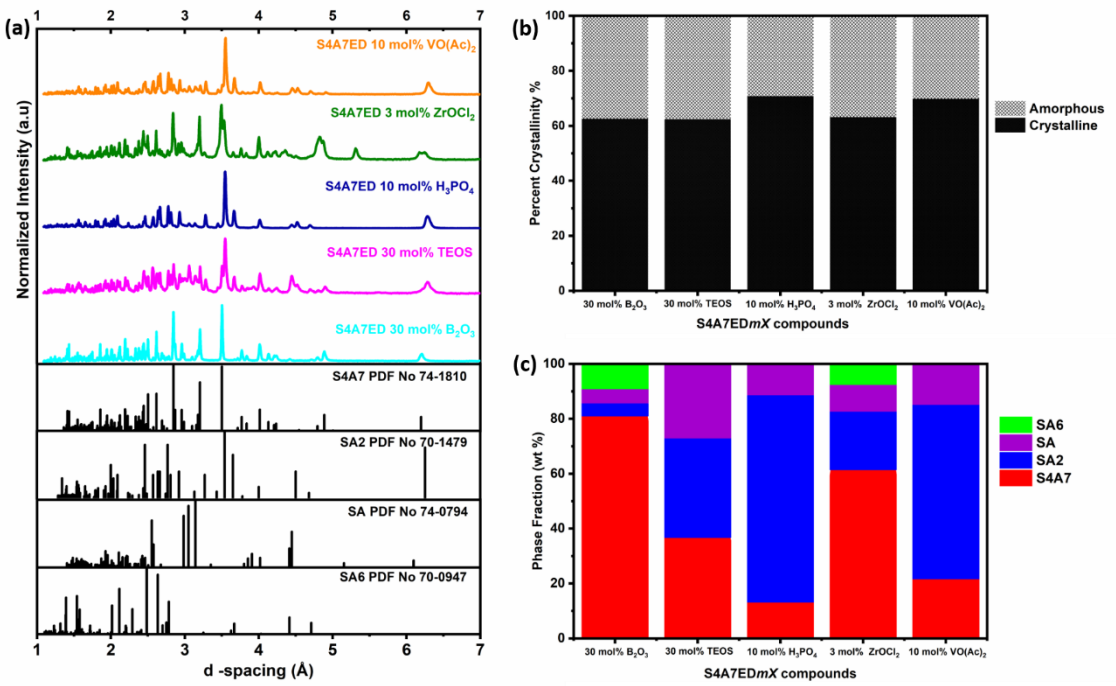

Figure 4.3 (a) X-ray diffractograms of hero S4A7EDmX compounds; b) Percent crystallinity and amorphous phase fraction determined from the XRD data of S4A7EDmX samples; c) Phase distribution revealed by Rietveld phase analysis of the diffractograms shown in Figure 4.3 (a).

The percent crystallinity was comparable in all compounds. The longest PersiL compound of S4A7ED*mX* with B_2O_3 was composed predominantly of S4A7 phase—*i.e.*, around 80 mol%. The S4A7ED*mX* compound with 30 mol% TEOS exhibited a relatively more equal distribution of SA, SA2, and S4A7 phases. An increase in the amount of TEOS had favored the formation of S4A7 phase (Figure 4.4 (a)) (Table 4.2). S4A7ED*mX* with 10 mol% H_3PO_4 was of predominantly SA2 phase (*ca.* 75%). An increase in the amount of H_3PO_4 correlated with increased SA2 phase content. (Figure 4.4 (b)) (Table 4.2). S4A7ED*mX* with 3 mol% $ZrOCl_2$ contained *ca.* 61 mol% S4A7. When the amount of Zr was increased, the S4A7 and SA2 phase content decreased, while the SA phase content increased (Figure 4.4 (c)). S4A7ED*mX* with 10 mol% $VO(Ac)_2$ consisted of *ca.* 63 mol% SA2. Figure 4.4 (d) and Table 4.2 show that increasing the V content resulted in more SA2 formation.

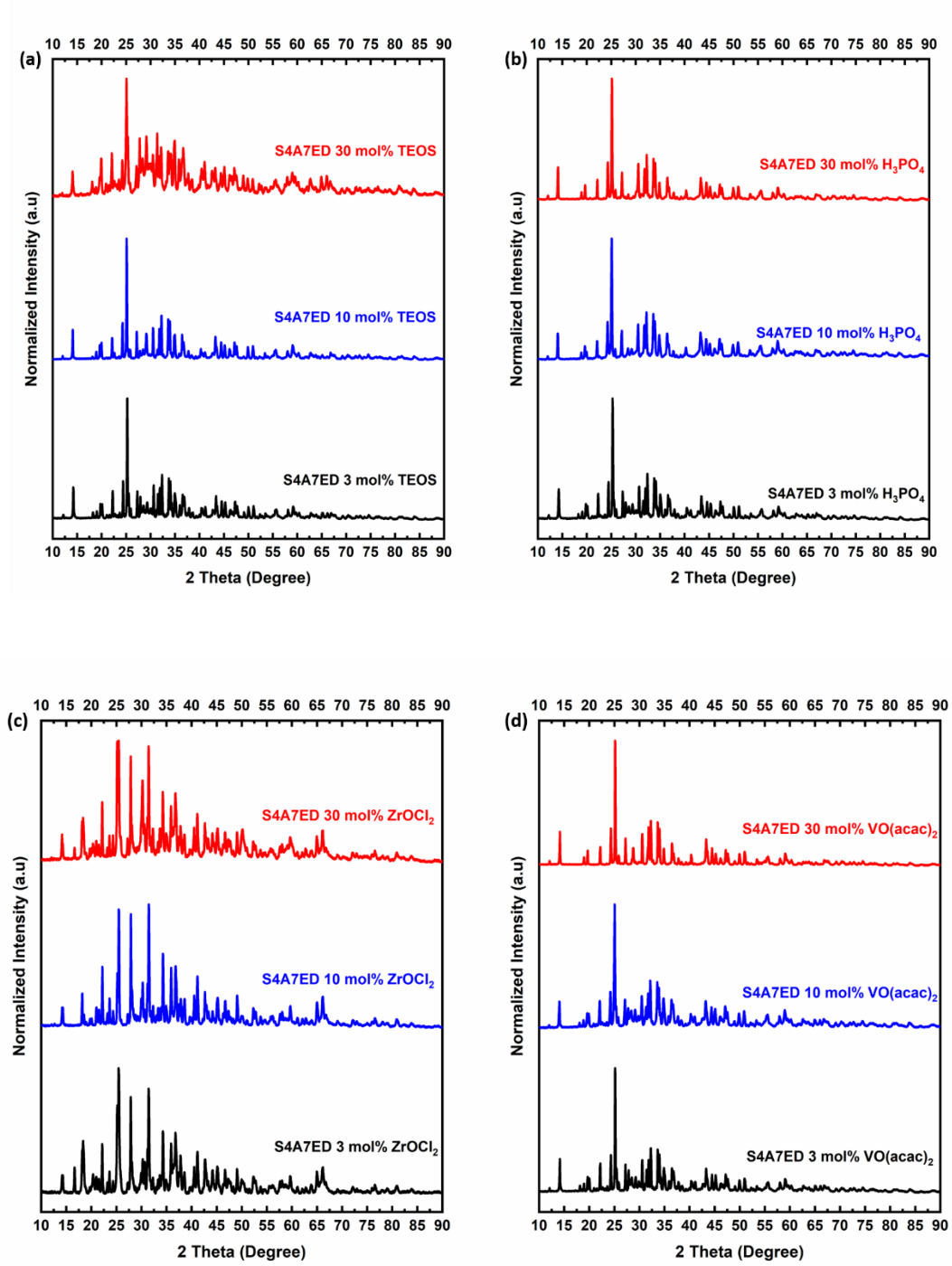

Figure 4.4 X-ray diffractograms of S4A7ED*mX* compounds a) TEOS ; b) H_3PO_4 ; c) $ZrOCl_2$; d) $VO(Ac)_2$

Table 4.2 Rietveld Phase Fraction and the percent crystallinity of the all S4A7ED*mX* compounds.

Composition	**Fraction of crystalline phase (%)**					
	S4A7	**SA2**	**SA**	**SA6**	**$Sr_3(VO_4)_2$**	**Goodnes of Fit**
S4A7ED 3 mol% TEOS	27.75	60.66	14.60			1.91
S4A7ED 10 mol % TEOS	11.38	71.60	17.02			2.55
S4A7ED 30 mol% TEOS	36.77	36.22	27.02			2.18
S4A7ED 3 mol% H_3PO_4	20.12	66.77	13.10			1.87
S4A7ED 10 mol% H_3PO_4	13.26	75.44	11.31			1.82
S4A7ED 30 mol% H_3PO_4	11.41	84.60	4			2.06
S4A7ED 3 mol% $ZrOCl_2$	61.45	21.30	9.73	7.51		2.51
S4A7ED 10 mol% $ZrOCl_2$	79.40	15.16	5.44			1.80
S4A7ED 30 mol% $ZrOCl_2$	48.32	19.58	18.65			3.34
S4A7ED 3mol% $VO(acac)_2$	23.13	63.58	13.29			1.83
S4A7ED 10 mol% $VO(acac)_2$	21.72	63.46	14.81			1.81
S4A7ED 30 mol% $VO(acac)_2$		91.75			8.25	2.72

The FTIR spectra were analyzed to identify the structural changes in strontium aluminate compounds correlating to the different oxide glass formers. Spectra over the region 600-4000 cm^{-1} are shown in Figure 4.5 (a). Above 1600 cm^{-1} no vibrations modes were observed. Characteristic vibrations of O-Al-O were observed in 600-1000 cm^{-1} region (Figure 4.5 (b)) for the phase-pure, undoped strontium aluminate phases from the reference spectra [59]. The FTIR spectrum of S4A7ED 3 mol% $ZrOCl_2$ (Figure 4.5 (b)) showed peaks at *ca.* 1050 cm^{-1} assigned to Zr-O and 1500 cm^{-1} assigned to Zr-OH bonds [78][70]. S4A7ED 10 mol% $VO(Ac)_2$ had an absorption band at *ca.* 1000 cm^{-1} (Figure 4.5 (b)), which was assigned to the V=O bond [72,73]. Table 4.3 summarizes the FTIR bands identified in all hero S4A7ED*mX* compounds.

To identify the absorbance bands related to SiO_4 and PO_4 tetrahedra with NBOs, these FTIR spectra were scrutinized in further analysis, for S4A7ED*mX* prepared with TEOS and H_3PO_4. The FTIR spectra of S4A7ED*mX* with 3, 10 and 30 mol% TEOS are

summarized in Figure 4.5 (c). The weak shoulder at 950 cm^{-1} was assigned to anti-symmetric stretching bands of Q_{Si}^2 units, which are SiO_4 tetrahedra with two BOs and two NBOs [79,80]. The band at *ca.* 1070 cm^{-1} was assigned to the Q_{Si}^3 antisymmetric stretching vibration of SiO_4 tetrahedra with three BOs and one NBO [79].

Structural changes in S4A7ED*mX* with 3, 10 and 30 mol% H_3PO_4 are shown in Figure 4.5 (d). The FTIR bands at *ca.* 1000-1150 cm^{-1} were assigned to the stretching vibrations of (PO_3^{3-}) groups containing NBOs [21,81,82]. The FTIR band at 950-850 cm^{-1} was assigned to asymmetric P-O-P stretching vibrations of phosphate tetrahedra with one BO and two NBOs, *i.e.*, the Q_P^1. Symmetric P-O-P stretching of Q_P^1 was additionally observed at 790-690 cm^{-1} [67].

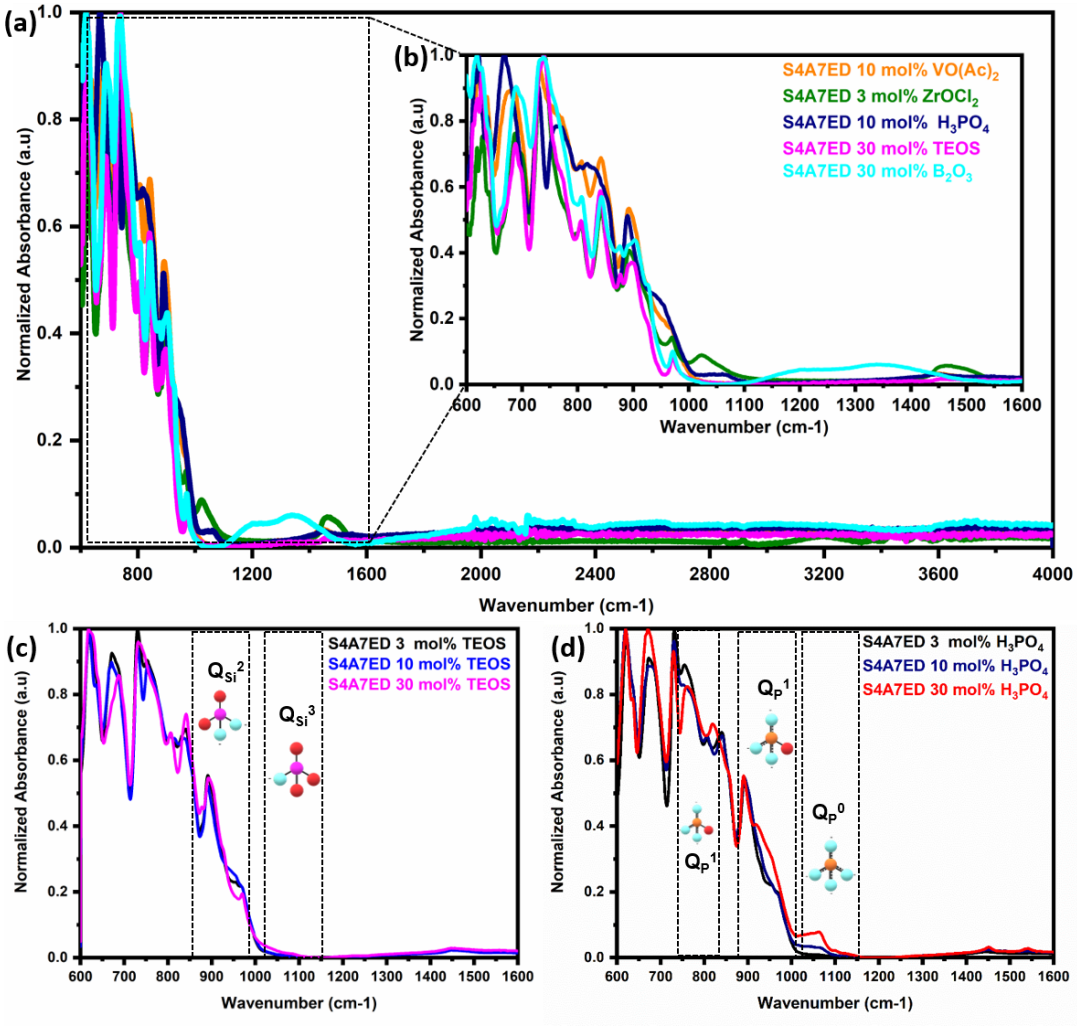

Figure 4.5 a) Full range FTIR spectra for S4A7ED*mX* compounds; b) 600-1600 cm^{-1} magnified; c) FTIR spectra for S4A7ED*mX* with 3, 10 and 30 mol% TEOS and d) FTIR spectra for S4A7ED*mX* with 3, 10 and 30 mol% H_3PO_4.

Table 4.3 Assignments of FTIR bands for hero S4A7ED*mX* compounds.

S4A7ED*mX* compounds	**Band (cm^{-1})**	**Assignment**
S4A7ED 30 mol% TEOS	950	Q_{Si}^2 antisymmetric stretching bands[79,80]
	1070	Q_{Si}^3 antisymmetric stretching bands[79,80]
S4A7ED 10 mol% H_3PO_4	790-690	symmetric P-O-P stretching of Q_P^1[21,67,82]
	950-850	asymmetric P-O-P stretching vibrations phosphate tetrahedron Q_p^1[67,83]
	1000-1150	P-NBO bonds stretching vibrations PO_3^{3-} [21,67,82,83]
S4A7ED 3 mol% $ZrOCl_2$	1050	Zr-O [78]
	1500	Zr-OH [78]
S4A7ED 10 mol% $VO(Ac)_2$	1000	V=O [84,85]

Micro-Raman spectra analyses are summarized in Figure 4.6, revealing localized atomic arrangements in the hero S4A7ED*mX* compounds. Table 4.4 summarizes the assigned Raman bands for these S4A7ED*mX* compounds. The Raman spectra of the phase-pure strontium aluminate compounds—S4A7, SA2, SA, and SA6—were used as the reference fingerprints[59]**.** The main 398 cm^{-1} peak for SA2 appeared in all compositions, except in S4A7ED*mX* with B_2O_3. For each compound, peaks in the larger Raman shift regime were observed, corresponding to localized vibrations around the oxide glass former cations, and demarcated with dashed vertical sight lines to facilitate their comparison (Figure 4.6 (a)).

The Raman spectrum of S4A7ED*mX* with 3 mol% $ZrOCl_2$ revealed a vibration mode at *ca.* 1200 cm^{-1}, related to Zr–O stretch in ZrO_4 units and Zr-OH. [78]. S4A7ED*mX* with 10 mol% $VO(Ac)_2$ showed the Raman mode of V=O at *ca.* 1000 cm^{-1} [84,85].

Raman spectra of different amounts of S4A7ED*mX* with TEOS are summarized in Figure 4.6 (b). S4A7ED*mX* with 30 mol% TEOS exhibited the most prominent shift in the 1000-1150 cm^{-1} region, which was assigned to the stretching modes of more-polymerized silicate groups. In the literature, Raman vibrations in the region 800-1200 cm^{-1} were assign to Si–O stretching vibrations in SiO_4 tetrahedra with NBOs [80,86]. The band deconvolution analysis is shown in Figure 4.6 (c) for the 1020-1140 cm^{-1} region, revealing the distribution of the Q_{Si}^n species. The strongest band centered at 1077 cm^{-1} was assigned to Q_{Si}^2, with much weaker bands at 1046 cm^{-1} and 1094 cm^{-1}, which may be oxygen sharing Q_{Si}^3 -Q_{Si}^2 units. The weak band at 1107 cm^{-1} was assigned to Q_{Si}^3 [80,87–90]. Additionally, active modes in the region at the 600 -700 cm^{-1} were attributed to bending motions in Si−O−Si rings sharing four and three SiO_4 tetrahedra [88].

Raman spectra of S4A7ED*mX* with different amounts of H_3PO_4 are shown in Figure 4.6 (d). With an elevated PO_x content, Raman scattering was observed in the region 900-1150 cm^{-1}, and the deconvolution applied to absorption bands within this region is summarized in Figure 4.6 (e). The band at *ca.* 950 cm^{-1} was assigned to asymmetric stretching vibration of Q_P^0 $(PO_4)^{3-}$ units [91,92]. The Raman band at 1050 cm^{-1} was assigned to symmetric stretch mode of NBO in Q_P^1 units (PO_3), [21,89,93]. The vibration at *ca.* 700 cm^{-1} was attributed to symmetric stretching vibrations of P–O–P linkages Q_P^2 [92].

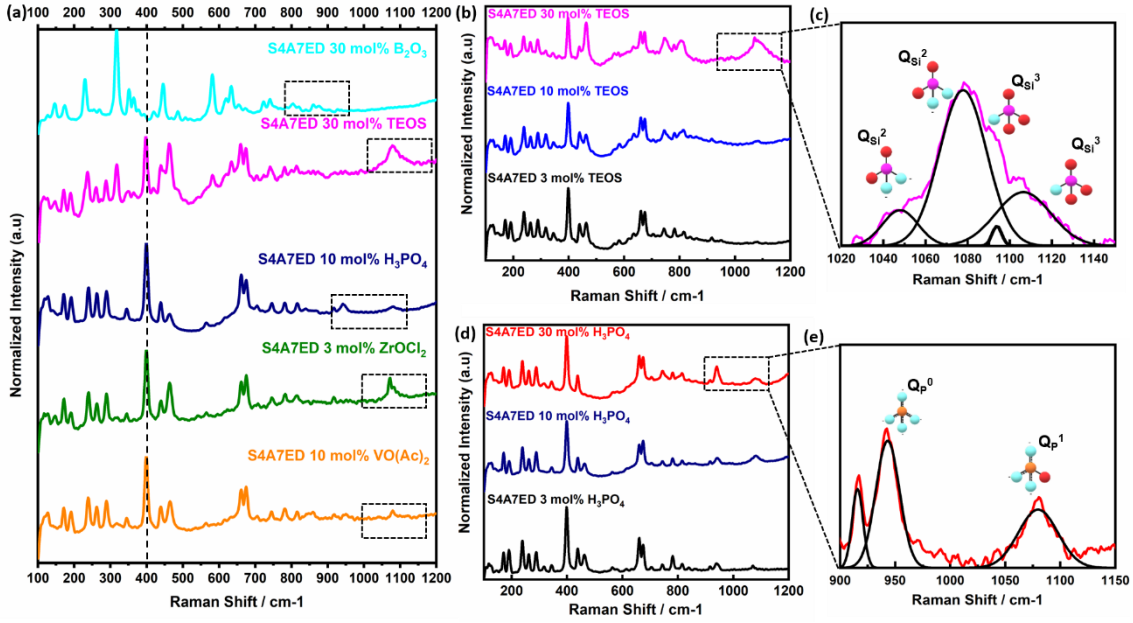

Figure 4.6 a) Raman shift spectra for S4A7ED*mX* compounds; b) Raman spectra for S4A7ED*mX* with 3,10 and 30 mol% TEOS; c) Deconvoluted Raman shift spectra for S4A7ED*mX* with 30 mol% TEOS; d) Raman spectra for S4A7ED*mX* with 3,10 and 30 mol% H_3PO_4 ; e) Deconvoluted Raman shift spectra for S4A7ED*mX* with 30 mol% H_3PO_4.

Table 4.4 Assignment of Raman bands for the hero S4A7ED*mX* compounds.

S4A7ED*mX* compounds	**Band (cm^{-1})**	**Assignment**
S4A7ED 30 mol% TEOS	630	bending motions in Si−O−Si rings [74,80,88]
	1046	symmetric stretching modes of Q_{Si}^2 units [80,87,88]
	1077	symmetric stretching modes of Q_{Si}^2 and Q_{Si}^3units[87]
	1107	symmetric stretching modes of Q_{Si}^3units [87–90]
S4A7ED 10 mol% H_3PO_4	700	symmetric stretching vibrations of P–O–P linkages Q_P^2 [92,94]
	950	asymmetric stretching of Orthophosphate species Q_P^0 [92–96] [91]
	1050	symmetric stretch mode of NBO in Q_P^1 units [21,64,89,93,95]
S4A7ED 3 mol% $ZrOCl_2$	1200	Zr–O stretch in ZrO_4 units and Zr-OH [78]
S4A7ED 10 mol% $VO(Ac)_2$	1000	V=O [85]

Figure 4.7 shows the excitation and emission spectra measured from the S4A7ED*mX* compounds. Table 2.5 summarizes the measurement range with maximum excitation and emission values for each compound. The excitation spectra were relatively similar. The maximum excitation wavelength changed with the incorporated oxide glass former cation, indicating changes in the electronic transition probability in Eu^{2+} (Figure 4.7 (a)). Figure 4.7 (b) shows the emission response of each S4A7ED*mX* compound, stimulated by their maximum excitation wavelength.

As seen in Figure 4.7 (a), the excitation spectra were obtained for all S4A7ED*mX* compounds using emission in the 490-495 nm range, except for S4A7ED*mX* with 10 mol% H_3PO_4. The emission required at 405 nm for obtaining the maximum excitation efficiency for this compound suggested that a different dominant phase was hosting the optically active Eu^{2+}.

Emission spectra of each multi-phase S4A7ED*mX* compound shown in Figure 4.7 (b), with the excitation wavelength for the measurement indicated in the legend. Overall, the broad emission band at *ca.* 490 nm and narrower one at *ca*. 400 nm were consistent with Eu $^{2+}$ emission from crystallographically non-equivalent Sr-sites in S4A7 [3,97,98]. The broad emission band at *ca*. 515-520 nm was assigned to Eu^{2+} emission in SA at room temperature[41,99–101] . Spectral deconvolution analysis revealed additional emission bands associated with Eu^{2+} in SA2 at *ca.* 475 nm [97]; Eu^{3+} in S4A7 at *ca.* 560 nm [4,102]; and Dy^{3+} in different strontium aluminates phases at *ca.* 575 nm [3,103,104].

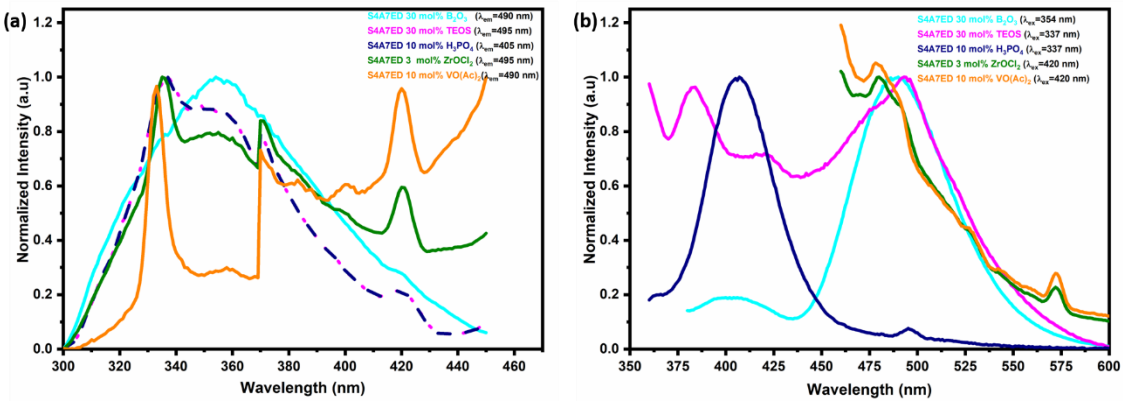

Figure 4.7 a) Excitation and b) emission spectra of the hero S4A7ED*mX* compounds.

4.3 Discussion

PersiL was observed in Eu,Dy co-doped strontium aluminate synthesized by Pechini processing using 4 different oxide glass forming precursors containing B, Si, Zr, and P. While B doping extended PersiL the longest, doping with Si, Zr, and P still extended PersiL perceptibly to the naked eye, and V had no effect.

Although the initial stoichiometry (S4A7ED) and processing conditions were the same for each composition, different phase compositions had formed. Rietveld phase analysis in Figure 4.3 (c) revealed a lack of correlation between the amount of phases exhibiting the room temperature PersiL, SA and S4A7, and the PersiL duration. Similar to what we had previously observed in B-doped compounds[59], the longest PersiL duration appeared in S4A7ED processed with 30-40 mol% B_2O_3, which did not contain the highest combined amount of SA and S4A7.We observed in this study that different oxide glass former cations preferentially stabilized the formation of the S4A7 phase to different degrees. As for B_2O_3-containing compounds, increasing Si up to 30 mol% (3, 10 and 30 mol% TEOS) preferentially stabilized S4A7. However, there was no correlation between the S4A7 phase content and oxide glass former content in the compounds containing Zr, P, and V.

The material structure supporting PersiL was defined by the way that the oxide glass forming cations tuned atomic arrangements in the host lattice. B_2O_3, SiO_2, P_2O_5 and V_2O_5 are all network-forming oxides, while ZrO_2 is a network intermediate. The structure of strontium aluminates consists of a scaffold of corner- and edge-sharing Al coordination polyhedra defining large cavities occupied by charge compensating Sr^{2+} cations. Because AlO_x coordination varies with stoichiometry CN = 4, 5 and 6, the oxide network formers modify the oxygen coordination of AlO_x to meet local requirements for charge compensation. The interactions of the oxide glass forming cations with Al and Sr thus defined the most stable atomic arrangements; additionally, via the ratio Sr/Al, they determined the most stable crystal phase.

Oxide glass formers tend to form NBO ions to different degrees. The addition of the modifier oxides to silicate and phosphate glasses induces the formation of NBO ions. In the boron structural anomaly, low concentrations of modifier oxides enable planar, trigonal charge-neutral [$BØ_3$] triangles to transform to negatively charged, tetrahedral $[BO_4]^-$ of 3-D character. Increasing the content of modifier oxides induced the formation of NBOs on borate polyanions, such as meta $[BØ_2O]^-$, pyro $[BØO_2]^{2-}$ and ortho $[BO_3]^{3-}$ units. In recent work, we reported that boron effectively densified the alumina polyhedral network at low modifier concentrations, while the increase in NBOs yielded increased free volume in the network at elevated modifier concentrations. Use of different oxide

glass formers appeared to change the distribution of AlO_X units within the amorphous preceramic; such changes in their connectivity would influence the formation of the crystal scaffold.

FTIR and Raman spectroscopy were well-suited for elucidating the vibration modes of oxygen bonds and coordination polyhedral units, as we sought to determine the BO/NBO ratio present in other compounds exhibiting PersiL. As detected in S4A7ED*mX* with 30 mol% B_2O_3, NBOs in polyanion units were also revealed by FTIR analysis of S4A7ED*m*X compounds doped with Si (Q_{Si}^2 and Q_{Si}^3 units) and P (Q_P^1 and Q_P^0 units). These polyhedra share BOs, indicating a BO/NBO ratio > 0. Raman scattering from $[BØ_3]$, $[BØ_4]^-$ and metaborate $[BØ_2O]^-$ was revealed in S4A7ED*mX* with 30 mol% B_2O_3. Similar polyanion moieties with both BO and NBOs were observed in the hero Si-doped S4A7ED*mX* compound, Q_{Si}^2 and Q_{Si}^3, which corresponds to $[SiO_3]^{2-}$ and $[SiO_{2.5}]^{1-}$, reflecting the presence of a polymerized SiO_4 network with NBO. In the hero P-doped S4A7ED*mX* compound, we detected the orthophosphate Qp^0, which is PO_4^{3-} and with four NBOs, and Qp^1, which is $P_2O_7^{4-}$, with one BO, three NBO. Notably, increased orthophosphate monomer content was detected at 950 cm^{-1} with higher P doping—*i.e.*, moieties with only NBOs and no BOs—in compounds exhibiting less PersiL, or even none at all. Because Zr and V polyanions were not as well-studied in the literature, such an analysis could not be applied to their FTIR and Raman spectra. It nonetheless appears that borate, silicate, and phosphate polyanions should have a BO/NBO ratio greater than zero to contribute to PersiL. The negatively charged NBO is necessary to induce the clustering of Eu^{2+} and Dy^{3+} in S4A7 that gives rise to PersiL. It is important to highlight that the use of micro-Raman analysis is essential to these results, because the signal-to-noise is superior to that in FTIR and because micron-scale spatial resolution can be achieved, enabling the well-defined analysis of grains larger than a micron.

PL spectra revealed Eu^{2+} hosted in multiple crystal environments, consistent with analysis of multi-phase compounds. Characteristic emission bands of the $4f^7$-$4f^6 5d^1$ transition occurring from Eu^{2+} incorporating substitutionally into the 2 crystallographically non-equivalent sites in S4A7 in S4A7ED*mX* compounds doped with B, Si, Zr, and V. In the P-doped S4A7ED*m*X, the strong broad emission at *ca.* 400 nm may arise from Eu^{2+} in SA2, SA or S4A7[97] . Thermal broadening in room temperature PL measurements

prevent distinguishing between these possibilities. In fact, analysis of the phase composition revealed the presence of mixtures of these phases in the hero S4A7ED*mX* compounds, as well as SA6 in the case of B- and Zr-doped compositions.

The longest PersiL compounds were the B-doped ones, followed by the Si-, the Zr-, the P-, and finally the V-doped ones, in order of decreasing duration. It should be noted that long PersiL correlated with high S4A7 phase content, in the case of B and Zr doping, while Si doping yielded a high combined S4A7 and SA content (66.79 %), both of which are room temperature PersiL phases. In these compounds, emission from Eu^{2+} in S4A7 dominates the luminescence spectra. In contrast, the hero P-doped S4A7ED*mX* compound, SA2 is the dominant phase, and emission from Eu^{2+} in an SA2 host dominates the luminescence spectra. This result is particularly notable, because Eu^{2+} in SA2 is not a PersiL phase at room temperature without the P doping [97].

As shown in Figure 4.8, S4A7 and SA each have 2 crystallographically non-equivalent Sr sites for hosting Eu^{2+} and Dy^{3+}. In the case of S4A7, one site is coordinated by 7 oxygens and the other by 10 oxygens; while in SA, both sites are coordinated by 7 oxygens**.** In SA2, there is only a single Sr site geometry, and there are 2 in the middle of the unit cell occupying a large cavity defined by the Al polyhedral scaffold. The presence of a NBO may be tuning their positions such that Eu^{2+} and Dy^{3+} incorporate substitutionally into these adjacent sites and are situated at a separation enabling the efficient energy transfer manifesting as PersiL.

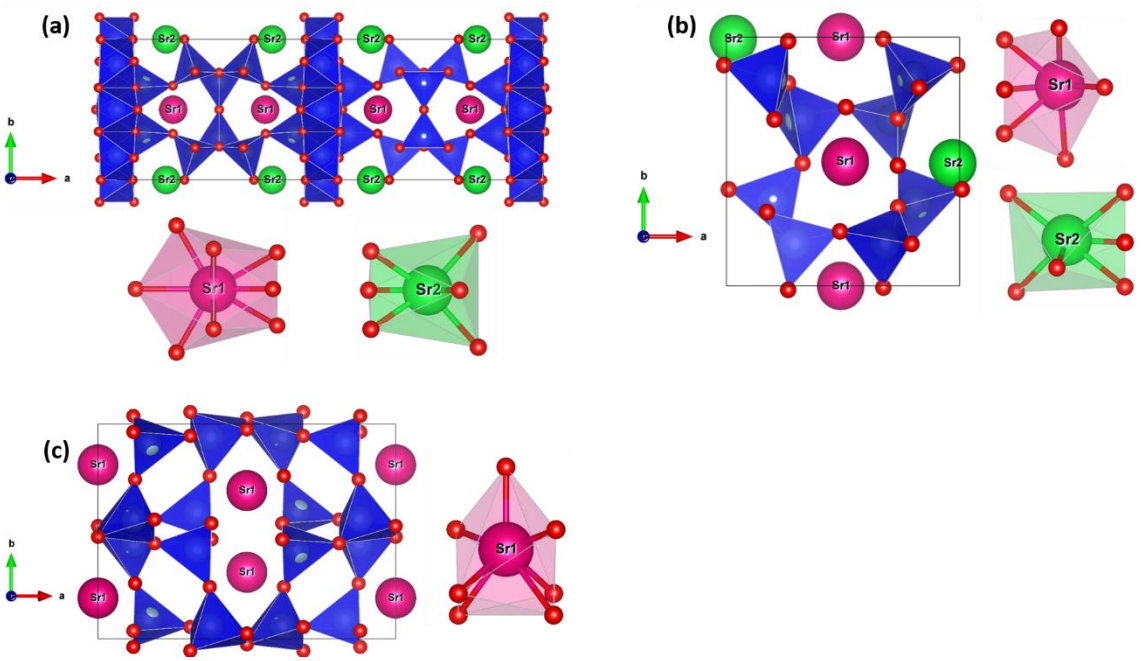

Figure 4.8 Crystal structure of a) S4A7, b) SA, and c) SA2, showing Sr sites hosting substitutionally incorporated rare earth dopants.

4.4 Conclusion

Oxide glass former cations extend persistent luminescence in Eu^{2+} and Dy^{3+} co-doped $Sr_4Al_{14}O_{25}$ compounds forming from an amorphous preceramic. Although B incorporation into the crystal structure of S4A7 induces clustering of Eu and Dy in the most efficient configuration for energy transfer leading to PersiL, the incorporation of Si, Zr, and P also emit PersiL from compounds consisting of a mixture of S4A7, SA, and SA2, albeit to a more limited extent. V doping does not yield PersiL in S4A7. In the case of Si and P, these cations are incorporated into the crystal structure as silicate and phosphate polyhedra with a non-zero ratio of BO to NBO. Although the reported data for Zr coordination polyhedra are limited, preventing the determination of Zr polyanions with NBO, its efficient extension of PersiL is clear. The results of this study show that the oxide glass formers, Si, P, and Zr also extend PersiL in S4A7ED compounds, like B. Moreover, P doping stabilizes the SA2 stoichiometry, and the phosphate polyanions

induce structural changes enabling PersiL, in a phase that would otherwise not emit room temperature PersiL.

CHAPTER 5: APPLICATION OF FTIR AND MICRO-RAMAN SPECTROSCOPY FOR ANALYZING POLYCRYSTALLINE CERAMIC STRONTIUM ALUMINATE COMPOUNDS

5.1 Introduction

Infrared Spectroscopy is one of the vibrational spectroscopy techniques, which is based on the interaction of electromagnetic radiation in the IR region with a matter. Infrared spectroscopy measures the absorption of IR radiation with the change in the dipole moment of each bond in the molecule[105]. Raman is a vibrational spectroscopy technique based on monochromatic laser light to induce electrical polarization of the structural features in the materials. Raman spectroscopy measures the shift in the wavelength of the incident photon due to the excitation of molecular vibrations [106]. These techniques have proved useful in determining the structure and local environment in polymorphic crystal structure and in glassy ones. Raman and infrared spectroscopy are commonly used as complimentary techniques for elucidating the local structure in modified glass and crystalline structures [26–32] [49].

Rietveld phase analysis of XRD data reveals that multiple competing phases are forming during our usual preparation of long afterglow, doped $Sr_4Al_{14}O_{25}$ by the Pechini method. Because multiple phases are being interrogated simultaneously, it is challenging to determine the atomic structure and subtle changes to atomic position due to incorporated dopants. Moreover, while EDX analysis in an electron microscope is useful for mapping elemental distribution, such methods will not provide information on the actual atomic arrangements of atoms in a crystalline solid. Instead, micro-Raman spectroscopy offers spatial resolution on the size scale of our ceramic powders, as well as the potential for

phase identification, and FTIR spectroscopy complementarily reveals the presence of non-active Raman vibration modes.

We first prepared pure, single-phase reference powders of monoclinic $SrAl_2O_4$, monoclinic $SrAl_4O_7$, hexagonal $SrAl_{12}O_{19}$ and orthorhombic $Sr_4Al_{14}O_{25}$. We generated reference sets of vibration spectra, *i.e.*, their fingerprints, using micro-Raman and FTIR spectroscopy. These fingerprints were then applied to determine the phase of each grain evaluated in the undoped version of our long afterglow $Sr_4Al_{14}O_{25}$.

Data collection by the FTIR method for strontium aluminate compounds is described in detail in Chapter 2. Ground powder was used to collect data in ATR mode and the steps to be followed to obtain accurate measurements with this technique are explained. However, more procedures were required to obtain consistent results with Raman spectroscopy, and these are described in detail in the next section.

5.2 Micro-Raman Spectroscopy Data Collection of the Strontium Aluminate Compounds

Micro–Raman spectrometer use a confocal optical microscope coupled to a Raman spectrometer to collect the spatially resolved spectra. The microscope focuses light from the laser onto the sample and collects photons scattered from a point on the analyzed sample [107].

We collected the reference spectra of each phase with powder samples. The powders were finely ground and pressed between two glass slides to provide a smooth surface for measurement. If the surface of the sample is not smooth, it is difficult to focus both the excitation and collection optics on the sample at the same time.

Analyzing the multiphase strontium aluminate powders with this approach was very challenging. Because the grains of each phase are indistinguishable from the pile of powder, the Raman signals of each phase overlapped. The solution was to use a well-

polished sintered pellet to focus the micron-sized particles of each phase during measurement.

The sintered pellet was prepared from finely ground powders under 70 bar pressure for 2 minutes. The pellet was then embedded in resin epoxy to easily polish the surface of the sample. As mentioned in Chapter 2, the system was first calibrated with Si, and then the sample was carefully placed on the sample stage. Focus adjusted for 5x, 20x and 50x numerical aperture by rotating the center ring of the track ball. Light intensity decreased and F-stop adjusted. The light intensity has been reduced and the F-stop has been adjusted. F-stop reduced image appearance similar to an octagonal ring as seen in Figure 5.1. If the edge of the ring is sharp, the sample is nominally in focus. Extended scanning mode was selected and measurement was taken with the smallest laser power.

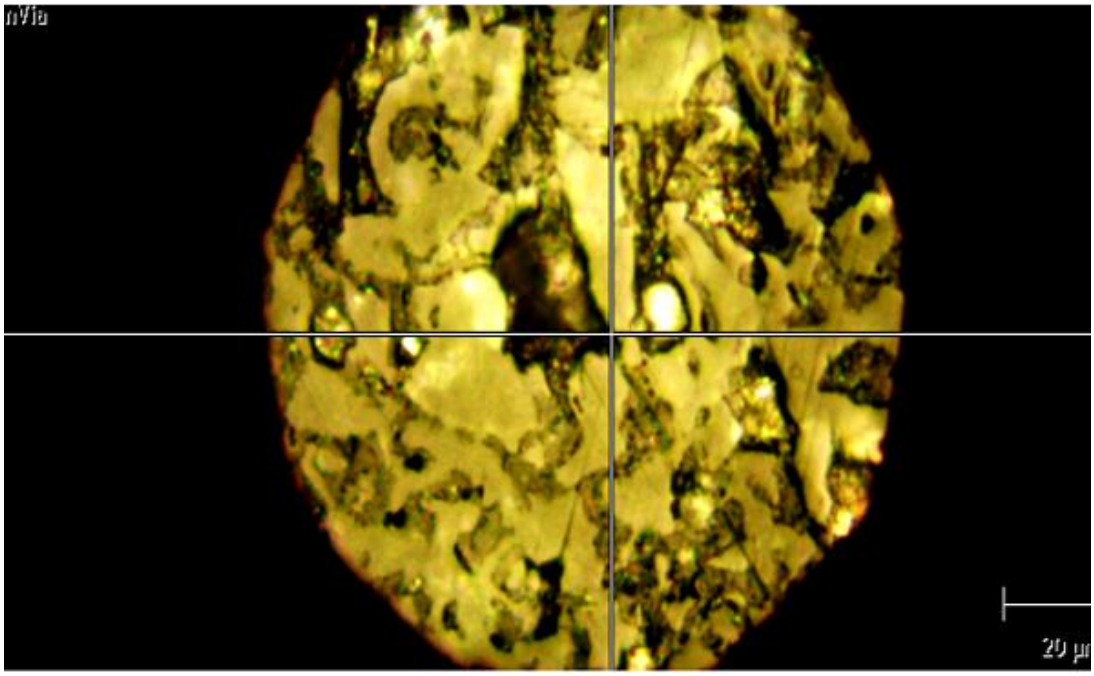

Figure 5.1 A representative image of the sample in focus for measurement.

5.2.1 Raman Spectroscopy Point Measurements

Raman measurements were collected from five different regions that can be distinguishable under the microscope. Raman measurements were first taken with an

extended scan. As seen in the Figure 5.2, the full spectrum range of 100-3200 cm^{-1} was chosen. No Raman peak was observed above 1200 cm^{-1} and therefore the scanning range was chosen between 100-1200 cm^{-1} .

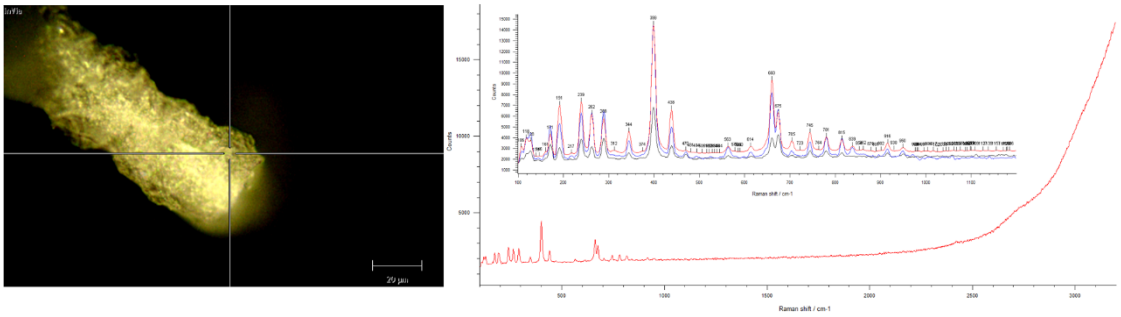

Figure 5.2 Optimization of the extended scan region for the data acquisition.

In order to ensure the right plane focus on the sample, checked the 'video with laser' option which is provide the overlap of laser focus point and the focused image simultaneously. Green laser spot should be in the center of the cross hairs and should be round shape not distorted or scattered. We have start to collection the measurement with Start with as minimum laser power as possible and gradually increase such as 0.05, 0.5, 1, 5 % laser power etc. If the high laser power intensity was chosen, this might cause saturation and induces wider surface on the sample as seen in the Figure 5.3.

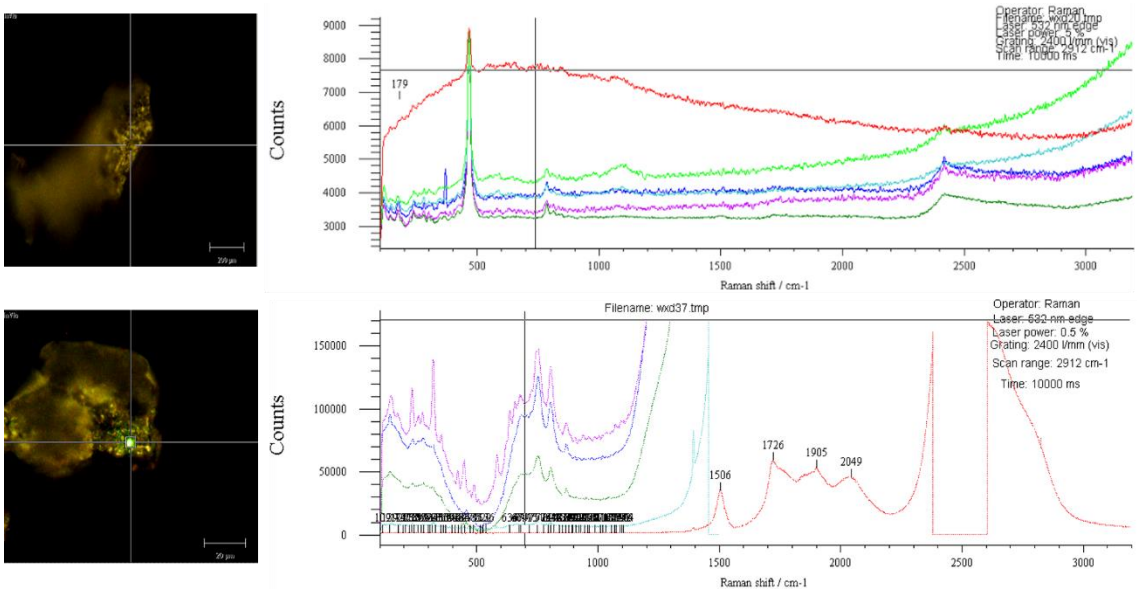

Figure 5.3 Representative spectrum images shows the laser intensity effect on the measurement collection.

A representative data set was obtained by measuring at 5 different locations on the sample. These datasets were compared with reference spectra to see if they were representative of the sample analyzed.

5.2.2 Raman Spectroscopy Map Measurements

Micro-Raman mapping is a powerful technique to visualize the spatial distribution and spectral information of polycrystalline strontium aluminate compounds synthesized with different glass-forming oxides. Raman mapping dataset was collected from a well-polished sintered pellet. Prior to the Raman mapping measurement, it is necessary to collect the reference spectra of each phase in the compounds. According to the Raman point analysis performed on 5 different regions of the sample, the multi-phase region was selected for mapping to analyze the distribution of crystalline and amorphous components Figure 5.4.

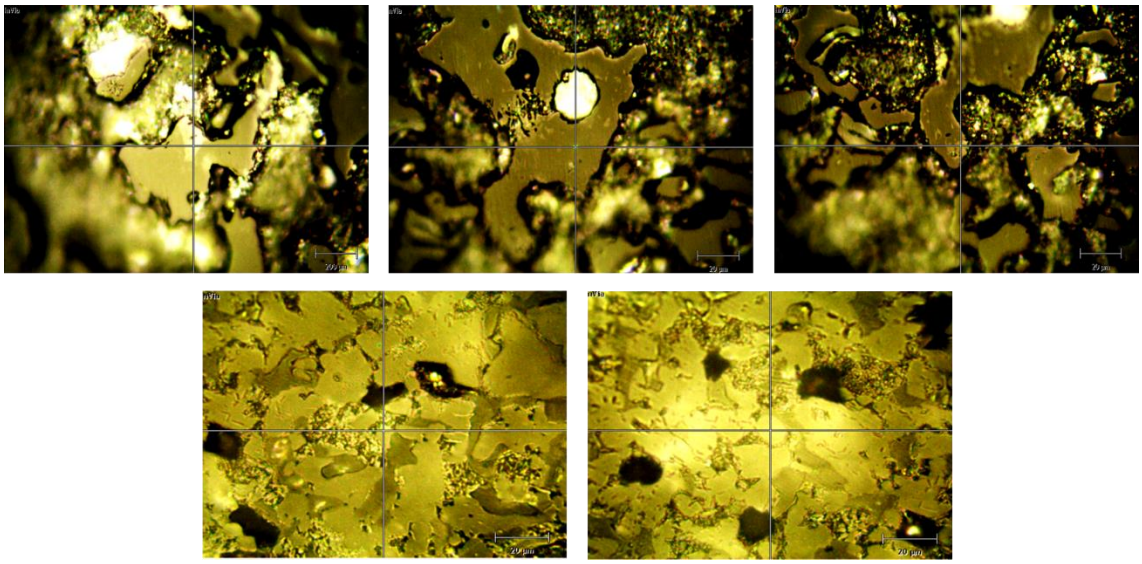

Figure 5.4 A representative region of interest for Raman mapping area selection on the sintered pellet sample.

Raman map data collection steps are shown in Figure 5.5. Choosing the appropriate step size for Raman map data collection is a challenging procedure that can affect the collected result. If the analyzed sample contains a particle size around 1 μm, then selection use 0.5 μm steps would give the best results. Consider that it is generally recommended to have 2 data points per resolution element. If you suspect the N.A. limited spatial resolution is 1.3 μm, data point spacing between 0.5 μm and 0.7 μm will likely create the best map. However, if the analyzed material has a grain size of 10 μm, anything smaller than 2 μm would not make sense unless the aim is trying to study the interface between particles. The consistency between step and laser focus spot size crucial consideration for the map data acquisition.

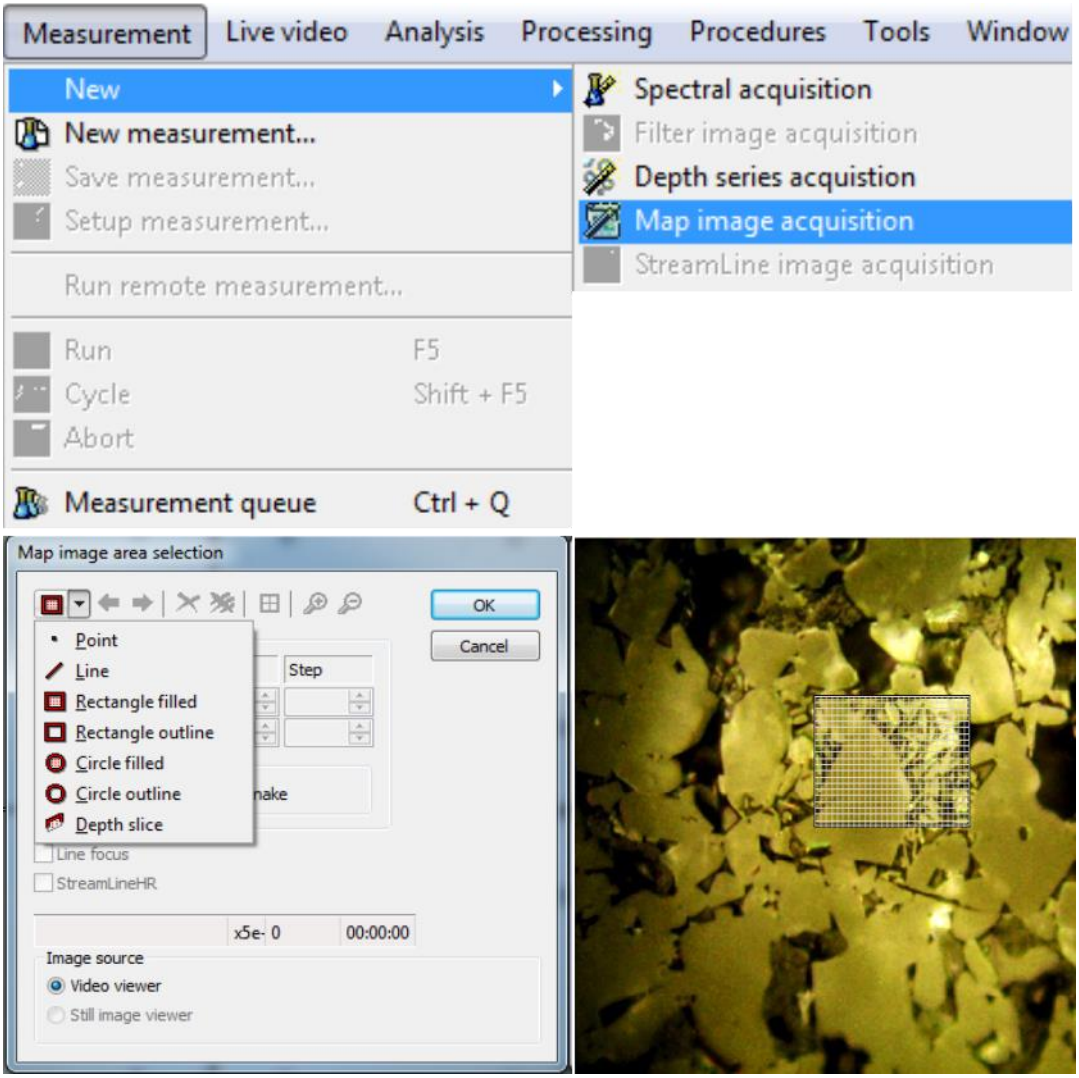

Figure 5.5 Raman Mapping procedure.

Laser focus spot size can be approximated by using the airy disk formula ($d = 1.22 \lambda / NA$) where the wavelength of the light λ and numerical aperture of the objective lens is used [108] .The laser spot size is estimated at 865 nm for a 50× microscope objective lens with a numerical aperture of 0.75. However, it should keep in consideration that spatial resolution is also affected by the entrance slit size and the number of CCD pixels being used.

The area size and the speed of the measurement are other considerations for the successful Raman mapping. If the larger map area were chosen for the map region with a way to smaller step size, the measurement would take more than 15 hours.

5.3 Chemometric Method

Hyperspectral Raman imaging provides three dimensional experimental dataset that contain both spectral (λ or ν) and spatial (*x* and *y*) information of components within heterogeneous samples [107]. Analysis of the Raman map dataset can be done by univariate methods or multivariate methods. One of the common univariate methods used for generating the chemical maps from hyperspectral images is based on the intensity of a Raman band. However, this method may misrepresent the Raman map dataset when there are interference effects during data collection from sample roughness, loss of focus or background interference [107]. Chemometric methods are multivariate data analysis methods that can overcome these interference effects and allows a better representation of the hyperspectral Raman imaging dataset [109,110].

Multivariate methods uses mathematical and statistical methods for decomposition to the whole data set simultaneously to identify and analyze the chemical, molecular and structural information of the non- homogenous samples [107,109–111].One of the challenges of the application of these methods is to choose the correct methods to effectively extract the chemical information from the concerning sample. Wire 3.4 contains 3 multivariate methods to unfold the Raman map dataset to analyze including DCLS, PCA, and MCR-ALS.

5.3.1 Direct Classical Least Squares (DCLS)

This method can be used when reference spectra of the all components in the mixture are available.

$$D = CS^T + E$$

Eq (5.1)

Where D is the data matrix, C is the concentration matrix, S pure spectra matrix correspond the concentration and E is the residual matrix [110]. DCLS method uses the reference spectrum and creates an intensity map based on similarity. The similarity value range from 0 to 1 and the closer the match, the closer the value is to 1.

The presence of cosmic rays and background fluorescence in the sample and the reference spectrum will have a detrimental effect on the observed value. For this reason, pre-processing requires for the analysis. Figure 5.6 and 5.7 shows the DCLS study of component 1 (C1) contribution distribution in the map data.

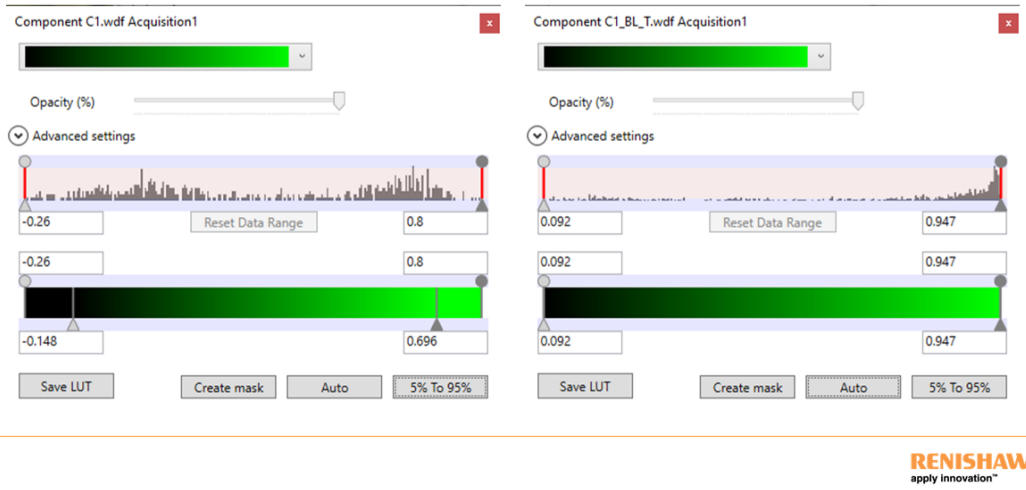

Figure 5.6 C1 contribution distribution without (left) and with pre-processing (right). (From discussion notes with Richard Bormett).

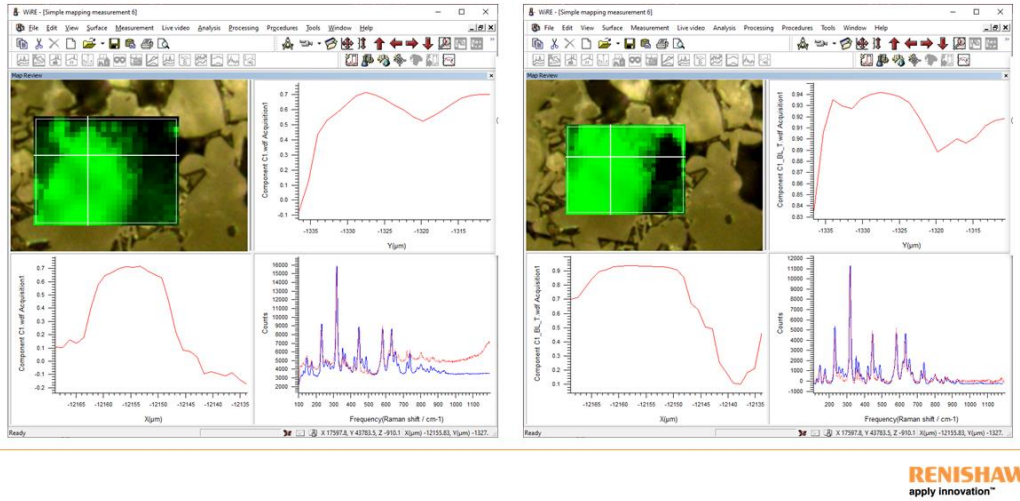

Figure 5.7 C1 contribution distribution without (left) and with pre-processing (right). (From discussion notes with Richard Bormett).

After the pre-processing of dataset, the best match to C1 and C2 showed in Figure 5.8 and 5.9.

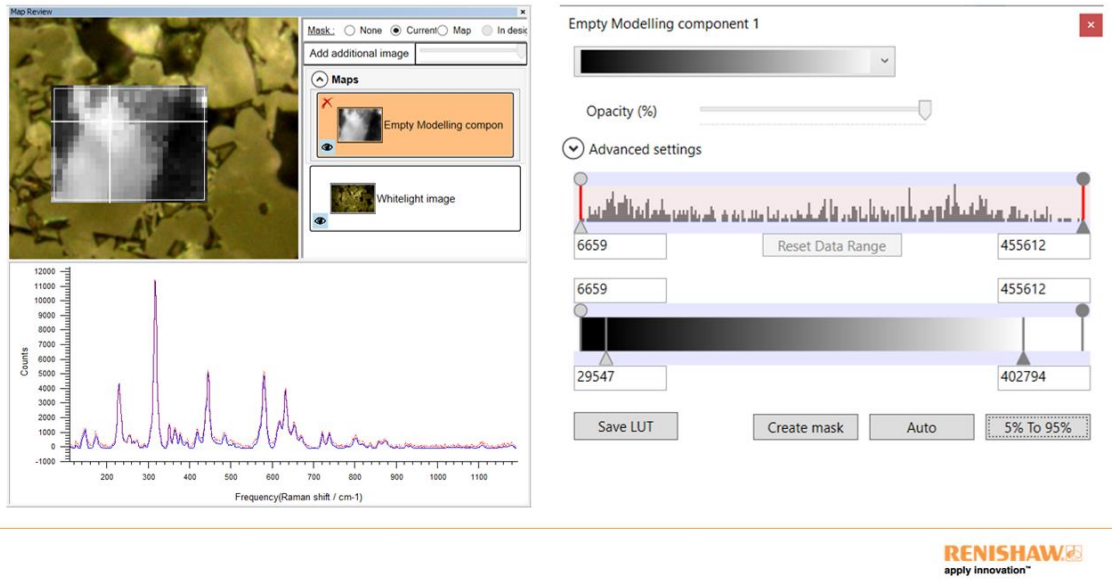

Figure 5.8 DCLS best match to C1. (From discussion notes with Richard Bormett).

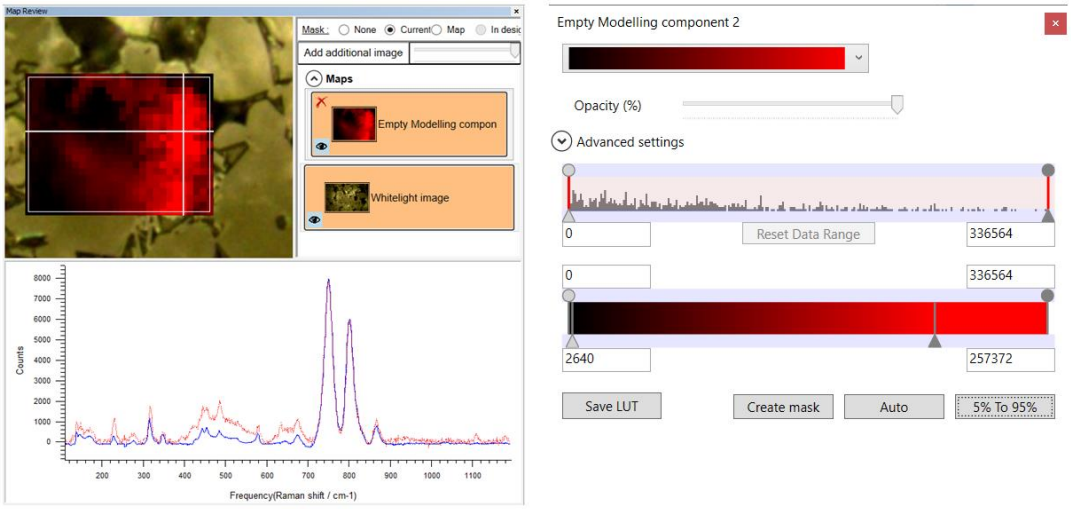

Figure 5.9 DCLS best match to C2. (From discussion notes with Richard Bormett).

5.3.2 Principal Component Analysis

This method reduces the amount of data matrix and generates a new set of variables, called principal components (PCs). The data decomposition is represented by;

$$D = TP^T + E$$

Eq (5.2)

Where D is initial data matrix, T is score matrix (concentration-like), P is loading matrix (spectrum-like) and E is residual matrix. PCA generates scores, which are distribution maps, and loadings, which are the spectra [112]. Interpretation of the PCA results can be challenging due to the uncorrelated scores and loading with real spectra of compounds. Fluorescence backgrounds can affect the data interpretation. Figure 5.10 is show how to fluorescence can influence the order of the principle components.

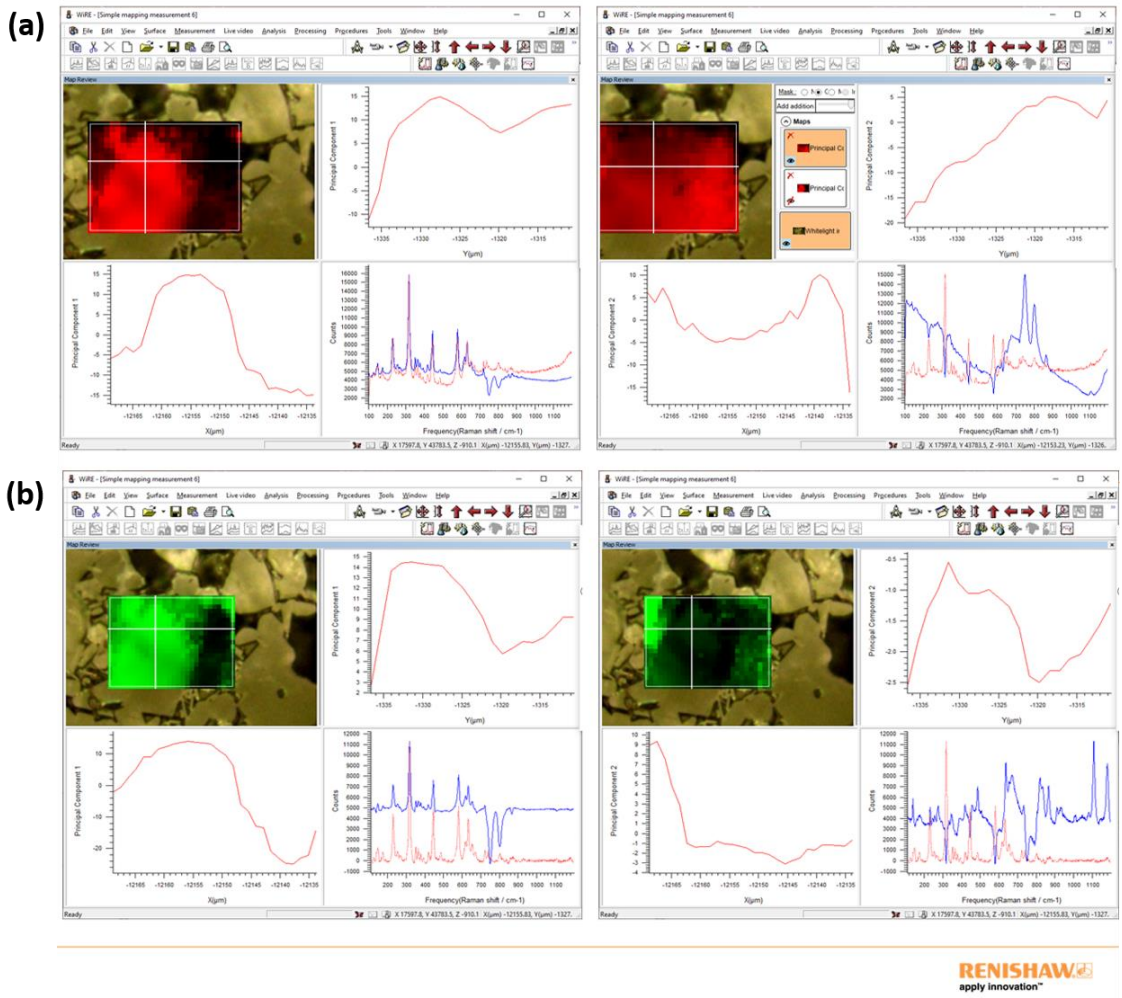

Figure 5.10 a) PCA C1 and C2 without pre-processing; b) PCA C1 and C2 with pre-processing. (From discussion notes with Richard Bormett).

5.3.3 Alternating Least Squares (MCR-ALS)

MCR –ALS method is used to collect pure spectral and contribution profiles of the components within the analyzed compounds.

$$D = CS^T + E$$

Eq (5.3)

where D is a matrix containing the spectra of all pixels of the image, S^T and C are matrices of the pure spectral signatures and the related distribution maps (concentration profiles) of the image constituents and E is a residual matrix [109,110,112].

After the Raman map data was collected, the data set to be analyzed with MCR-ALS was opened as shown in Figure 5.11.

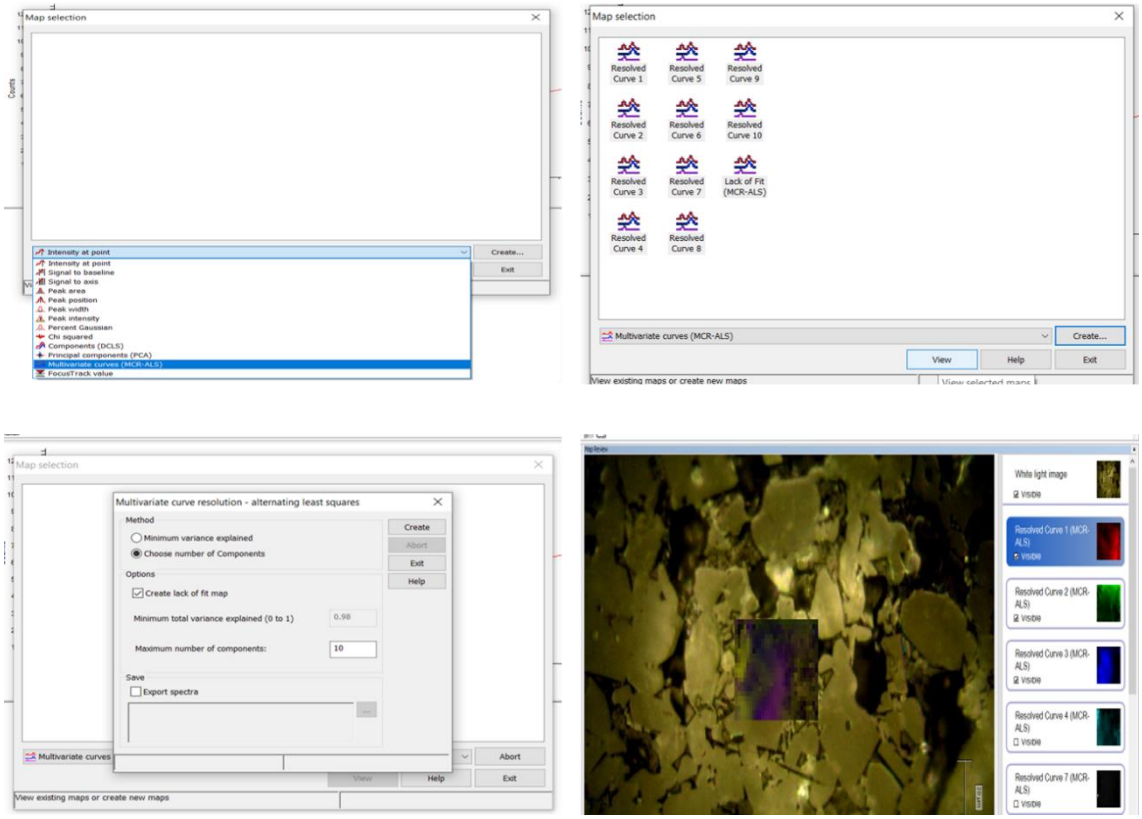

Figure 5.11 Map selection procedure for the MCR-ALS.

In order to determine the best chemometric method for our Raman dataset, we investigated the same dataset with PCA and MCR-ALS techniques. The comparison of spatial and spectral results from both techniques is shown in Figure 5.12. The difference in the distribution of complex phases was observed as seen in Figures 5.12 (a) and 5.12 (b) with color-coded scores.

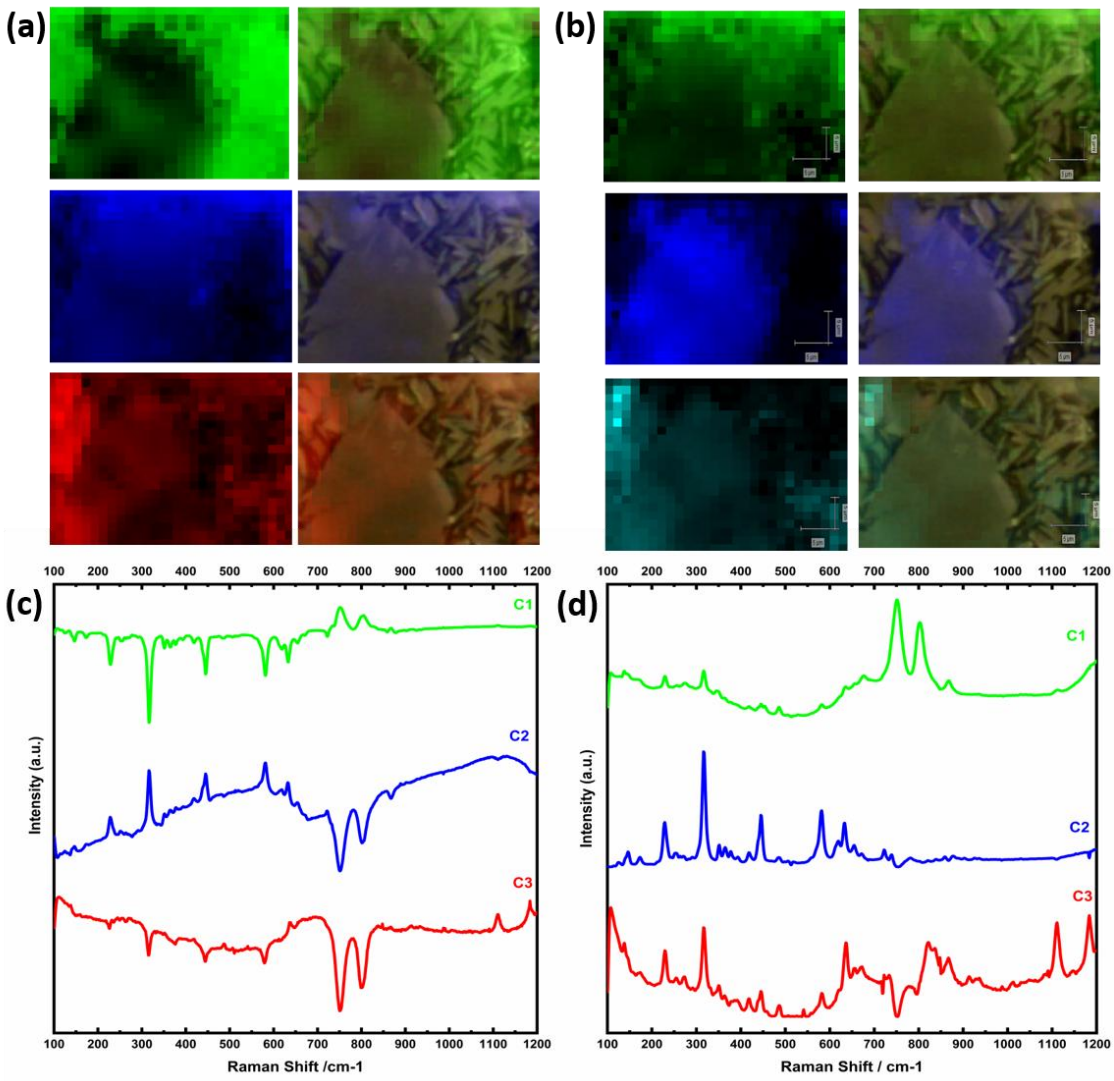

Figure 5.12 Comparison of PCA and MCR-ALS method for the S4A7ED 30 mo% B_2O_3.

The loadings obtained from the PCA are not recognizable as spectra, as these are abstract vectors and not constrained to be positive (Figure 5.12 (c)). MCR-ALS provides a decomposition of mixed experimental data into estimates of the chemically meaningful profiles of the respective chemical species (Figure 5.12 (d)).

MCR-ALS method was selected as a data processing method for the dataset collected from the multiphase strontium aluminate compounds.

5.3.4 Pre-processing for Raman Spectroscopy Data

5.3.4.1 Cosmic ray removal

Cosmic rays appear as dense random and sharp peaks in the spectrum (Figure 5.13). The result of the data analysis can be misleading if the cosmic rails were not removed as we observed in the Raman dataset. The cosmic ray in the spectrum can be removed by using the cosmic ray lift option in the toolbar.

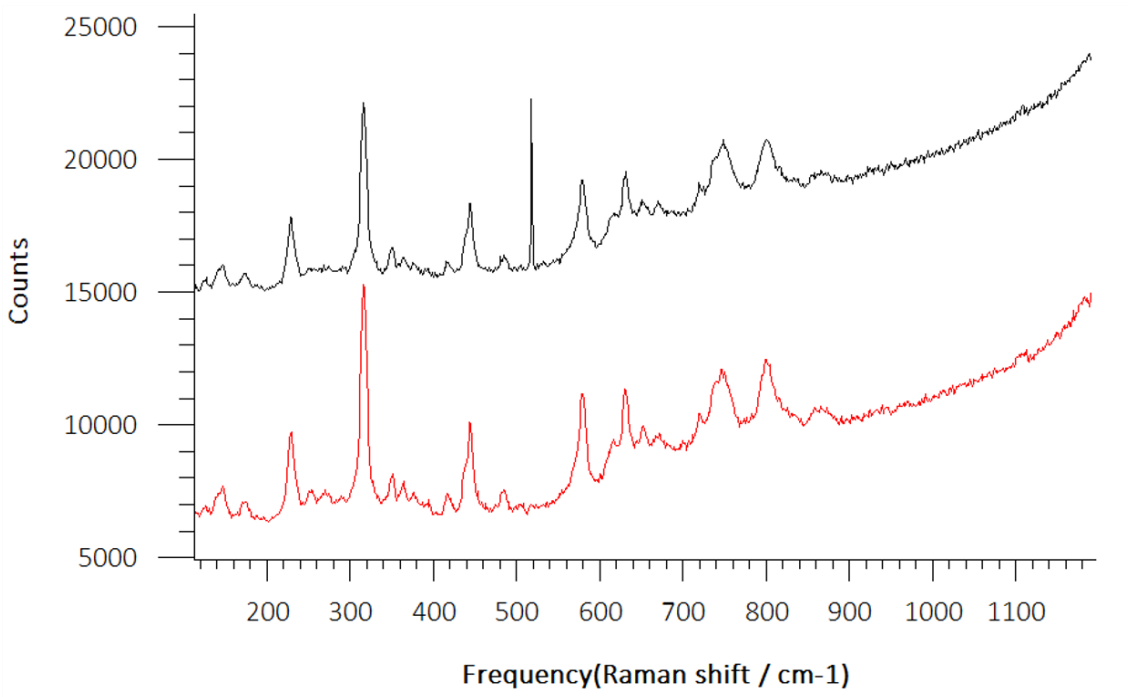

Figure 5.13 Cosmic Ray observed in spectrum.

5.3.4.2 Noise filtering

After the cosmic ray removal, noise filtering should be apply to PCA data set. Noise filtering analyses the spectral features for whether they represent the noise or actual loading that has spectral information. The application of the noise filter for the PCA dataset is shown in Figure 5.14.

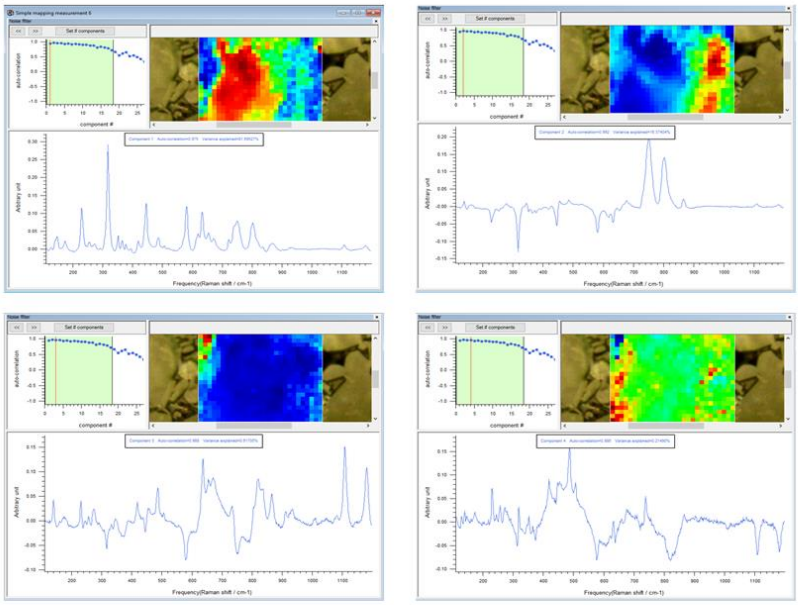

Figure 5.14 Noise filter application to PCA dataset for 4 components that appeared in the dataset.

5.3.4.3 Truncate Rayleigh edge cut-off artifact

The spectral window includes low frequency data that is beyond the transmission window of the Raleigh filter should be removed.

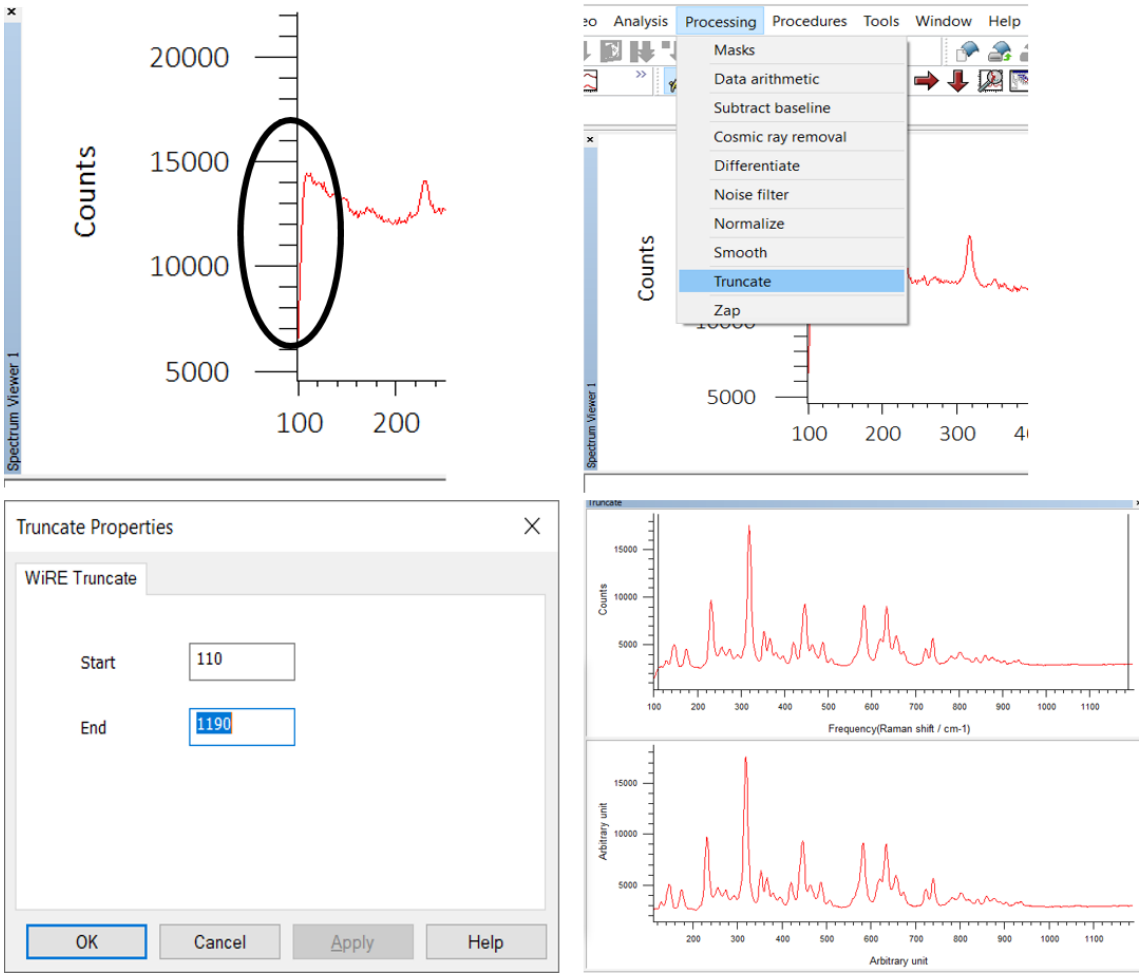

Figure 5.15 Truncate process for collected Raman spectra.

5.3.4.4 Baseline Correction and Smoothing

Baseline subtraction can be applied to remove the nonlinear background. Wire 3.4 offers the baseline subtraction option on the toolbar. It is important to note that, observed the change in the collected spectrum should be examined carefully whether it is due to background or overlapping Raman bands. For this purpose, a couple of measurements should be first collected and compared with previous results and then decided to subtract the baseline.

Smoothing can be applied if the collected spectrum to noisy and this option is provided in the Wire 3.4 software by the Savitzky-Golay algorithm. During the smoothing weak Raman signals can vanish, so should be careful to apply.

5.4 Investigation the Strontium Aluminate Compounds with FTIR Spectroscopy

In previous studies, FTIR spectroscopy techniques have proved useful in determining the structure and local environment of glassy systems. Although the glasses do not have a long-range structural order, they still have a short-range order in their atomic arrangements. Nag demonstrated the existence of BO_4 units in SA by using FTIR and NMR techniques [2]. We systematically studied the 4 major phases of strontium aluminate to trace the dopant-induced structural changes and the presence of short-range order units in compounds.

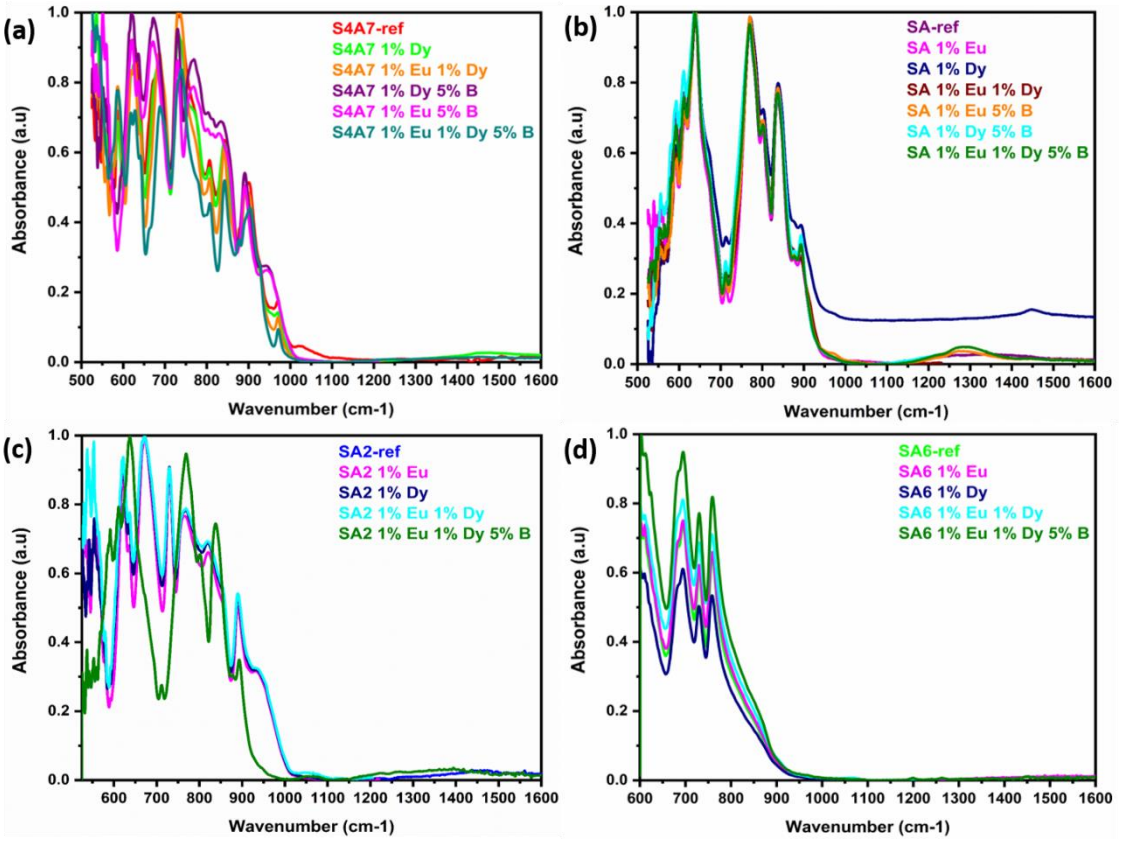

Figure 5.16 FTIR spectra summary for strontium aluminate phases doped with only Eu, Dy and B.

Eu, Dy, and B-doped strontium aluminate compounds synthesized by the Pechini process as described in Chapter 2, were investigated by FTIR spectroscopy to elucidate that dopants induced structural changes in the crystal structure. SA and S4A7 phases have been studied by FTIR in the literature, but as far as we know, we have not come across a study about SA2 and SA6 phases. The region 500-1000 cm^{-1} showed vibrations related to the alumina scaffold of the strontium aluminate crystal structures in Figure 5.16. In this region, the characteristic vibrations of O-Al-O were observed in the phase-pure, undoped SA,S4A7, SA2 and SA6 reference spectra .Absorption bands were observed for Al-O features, both anti-symmetric stretching (700-1000 cm^{-1} region) and anti-symmetric bending (550-650 cm^{-1}). However broad overlap FTIR bands did not reveal much information of the each spectrum of doped strontium aluminate compounds.

5.5 Investigation the Strontium Aluminate Compounds with Micro-Raman Spectroscopy

The Raman modes of $SrAl_2O_4$ (SA) have also been considered in several studies [22–24]. Meanwhile, crystal structure changes due to dopant and impurity incorporation have been studied with Raman spectroscopy [25]. Figure 17 is shown the systemic investigation of Eu, Dy and B doped strontium aluminate compounds.

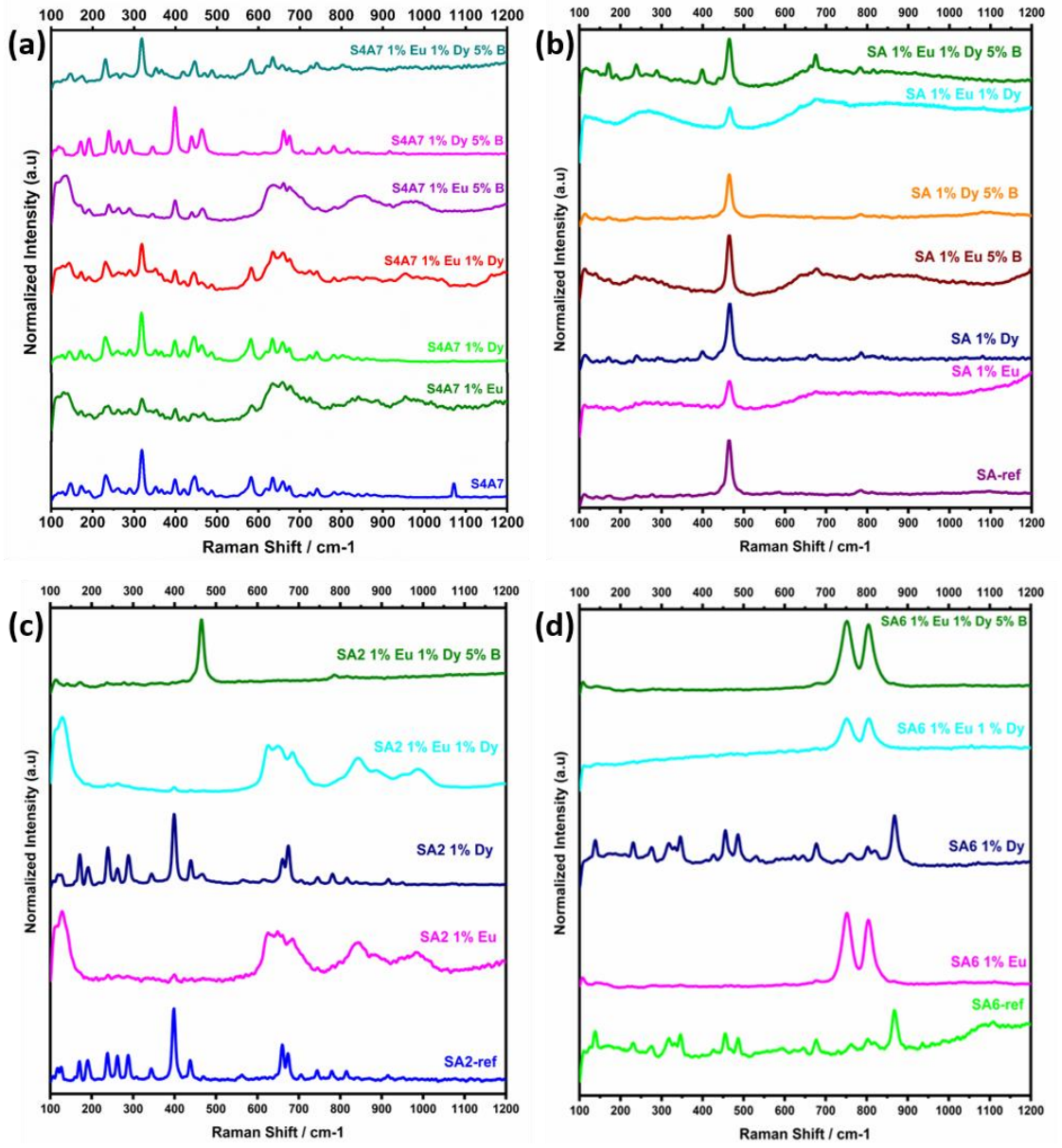

Figure 5.17 Raman spectra summary for strontium aluminate phases doped with only Eu, Dy and B.

Unlike the FTIR spectra, Raman spectra of each compounds revealed the changes in phonon vibrations of crystals structures. Figure 5.17 shows the effect of individual rare earth dopants on the each strontium aluminate crystalline phases. The general trend that observed was; unit cell doped with only Eu exhibited distortion in the Raman shift, while

doping with only Dy didn't generate such a distortion. This observation can be attributed to the difference in size between Eu and Dy ions, the latter of which, being larger, is more prone to segregating out of the grain above the solubility limit [4]. This might be the reason of doped only with Dy exhibited similar Raman spectra with the non-doped sample. Eu, Dy, and B doped SA2 and SA6 compounds showed more differences in high intensity and narrow band spectra compared to reference spectra.

Reference spectra of each phase collected to be as guideline to interpret the data from multiphase compounds. Figure 5.18 is shown the Raman spectra of S4A7ED 30 mol% TEOS. XRD Rietveld phase fraction analysis reveals the equal distribution of the SA, SA2 and S4A7 phases, which is similar to what we observed from Raman spectra. Trace of all three phases appears in the Raman spectra of S4A7ED 30 mol% TEOS. Comparing the doped compounds with the reference compounds enabled us to distinguish the Raman bands in the compounds and made it easier for us to distinguish the new bands that appeared only because of the SiO_4 units from the others.

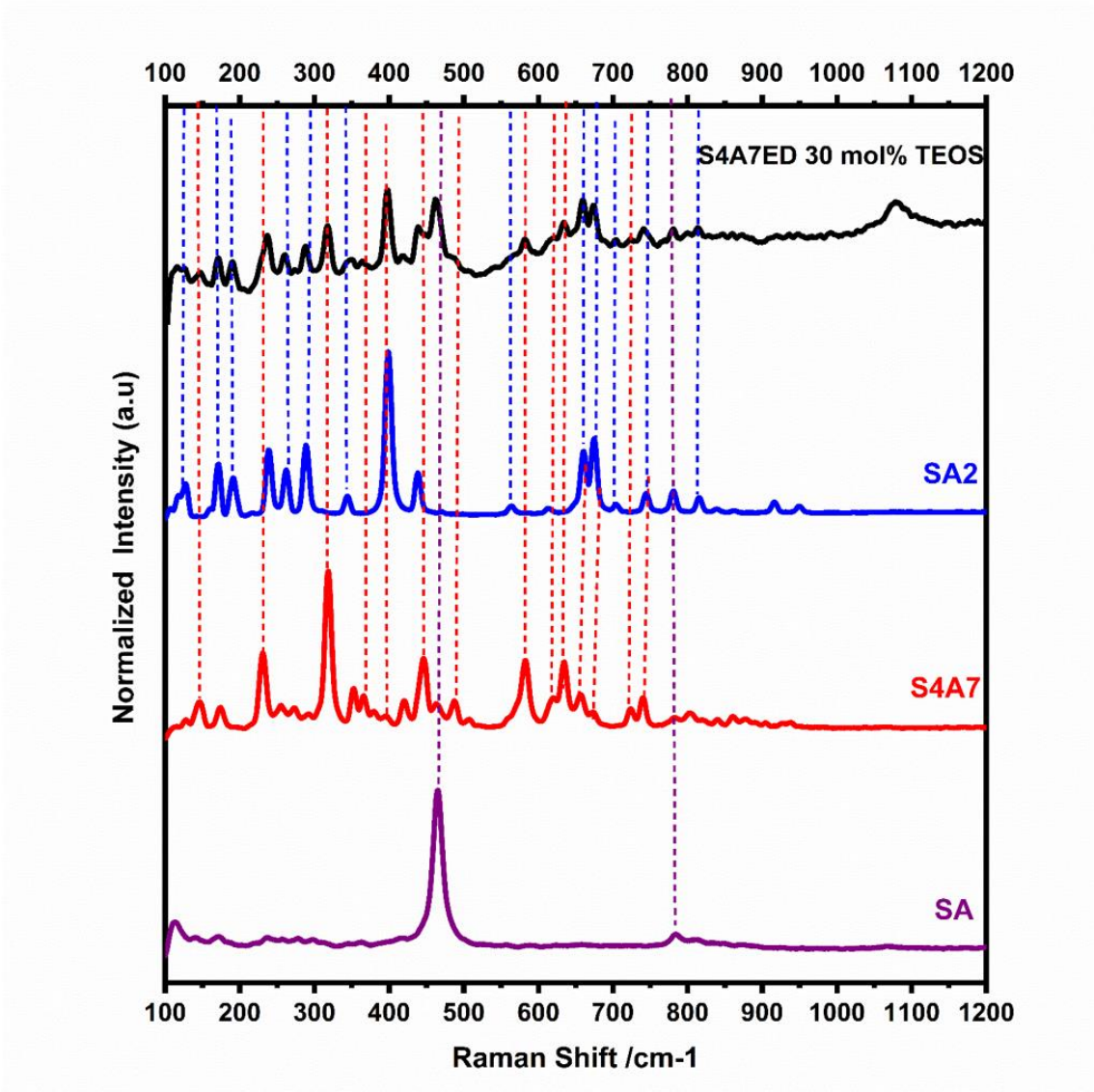

Figure 5.18 Raman spectra of the S4A7ED 30 mol% TEOS with reference spectra.

To summarize the Raman and FTIR spectra had showed the characteristic vibrations of boron units, but offered deeper insight into the glassy suprastructures. FTIR revealed the presence of BO_3 and BO_4 units but Micro-Raman analysis of S4A7EDxB grains revealed the presence of borate supramolecular structures in their orthorhombic $Sr_4Al_{14}O_{25}$ crystal structure as $B\emptyset_3$, $B\emptyset_2O^-$, and $B\emptyset_4^-$ units. Chapter 3 Raman spectroscopy offers sub-micrometer spatial resolution compared to FTIR spectroscopy. Both techniques has instrumental and technical limitations.

5.6 Developing of the MCR-ALS Analysis Software

As described in the above section, to improve the spectrum results that we obtain from MCR-ALS for the current Wire 3.4 version that we have, some pre-processing methods has to apply. However, Wire3.4 has limitations for the pre-processing options. Ahmet Alper Özkan has developed a software for the MCR-ALS data set analysis.

Alper developed a software with three preprocessing options such as Savitzky-Golay filtering to smooth regularly occurring noise [113], asymmetric least squares baseline removal to fix the curves on the horizontal axis [114] and PCA to remove cosmic rays [115] Figure 5.19.

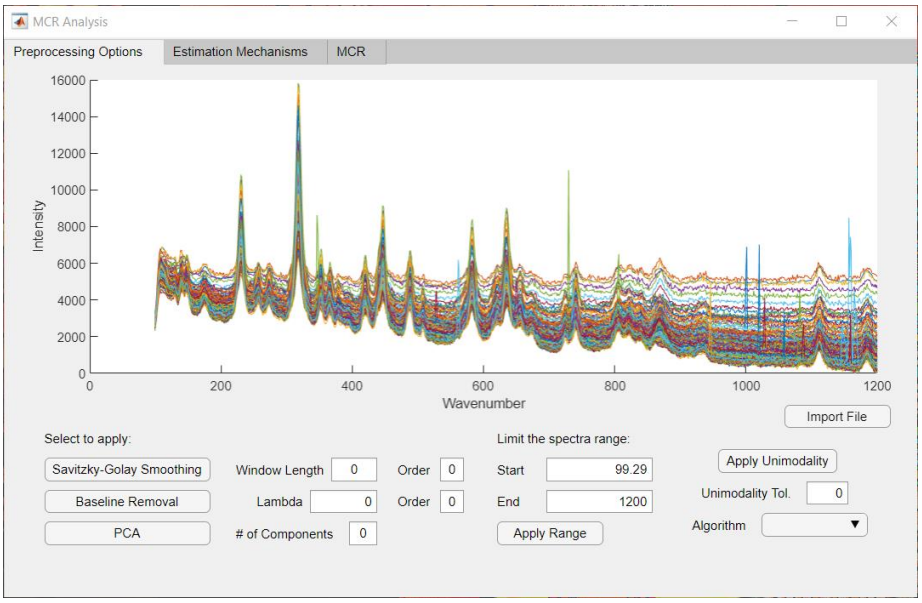

Figure 5.19 Preprocessing tab of the graphical user interface with a sample dataset. (From Ahmet Alper Özkan graduation Project).

The software named as MCR_Analysis, provides spectrum range limitation options in addition to eliminate the cosmic ray peaks and low intensity noise components options. The software uses EFA and SIMPLISMA as an estimation tab. SIMPLISMA outputs provides more similar pure components Figure 5.20. The heat map image is shown in

Figure 5.21, has similar color-coded spectrum of the C1 components that observed in Wire 3.4 MCR-ALS processing.

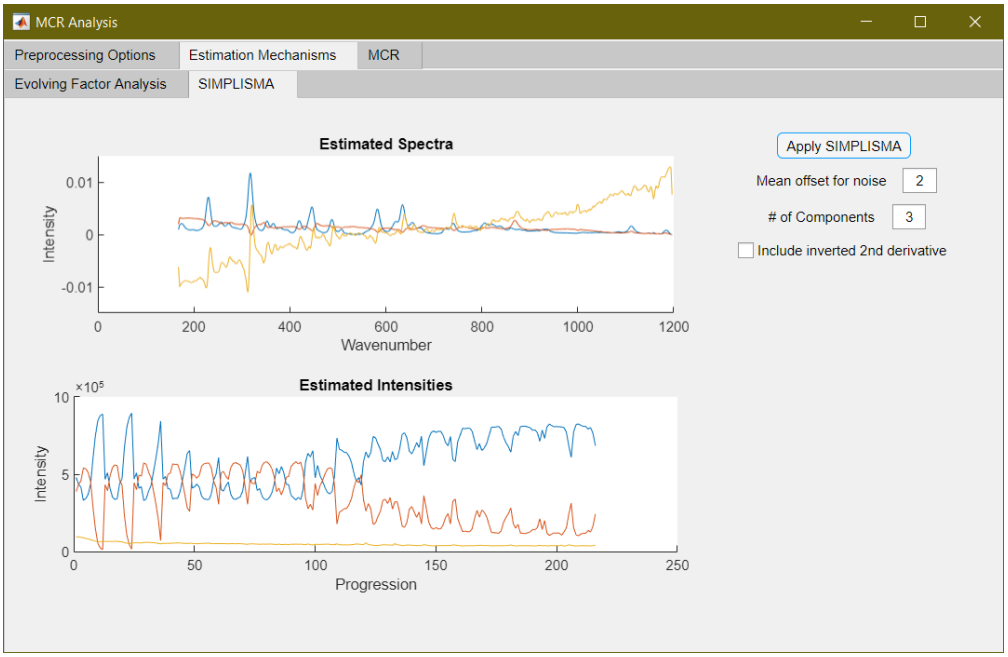

Figure 5.20 SIMPLISMA subtab of the Estimation Mechanisms (From Ahmet Alper Özkan graduation Project).

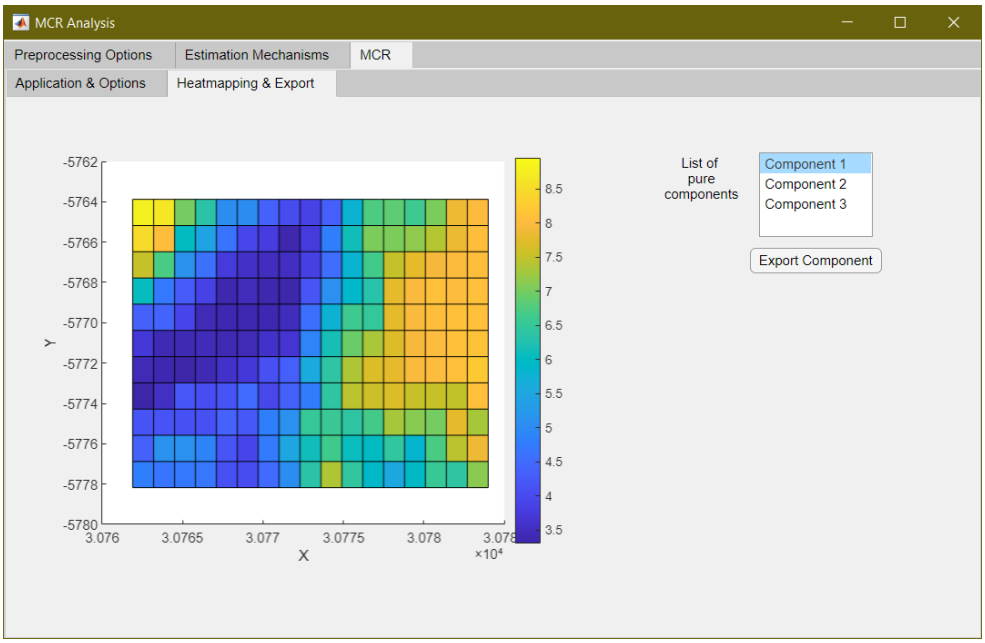

Figure 5.21 Heat mapping window with the 1st component displayed (From Ahmet Alper Özkan graduation Project).

CHAPTER 6: SUMMARY AND FUTURE WORK

The objective of this dissertation is to understand how certain oxide glass forming cations induce the clustering of divalent Eu and trivalent Dy in strontium aluminate compounds which was manifested as PersiL. To elucidate the atomic arrangements in such compounds, we applied materials characterization tools that reveal information about short-range order and localized environments, FTIR, and Raman spectroscopy.

In chapter 3, the longest duration of persistent luminescence in Eu and Dy co-doped strontium aluminate (S4A7ED) was observed on 30-40 mol% B_2O_3 (S4A7EDB). This composition does not contain the highest amount of long persistence phase. The crystal environment of B in S4A7ED was evaluated by using Raman and FTIR spectroscopy. Polyatomic vibration modes containing B-O were revealed, in the form of metaborate and orthoborate. Based on these results, we proposed a structural model for S4A7EDB, in which B introduces non-bridging oxygen, which offers excess negative charge and enlarged adjacent Sr sites, both of which enable Eu and Dy dopant clustering that yields extreme persistent luminescence.

In chapter 4, we investigated the correlation between other oxide glass forming cations—Si, P, Zr, and V—and their capability for extending PersiL in S4A7ED. To understand the structural changes that these cations impart to the atomic arrangements inside the S4A7ED crystal structure, we used FTIR and micro-Raman spectroscopy and evaluated the impact of charged NBOs. Our results demonstrated that the use of oxide glass forming precursors of Si, P, and Zr during Pechini processing also extended PersiL in S4A7ED compounds and was correlated with structural changes arising from NBO incorporation. We also observed the persistent luminescence behavior at room temperature for the

strontium aluminate compounds dominated by SA2 phases, which were synthesized with H_3PO_4.

In Chapter 5, data collection, interpretation, and challenges encountered using FTIR and Micro-Raman Spectroscopy in multiphase strontium aluminate compounds were described in detail. Reference spectra of each strontium aluminate phase enlightened the investigation of the multiphase phase doped strontium aluminate compounds. Choosing the right chemometric methods, analyzing the Raman map dataset and the importance of preprocessing techniques are critical in extracting information from the huge dataset. It is important to note that the use of micro-Raman spectroscopy is essential for our ceramic powders. Because this technique offers spatial resolution and phase identification potential at a dimensional scale. Complementary FTIR spectroscopy revealed the presence of inactive Raman vibration.

It is important to highlight that the use of micro-Raman analysis was essential to these results, because the signal-to-noise was superior to that in FTIR and because the micron-scale spatial resolution was achieved, enabling the well-defined analysis of grains larger than a micron.

The culmination of the systematic study of the structure of PersiL strontium aluminate compounds gave us insight into the design rule of persistence of luminescence compounds. Our key results have revealed that the incorporation of electrically charged, non-bridging oxygen (NBO) species into the doped $Sr_4Al_{14}O_{25}$ (S4A7ED) crystal structure induces the clustering of divalent Eu and trivalent Dy, which is manifested as PersiL. The non-zero ratio of the BO to NBO is essential to designing the strontium aluminate compounds with persistent luminescence. Regarding future work, the optimization of the synthesis conditions and stoichiometric ratio of different glass-forming oxides can enhance the afterglow duration of strontium aluminates which was not reported as room temperature PersiL such as SA2 compounds.

REFERENCES

[1] Chen IC, Chen TM. Sol-gel synthesis and the effect of boron addition on the phosphorescent properties of $SrAl_2O_4:Eu^{2+}$, Dy^{3+} phosphors. J Mater Res 2001;16:644–51. https://doi.org/10.1557/JMR.2001.0122.

[2] Nag A, Kutty TRN. Role of B_2O_3 on the phase stability and long phosphorescence of $SrAl_2O_4$:Eu,Dy. J Alloys Compd 2003;354:221–31. https://doi.org/https://doi.org/10.1016/s0925-8388(03)00009-4.

[3] Inan Akmehmet G, Šturm S, Bocher L, Kociak M, Ambrožič B, Ow-Yang CW. Structure and Luminescence in Long Persistence Eu, Dy, and B Codoped Strontium Aluminate Phosphors: The Boron Effect. J Am Ceram Soc 2016;99:2175–80. https://doi.org/10.1111/jace.14188.

[4] Khabbaz Abkenar S, Kocjan A, Samardžija Z, Fanetti M, Coşgun Ergene A, Šturm S, et al. Effect of sintering and boron content on rare earth dopant distribution in long afterglow strontium aluminate. J Eur Ceram Soc 2020;40:4129–39. https://doi.org/10.1016/j.jeurceramsoc.2020.04.048.

[5] Nag A, Kutty TRN. The mechanism of long phosphorescence of $SrAl_{2-x}B_xO_4$ ($0 < x < 0.2$) and $Sr_4Al_{14-x}B_xO_{25}$ ($0.1 < x < 0.4$) co-doped with Eu^{2+} and Dy^{3+}. Mater Res Bull 2004;39:331–42. https://doi.org/10.1016/j.materresbull.2003.11.007.

[6] Shelby JE. Introduction to Glass Science and Technology. 2nd ed. Royal Society of Chemistry, 1997; 2007. https://doi.org/10.1039/9781847551160-00072.

[7] Wright AC. My Borate Life: An Enigmatic Journey. Int J Appl Glas Sci 2015;6:45–63. https://doi.org/10.1111/ijag.12113.

[8] Scholze H. Glass: nature, structure, and properties. 1st ed. Springer, New York,; 1992. https://doi.org/10.5860/choice.29-2717.

[9] Chiang Y-M, Birnie DP, Kingery WD. Physical Ceramics: Principles for Ceramic Science and Engineering. Wiley; 1996.

[10] Meera BN, Ramakrishna J. Raman spectral studies of borate glasses. J Non Cryst Solids 1993;159:1–21. https://doi.org/10.1016/0022-3093(93)91277-A.

[11] Bunker BC, Kirkpatrick RJ, Brow RK, Turner GL, Nelson C. Local Structure of Alkaline-Earth Boroaluminate Crystals and Glasses: II, 11B and 27Al MAS NMR Spectroscopy of Alkaline-Earth Boroaluminate Glasses. J Am Ceram Soc 1991;74:1430–8. https://doi.org/10.1111/j.1151-2916.1991.tb04124.x.

[12] Osipov AA, Eremyashev VE, Mazur AS, Tolstoi PM, Osipova LM. Coordination state of aluminum and boron in barium aluminoborate glass. Glas Phys Chem 2016;42:230–7. https://doi.org/10.1134/S1087659616030111.

[13] Yiannopoulos YD, Chryssikos GD, Kamitsos EI. Structure and properties of alkaline earth borate glasses. Phys Chem Glas 2001;42:164–72.

[14] Kyômen T, Motani R, Hanaya M. Effect of B_2O_3 or SiO_2 Fluxes on morphology and size of pr-doped $CaTiO_3$ phosphor particles and on their photoluminescence properties. Key Eng Mater 2012;497:31–7. https://doi.org/10.4028/www.scientific.net/KEM.497.31.

[15] Yu YT, Kim BG. Effects of adding B_2O_3 as a flux on phosphorescent properties in synthesis of $SrAl_2O_4$: (Eu^{2+}, Dy^{3+}) phosphor. Korean J Chem Eng 2003;20:973–6. https://doi.org/10.1007/BF02697308.

[16] Venkatesan A, Krishna Chandar NR, Kandasamy A, Karl Chinnu M, Marimuthu KN, Mohan Kumar R, et al. Luminescence and electrochemical properties of rare earth (Gd, Nd) doped V_2O_5 nanostructures synthesized by a non-aqueous sol-gel route. RSC Adv 2015;5:21778–85. https://doi.org/10.1039/c4ra14542a.

[17] Du P, Li S, Wang X, Zhu Q, Li JG. On the role of Zr substitution in structure modification and photoluminescence of $Li_{5+2x}La_3(Ta_{1-x}Zr_x)_2O_{12}$:Eu garnet phosphors. Dalt Trans 2021;50:3337–47. https://doi.org/10.1039/d0dt04245e.

[18] Fernández-Rodríguez L, Durán A, Pascual MJ. Silicate-based persistent phosphors. Open Ceram 2021;7:100150. https://doi.org/10.1016/j.oceram.2021.100150.

[19] Verma BR, Baghel RN. A Review on Luminescence properties in Eu Doped Phosphate Phosphors. Int J Mater Sci 2017;12:483–9.

[20] Furuya S, Nakano H, Yokoyama N, Banno H, Fukuda K. Enhancement of photoluminescence intensity and structural change by doping of P5+ ion for Ca2−x/2(Si1−xPx)O4:Eu2+ green phosphor. J Alloys Compd 2016;658:147–51. https://doi.org/https://doi.org/10.1016/j.jallcom.2015.10.172.

[21] Musgraves JD, Hu J, Calvez L. Handbook of Glass. Springer International Publishing,Switzerland; 2019. https://doi.org/10.1007/978-3-319-93728-1_50.

[22] Escribano P, Marchal M, Luisa Sanjuán M, Alonso-Gutiérrez P, Julián B, Cordoncillo E. Low-temperature synthesis of $SrAl_2O_4$ by a modified sol-gel route: XRD and Raman characterization. J Solid State Chem 2005;178:1978–87. https://doi.org/10.1016/j.jssc.2005.04.001.

[23] Dias A, Moreira RL. Polarization-resolved Raman modes of monoclinic $SrAl_2O_4$ ceramics. J Raman Spectrosc 2018;49:1514–21. https://doi.org/10.1002/jrs.5405.

[24] Rojas-Hernandez RE, Rubio-Marcos F, Gonçalves RH, Rodriguez MÁ, Véron E,

Allix M, et al. Original Synthetic Route to Obtain a $SrAl_2O_4$ Phosphor by the Molten Salt Method: Insights into the Reaction Mechanism and Enhancement of the Persistent Luminescence. Inorg Chem 2015;54:9896–907. https://doi.org/10.1021/acs.inorgchem.5b01656.

[25] Tuschel D. Effect of dopants or impurities on the raman spectrum of the host crystal. Spectroscopy 2017;32:13–9.

[26] Schmid T, Schäfer N, Levcenko S, Rissom T, Abou-Ras D. Orientation-distribution mapping of polycrystalline materials by Raman microspectroscopy. Sci Rep 2015;5:1–7. https://doi.org/10.1038/srep18410.

[27] Partyka J, Leśniak M. Raman and infrared spectroscopy study on structure and microstructure of glass-ceramic materials from SiO_2-Al_2O_3-Na_2O-K_2O-CaO system modified by variable molar ratio of SiO_2/Al_2O. Spectrochim Acta - Part A Mol Biomol Spectrosc 2016;152:82–91. https://doi.org/10.1016/j.saa.2015.07.045.

[28] Efimov AM. Vibrational spectra, related properties, and structure of inorganic glasses. J Non Cryst Solids 1999;253:95–118. https://doi.org/10.1016/S0022-3093(99)00409-3.

[29] Hu G, Zhou Y, Liu R, Li C, Liu L, Lin H, et al. Regulation of luminescence properties of SBGNA:Eu^{3+} glass by the content of B_2O_3 and Al_2O_3. Opt Mater (Amst) 2020;106:110025. https://doi.org/10.1016/j.optmat.2020.110025.

[30] Jiao Q, Yu X, Xu X, Zhou D, Qiu J. Relationship between Eu^{3+} reduction and glass polymeric structure in Al_2O_3-modified borate glasses under air atmosphere. J Solid State Chem 2013;202:65–9. https://doi.org/10.1016/j.jssc.2013.03.005.

[31] Gautam C, Yadav AK, Singh AK. A Review on Infrared Spectroscopy of Borate Glasses with Effects of Different Additives. ISRN Ceram 2012;2012:1–17. https://doi.org/10.5402/2012/428497.

[32] Redkov A V., Lipovskii AA, Tagantsev DK, Groth B. Micro-Raman Spectroscopy Study of Glass-Ceramics with Gradient of Volume Fraction of Crystalline Phase. J Am Ceram Soc 2016;99:2558–60. https://doi.org/10.1111/jace.14368.

[33] Douy A, Capron M. Crystallisation of spray-dried amorphous precursors in the SrO-Al2O3 system: A DSC study. J Eur Ceram Soc 2003;23:2075–81. https://doi.org/10.1016/S0955-2219(03)00015-3.

[34] Bruker-AXS. DIFFRACPlus TOPAS: TOPAS 4.2 Technical Reference. 2008.

[35] Inorganic Crystal Structure Database. FIZ Karlsruhe Karlsruhe, Ger 2019. https://www.fiz-karlsruhe.de/de/produkte-und-dienstleistungen/inorganic-crystal-structure-database-icsd.html, [FIZ Karlsruhe: Karlsruhe, Germany, 2019].

[36] Momma K, Izumi F. VESTA 3 for three-dimensional visualization of crystal, volumetric and morphology data. J Appl Crystallogr 2011;44:1272–6. https://doi.org/10.1107/S0021889811038970.

[37] Meier RJ. On art and science in curve-fitting vibrational spectra. Vib Spectrosc 2005;39:266–9. https://doi.org/10.1016/j.vibspec.2005.03.003.

[38] Wojdyr M. Fityk: A general-purpose peak fitting program. J Appl Crystallogr 2010;43:1126–8. https://doi.org/10.1107/S0021889810030499.

[39] Chang CK, Jiang L, Mao DL, Feng CL. Photoluminescence of $4SrO{\cdot}7Al_2O_3$ ceramics sintered with the aid of B_2O_3. Ceram Int 2004;30:285–90. https://doi.org/10.1016/S0272-8842(03)00101-9.

[40] Bierwagen J, Delgado T, Jiranek G, Yoon S, Gartmann N, Walfort B, et al. Probing traps in the persistent phosphor $SrAl_2O_4:Eu^{2+},Dy^{3+},B^{3+}$ - A wavelength, temperature and sample dependent thermoluminescence investigation. J Lumin 2020;222:117113. https://doi.org/10.1016/j.jlumin.2020.117113.

[41] Clabau F, Rocquefelte X, Jobic S, Deniard P, Whangbo MH, Garcia A, et al. Mechanism of phosphorescence appropriate for the long- lasting phosphors Eu^{2+}-doped $SrAl_2O_4$ with codopants Dy^{3+} and B^{3+}. Chem Mater 2005;17:3904–12. https://doi.org/10.1021/cm050763r.

[42] Thompson N, Murugaraj P, Rix C, Mainwaring DE. Role of oxidative pre-calcination in extending blue emission of $Sr_4Al_{14}O_{25}$ nanophosphors formed with microemulsions. J Alloys Compd 2012;537:147–53. https://doi.org/10.1016/j.jallcom.2012.04.112.

[43] Möncke D, Kamitsos EI, Palles D, Limbach R, Winterstein-Beckmann A, Honma T, et al. Transition and post-transition metal ions in borate glasses: Borate ligand speciation, cluster formation, and their effect on glass transition and mechanical properties. J Chem Phys 2016;145:124501. https://doi.org/10.1063/1.4962323.

[44] Winterstein-Beckmann A, Möncke D, Palles D, Kamitsos EI, Wondraczek L. Structure and properties of orthoborate glasses in the Eu_2O_3-(Sr,Eu)O-B_2O_3 quaternary. J Phys Chem B 2015;119:3259–72. https://doi.org/10.1021/jp5120465.

[45] Bødker MS, Christensen R, Sørensen LG, Østergaard MB, Youngman RE, Mauro JC, et al. Predicting Cation Interactions in Alkali Aluminoborate Glasses using Statistical Mechanics. J Non Cryst Solids 2020;544:120099. https://doi.org/10.1016/j.jnoncrysol.2020.120099.

[46] Ahmed MR, Shareefuddin M. EPR, optical, physical and structural studies of strontium alumino-borate glasses containing Cu^{2+} ions. SN Appl Sci 2019;1:1–10. https://doi.org/10.1007/s42452-019-0201-5.

[47] Inan Akmehmet G, Šturm S, Komelj M, Samardžija Z, Ambrožič B, Sezen M, et al. Origin of long afterglow in strontium aluminate phosphors: Atomic scale imaging of rare earth dopant clustering. Ceram Int 2019:1–5. https://doi.org/10.1016/j.ceramint.2019.06.271.

[48] Inan Akmehmet G. INVESTIGATING THE ORIGINS OF LONG PERSISTENCE IN STRONTIUM ALUMINATE PHOSPHORS BY NANOSCALE RESOLVED IMAGING AND SPECTROSCOPY. PhD thesis, Sabancı University, 2015.

[49] Keiner R, Frosch T, Hanf S, Rusznyak A, Akob DM, Küsel K, et al. Raman spectroscopy - An innovative and versatile tool to follow the respirational activity and carbonate biomineralization of important cave bacteria. Anal Chem 2013;85:8708–14. https://doi.org/10.1021/ac401699d.

[50] Kamitsos EI, Chryssikos GD. Borate glass structure by Raman and infrared spectroscopies. J Mol Struct 1991;247:1–16. https://doi.org/10.1016/0022-2860(91)87058-P.

[51] Zhang S, Pang R, Li D, Fu J, Jia Y, Li H, et al. Reduction of Eu^{3+} due to a change of the topological structure of the BO_3 unit in borate glass. Dalt Trans 2015;44:17916–9. https://doi.org/10.1039/c5dt03606b.

[52] Bril TW. Raman Spectroscopy of Crystalline and Vitreous Borates. PhD thesis,Technische Hogeschool Eindhoven, 1976. https://doi.org/10.6100/IR127808.

[53] Simon G, Hehlen B, Vacher R, Courtens E. Hyper-Raman scattering analysis of the vibrations in vitreous boron oxide. Phys Rev B - Condens Matter Mater Phys 2007;76:1–12. https://doi.org/10.1103/PhysRevB.76.054210.

[54] Varsamis CP, Kamitsos EI, Chryssikos GD. Structure of fast-ion-conducting AgI-doped borate glasses in bulk and thin film forms. Phys Rev B - Condens Matter Mater Phys 1999;60:3885–98. https://doi.org/10.1103/PhysRevB.60.3885.

[55] Varsamis CPE, Makris N, Valvi C, Kamitsos EI. Short-range structure, the role of bismuth and property-structure correlations in bismuth borate glasses. Phys Chem Chem Phys 2021;23:10006–20. https://doi.org/10.1039/d1cp00301a.

[56] Voronko YK, Sobol AA, Shukshin VE. Structure of boron-oxygen groups in crystalline, molten, and glassy alkali-metal and alkaline-earth metaborates. Inorg Mater 2012;48:732–7. https://doi.org/10.1134/S0020168512060210.

[57] Qiu J, Hirao K. Long lasting phosphorescence in Eu^{2+} -doped calcium aluminoborate glasses. Solid State Commun 1998;106:795–8. https://doi.org/10.1016/S0038-1098(98)00134-3.

[58] El Hayek R, Ferey F, Florian P, Pisch A, Neuville DR. Structure and properties of lime alumino-borate glasses. Chem Geol 2017;461:75–81. https://doi.org/10.1016/j.chemgeo.2016.11.025.

[59] Coşgun Ergene A, Khabbaz Abkenar S, Deniz E, Ow-Yang CW. Borate polyanions tuning persistent luminescence in Eu and Dy co-doped strontium aluminate. Mater Adv 2022;3:3238–50. https://doi.org/10.1039/D1MA01234G.

[60] Furuya S, Nakano H, Yokoyama N, Banno H, Fukuda K. Enhancement of photoluminescence intensity and structural change by doping of P^{5+} ion for $Ca_{2-x/2}(Si_{1-x}P_x)O_4:Eu^{2+}$ green phosphor. J Alloys Compd 2016;658:147–51. https://doi.org/10.1016/j.jallcom.2015.10.172.

[61] Castaing V, Monteiro C, Sontakke AD, Asami K, Xu J, Fernández-Carrión AJ, et al. Hexagonal $Sr_{1-x/2}Al_{2-x}Si_xO_4:Eu^{2+},Dy^{3+}$ transparent ceramics with tuneable persistent luminescence properties. Dalt Trans 2020;49:16849–59. https://doi.org/10.1039/D0DT03137B.

[62] Massera J, Głuchowski P, Lastusaari M, Rodrigues LCV, Petit L, Hölsä J, et al. New alternative route for the preparation of phosphate glasses with persistent luminescence properties. J Eur Ceram Soc 2015;35:1255–61. https://doi.org/10.1016/j.jeurceramsoc.2014.11.007.

[63] Moulton BJA, Picinin A, Silva LD, Doerenkamp C, Lozano H, Sampaio D, et al. A critical evaluation of barium silicate glass network polymerization. J Non Cryst

Solids 2022;583:121477. https://doi.org/10.1016/j.jnoncrysol.2022.121477.

[64] Richard K B. Review: the structure of simple phosphate glasses. J Non Cryst Solids 2000;263–264:1–28.

[65] Boccaccini AR, Brauer DS, Hupa L. Bioactive Glasses Fundamentals, Technology and Applications. 2017.

[66] Zhang LY, Li H, Hu LL. Statistical approach to modeling relationships of composition – structure – property I: Alkaline earth phosphate glasses. J Alloys Compd 2018;734:163–71. https://doi.org/10.1016/j.jallcom.2017.11.007.

[67] Muñoz F, Rocherullé J, Ahmed I, Hu L. Phosphate Glasses. 2019. https://doi.org/10.1007/978-3-319-93728-1_16.

[68] Hoppe U. A structural model for phosphate glasses. J Non Cryst Solids 1996;195:138–47. https://doi.org/10.1016/0022-3093(95)00524-2.

[69] K.Brow R. Nature of Alumina in Phosphate Glass:I, Properties of Sodium Aluminophosphate Glass 1992:913–8.

[70] Sarkar D, Mohapatra D, Ray S, Bhattacharyya S, Adak S, Mitra N. Synthesis and characterization of sol-gel derived ZrO_2 doped Al_2O_3 nanopowder. Ceram Int 2007;33:1275–82. https://doi.org/10.1016/j.ceramint.2006.05.002.

[71] Lu X, Deng L, Kerisit S, Du J. Structural role of ZrO_2 and its impact on properties of boroaluminosilicate nuclear waste glasses. Npj Mater Degrad 2018;2. https://doi.org/10.1038/s41529-018-0041-6.

[72] Manara D, Grandjean A, Pinet O, Dussossoy JL, Neuville DR. Sulfur behavior in silicate glasses and melts: Implications for sulfate incorporation in nuclear waste glasses as a function of alkali cation and V_2O_5 content. J Non Cryst Solids 2007;353:12–23. https://doi.org/10.1016/j.jnoncrysol.2006.09.041.

[73] Dimitriev Y, Dimitrov V, Arnaudov M, Topalov D. IR-Spectral Study Of Vanadate Vitreous Systems. J Non Cryst Solids 1982;57:147–56.

[74] Neuville DR, Cormier L, Massiot D. Al coordination and speciation in calcium aluminosilicate glasses: Effects of composition determined by ^{27}Al MQ-MAS NMR and Raman spectroscopy. Chem Geol 2006;229:173–85. https://doi.org/10.1016/j.chemgeo.2006.01.019.

[75] Charpentier T, Okhotnikov K, Novikov AN, Hennet L, Fischer HE, Neuville DR, et al. Structure of Strontium Aluminosilicate Glasses from Molecular Dynamics Simulation, Neutron Diffraction, and Nuclear Magnetic Resonance Studies. J Phys Chem B 2018;122:9567–83. https://doi.org/10.1021/acs.jpcb.8b05721.

[76] Licheron M, Montouillout V, Millot F, Neuville DR. Raman and ^{27}Al NMR structure investigations of aluminate glasses: $(1-x)Al_2O_3-x$ MO, with M=Ca, Sr, Ba and $0.5<x<0.75$). J Non Cryst Solids 2011;357:2796–801. https://doi.org/https://doi.org/10.1016/j.jnoncrysol.2011.03.001.

[77] Poelman D, Avci N, Smet PF. Measured luminance and visual appearance of multi-color persistent phosphors. Opt Express 2009;17:358–64. https://doi.org/10.1364/OE.17.000358.

[78] Karthik A, Manivasakan P, Arunmetha S, Yuvakkumar R, Rajendran V. Production of Al_2O_3-stabilized tetragonal ZrO_2 nanoparticles for thermal barrier coating. Int J Appl Ceram Technol 2013;10:887–99. https://doi.org/10.1111/ijac.12032.

[79] Merzbacher CI, White WB. The structure of alkaline earth aluminosilicate glasses as determined by vibrational spectroscopy. J Non Cryst Solids 1991;130:18–34. https://doi.org/10.1016/0022-3093(91)90152-V.

[80] Kalampounias AG. IR and Raman spectroscopic studies of sol-gel derived alkaline-earth silicate glasses. Bull Mater Sci 2011;34:299–303.

https://doi.org/10.1007/s12034-011-0064-x.

[81] Hudgens JJ, Martin SW. Glass Transition and Infrared Spectra of Low-Alkali, Anhydrous Lithium Phosphate Glasses. J Am Ceram Soc 1993;76:1691–6. https://doi.org/10.1111/j.1151-2916.1993.tb06636.x.

[82] Sun Y, Zhang Z, Liu L, Wang X. FTIR, Raman and NMR investigation of CaO-SiO_2-P_2O_5 and CaO-SiO_2-TiO_2-P_2O_5 glasses. J Non Cryst Solids 2015;420:26–33. https://doi.org/10.1016/j.jnoncrysol.2015.04.017.

[83] Moustafa YM, El-Egili K. Infrared spectra of sodium phosphate glasses. J Non Cryst Solids 1998;240:144–53. https://doi.org/10.1016/S0022-3093(98)00711-X.

[84] Hayakawa S, Yoko T, Sakka S. Structural studies on alkaline earth vanadate glasses (part 1) - IR spectroscopic study -. J Ceram Soc Japan Int Ed 1994;102:522–8.

[85] Shvets P, Dikaya O, Maksimova K, Goikhman A. A review of Raman spectroscopy of vanadium oxides. J Raman Spectrosc 2019;50:1226–44. https://doi.org/10.1002/jrs.5616.

[86] Hehlen B, Neuville DR. Non network-former cations in oxide glasses spotted by Raman scattering. Phys Chem Chem Phys 2020;22:12724–31. https://doi.org/10.1039/d0cp00630k.

[87] Grund Bäck L, Ali S, Karlsson S, Möncke D, Kamitsos EI, Jonson B. Mixed alkali/alkaline earth-silicate glasses: Physical properties and structure by vibrational spectroscopy. Int J Appl Glas Sci 2019;10:349–62. https://doi.org/10.1111/ijag.13101.

[88] Hehlen B, Neuville DR. Raman response of network modifier cations in alumino-silicate glasses. J Phys Chem B 2015;119:4093–8. https://doi.org/10.1021/jp5116299.

[89] Griebenow K, Hoppe U, Möncke D, Kamitsos EI, Wondraczek L. Transition-metal incorporation and Co-Sr/Mn-Sr mixed-modifier effect in metaphosphate glasses. J Non Cryst Solids 2017;460:136–45. https://doi.org/10.1016/j.jnoncrysol.2017.01.022.

[90] Aguiar H, Serra J, González P, León B. Structural study of sol-gel silicate glasses by IR and Raman spectroscopies. J Non Cryst Solids 2009;355:475–80. https://doi.org/10.1016/j.jnoncrysol.2009.01.010.

[91] Abou Neel EA, Chrzanowski W, Pickup DM, O'Dell LA, Mordan NJ, Newport RJ, et al. Structure and properties of strontium-doped phosphate-based glasses. J R Soc Interface 2009;6:435–46. https://doi.org/10.1098/rsif.2008.0348.

[92] Kuwik M, Pisarska J, Pisarski WA. Influence of oxide glass modifiers on the structural and spectroscopic properties of phosphate glasses for visible and near-infrared photonic applications. Materials (Basel) 2020;13:1–20. https://doi.org/10.3390/ma13214746.

[93] Jha K, Jayasimhadri M. Structural and emission properties of Eu^{3+}-doped alkaline earth zinc-phosphate glasses for white LED applications. J Am Ceram Soc 2017;100:1402–11. https://doi.org/10.1111/jace.14668.

[94] Velli LL, Varsamis CPE, Kamitsos EI, Möncke D, Ehrt D. Structural investigation of metaphosphate glasses. Phys Chem Glas 2005;46:178–81.

[95] Liu C, Zhang R, Zhao X, Jia J, Min Y. Quantification of phosphorus structures in $CaO–SiO_2–P_2O_5$ glasses via Raman spectroscopy. J Non Cryst Solids 2021;557. https://doi.org/10.1016/j.jnoncrysol.2020.120579.

[96] Konidakis I, Varsamis CPE, Kamitsos EI, Möncke D, Ehrt D. Structure and properties of mixed strontium-manganese metaphosphate glasses. J Phys Chem C 2010;114:9125–38. https://doi.org/10.1021/jp101750t.

[97] Dutczak D, Jüstel T, Ronda C, Meijerink A. Eu^{2+} luminescence in strontium aluminates. Phys Chem Chem Phys 2015;17:15236–49. https://doi.org/10.1039/c5cp01095k.

[98] Luitel HN, Watari T, Chand R, Torikai T, Yada M. Giant Improvement on the Afterglow of $Sr_4Al_{14}O_{25}:Eu^{2+},Dy^{3+}$ Phosphor by Systematic Investigation on Various Parameters. J Mater 2013;2013:613090. https://doi.org/10.1155/2013/613090.

[99] Botterman J, Joos JJ, Smet PF. Trapping and detrapping in $SrAl_2O_4$:Eu,Dy persistent phosphors: Influence of excitation wavelength and temperature. Phys Rev B - Condens Matter Mater Phys 2014;90:1–15. https://doi.org/10.1103/PhysRevB.90.085147.

[100] Bierwagen J, Yoon S, Gartmann N, Walfort B, Hagemann H. Thermal and concentration dependent energy transfer of Eu^{2+} in $SrAl_2O_4$. Opt Mater Express 2016;6:793–803. https://doi.org/10.1364/OME.6.000793.

[101] Wang Z, Liu Y, Huang Z, Fang M, Wu X. Direct-white-emitting phosphor $SrAl_2O_4$: $Eu^{2+/3+}$ with colour-tunable photoluminescence by variation of europium activator valence. Mater Res Express 2018;5:96202. https://doi.org/10.1088/2053-1591/aad726.

[102] Peng M, Pei Z, Hong G, Su Q. Study on the reduction of $Eu^{3+} \rightarrow Eu^{2+}$ in $Sr_4Al_{14}O_{25}$: Eu prepared in air atmosphere. Chem Phys Lett 2003;371:1–6. https://doi.org/10.1016/S0009-2614(03)00044-7.

[103] Ganesh Kumar K, Balaji Bhargav P, Aravinth K, Arumugam R, Ramasamy P. Dysprosium activated strontium aluminate phosphor: A potential candidate for WLED applications. J Lumin 2020;223:117126. https://doi.org/10.1016/j.jlumin.2020.117126.

[104] Yerpude AN, Dhoble SJ, Ramesh B, Raju BDP. Photoluminescence and decay

properties of Sm^{3+} and Dy^{3+} in $SrAl_4O_7$ phosphor. Adv Mater Lett 2015;6:1111–5. https://doi.org/10.5185/amlett.2015.5919.

[105] Stuart BH. Infrared Spectroscopy: Fundamentals and Applications. 2005. https://doi.org/10.1002/0470011149.

[106] Popovic Z V. Raman scattering in materials science. vol. 214. 1996. https://doi.org/10.4028/www.scientific.net/msf.214.11.

[107] Smith JP, Holahan EC, Smith FC, Marrero V, Booksh KS. A novel multivariate curve resolution-alternating least squares (MCR-ALS) methodology for application in hyperspectral Raman imaging analysis. Analyst 2019;144:5425–38. https://doi.org/10.1039/C9AN00787C.

[108] Lee E. Imaging Modes BT - Raman Imaging: Techniques and Applications. In: Zoubir A, editor., Berlin, Heidelberg: Springer Berlin Heidelberg; 2012, p. 1–37. https://doi.org/10.1007/978-3-642-28252-2_1.

[109] De Juan A, Jaumot J, Tauler R. Multivariate Curve Resolution (MCR). Solving the mixture analysis problem. Anal Methods 2014;6:4964–76. https://doi.org/10.1039/c4ay00571f.

[110] Zhang L, Henson MJ, Sekulic SS. Multivariate data analysis for Raman imaging of a model pharmaceutical tablet. Anal Chim Acta 2005;545:262–78. https://doi.org/https://doi.org/10.1016/j.aca.2005.04.080.

[111] Offroy M, Moreau M, Sobanska S, Milanfar P, Duponchel L. Pushing back the limits of Raman imaging by coupling super-resolution and chemometrics for aerosols characterization. Sci Rep 2015;5:12303. https://doi.org/10.1038/srep12303.

[112] Gautam R, Vanga S, Ariese F, Umapathy S. Review of multidimensional data processing approaches for Raman and infrared spectroscopy. EPJ Tech Instrum

2015;2. https://doi.org/10.1140/epjti/s40485-015-0018-6.

[113] Savitzky A, Golay MJE. Smoothing and Differentiation of Data by Simplified Least Squares Procedures. Anal Chem 1964;36:1627–39. https://doi.org/10.1021/ac60214a047.

[114] Eilers PHC. A Perfect Smoother. Anal Chem 2003;75:3631–6. https://doi.org/10.1021/ac034173t.

[115] Tauler R, Walczak B. Comprehensive Chemometrics Chemical and Biochemical Data Analysis. Elsevier; 2009.